

STRUCTURE AND PROPERTIES OF SODIUM BISMUTH TITANATE
FERROELECTRIC CERAMICS

By

ELENA AKSEL

A DISSERTATION PRESENTED TO THE GRADUATE SCHOOL
OF THE UNIVERSITY OF FLORIDA IN PARTIAL FULFILLMENT
OF THE REQUIREMENTS FOR THE DEGREE OF
DOCTOR OF PHILOSOPHY

UNIVERSITY OF FLORIDA

2012

© 2012 Elena Aksel

To my wonderful family

ACKNOWLEDGMENTS

I am truly thankful for the wonderful experience I have had at the University of Florida over the past four years. I would like to first and foremost thank my advisor, Professor Jacob Jones. His guidance and encouragement throughout my time here have helped and motivated me along this process. His passion and excitement for our work are truly contagious. I am also thankful to my PhD committee – Professors Simon Phillpot, Juan Nino, Wolfgang Sigmund, and Alexander Angerhofer for their many helpful discussions during my time here. I also appreciate the willingness of Dr. Jennifer Andrew to substitute in my committee. I am thankful to my group members, both past and present, for their constant input and feedback on all of my work. I especially would like to thank Humberto Foronda, Jared Carter, and Kevin Seymour for their help with the processing of my samples and Dr. Jennifer Forrester and Dr. Goknur Tutuncu for the hours they have volunteered to the reading of this dissertation. I am also incredibly grateful to the University of Florida Alumni Fellowship and the National Science Foundation (award number DMR-0746902) for my funding.

During my PhD career I have been fortunate to work with our very inspiring collaborators around the world. I would like to thank Professor Jürgen Rödel, Dr. Torsten Granzow, Dr. Wook Jo, Dr. Silke Schaab, and the rest of the NAW group at the Technical University of Darmstadt for hosting me during my three month stay there and teaching me so much about some the fundamentals of our research. I also would like to thank Robert Dittmer for conducting some follow up measurements at Darmstadt after my visit. I am thankful to Dr. Rüdiger Eichel, Dr. Emre Erdem, and Dr. Peter Jakes for sharing their knowledge of Electron Paramagnetic Resonance and hosting me during my stay in Freiburg. I am especially grateful to the Sonderforschungsbereich (SFB) 595

from the Deutsche Forschungsgemeinschaft for funding my six month stay in Germany. I have also had the wonderful opportunity to spend a month working with Professor Dragan Damjanovic at the Ceramics Laboratory of the École Polytechnique Fédérale de Lausanne. Working with Dragan is always incredible inspiring and enlightening. This trip was graciously sponsored by the National Science Foundation International Research Experience for Students (NSF IRES) under award number OISE-0755170. My doctorate research has also involved numerous trips to several national laboratories, both in the US and abroad, and I am especially grateful for the help I have received from the scientists there – Dr. Matthew Suchomel (APS), Dr. Katharine Page (LANSCE), Dr. Thomas Proffen (LANSCE), Dr. Andrew Studer (ANSTO), and Dr. John Daniels (ESRF).

Part of the work presented in this dissertation was done with our collaborators, and I would like to specifically acknowledge their contributions. The structural refinement of NBT presented in Chapter 3 was done based on the starting models provided by Professor Pam Thomas from the University of Warwick. The pair distribution function (PDF) analysis presented in Chapter 5 was done in collaboration with Dr. Katharine Page from Los Alamos National Laboratory. I would like to thank Dr. Daniel Shoemaker from Argonne National Laboratory for providing the Reverse Monte Carlo simulations of the PDF data. Finally, I am grateful to Dr. Marco Deluca from the Montanuniversitaet in Leoben, Austria for providing the Raman spectroscopy measurements and analysis presented in Chapter 8.

Finally, above all, I am incredibly thankful for my amazing family and friends. I cannot express enough all that my parents have done for me to have the opportunity to

be here. My sister, Alla, has also played an absolutely integral part in my desire and motivation to pursue a graduate education. I would like to all of the wonderful friends I have made in Gainesville along the way for helping me make the most of these years.

TABLE OF CONTENTS

	<u>page</u>
ACKNOWLEDGMENTS.....	4
LIST OF TABLES.....	10
LIST OF FIGURES.....	12
LIST OF ABBREVIATIONS.....	16
ABSTRACT.....	18
CHAPTER	
1 INTRODUCTION.....	21
Motivation.....	21
Fundamentals of Piezoelectricity.....	22
NBT Background.....	26
Objective of Research.....	29
Dissertation Outline.....	29
2 PHASE FORMATION OF NBT DURING SOLID STATE PROCESSING.....	33
Background.....	33
Experimental.....	34
Results and Discussion.....	35
Calcination Profile.....	35
Transient Phases.....	35
Mechanism.....	37
Summary.....	41
3 LONG RANGE AVERAGE ROOM TEMPERATURE STRUCTURE OF NBT USING HIGH-RESOLUTION X-RAY DIFFRACTION.....	49
Motivation.....	49
Experimental.....	49
Results and Discussion.....	51
Summary.....	55
4 AVERAGE STRUCTURE OF NBT USING X-RAY AND NEUTRON DIFFRACTION.....	61
Motivation.....	61
Experimental.....	61
Results and Discussion.....	62

	Summary	68
5	LOCAL ATOMIC STRUCTURE DEVIATION FROM AVERAGE STRUCTURE OF NBT.....	82
	Motivation	82
	Experimental.....	83
	Results and Discussion.....	84
	Rietveld Analysis	84
	Small Box PDF Modeling.....	86
	Reverse Monte Carlo Modeling.....	91
	Summary	93
6	PHASE TRANSITION SEQUENCE OF NBT USING HIGH-RESOLUTION X-RAY DIFFRACTION	106
	Motivation	106
	Experimental.....	108
	Results and Discussion.....	108
	Summary	110
7	STRUCTURE AND PROPERTIES OF LA-MODIFIED NBT AT AMBIENT AND ELEVATED TEMPERATURES.....	114
	Motivation	114
	Experimental.....	115
	Results.....	117
	Electrical Property Measurements.....	117
	Crystallographic Structure of La-Modified NBT	118
	Discussion	121
	Summary	123
8	STRUCTURE AND PROPERTIES OF FE-MODIFIED NBT AT AMBIENT AND ELEVATED TEMPERATURES.....	134
	Motivation	134
	Experimental.....	136
	Results.....	137
	Temperature Dependence of Properties	137
	Crystallographic Structure of Unmodified and Fe-Modified NBT	138
	Raman Spectroscopy of Unmodified and Fe-Modified NBT	141
	Discussion	144
	Summary	149
9	CONCLUSIONS AND FUTURE WORK	161
	Conclusions	161
	Future Work.....	164

APPENDIX

A	TECHNIQUES AND MATERIALS	167
	Materials	167
	Structural Refinement	167
	Pair Distribution Function Analysis	168
B	SUPPLEMENTAL INFORMATION TO CHAPTER 3	175
C	SUPPLEMENTAL INFORMATION TO CHAPTER 7	178
D	SUPPLEMENTAL INFORMATION TO CHAPTER 8	180
E	ADDITIONAL PROPERTY MEASUREMENTS	182
F	PUBLICATIONS LIST	193
	LIST OF REFERENCES	195
	BIOGRAPHICAL SKETCH.....	204

LIST OF TABLES

<u>Table</u>	<u>page</u>
1-1	Summary of the piezoelectric and ferroelectric properties of NBT and PZT 30
3-1	Summary of refined lattice parameters and Bragg fitting values from the Cc refinement of sintered NBT. 57
3-2	Summary of refined atomic positions and occupancies resulting from the Cc refinement of the sintered material. 58
4-1	Lattice parameters of NBT at room temperature determined from a structural refinement of diffraction data. 69
4-2	Fitting values of the refinement of NBT at room temperature. 70
4-3	Atomic positions for NBT at room temperature. 71
4-4	Anisotropic displacement parameters for NBT at room temperature, determined from a combined X-ray and neutron Rietveld refinement. 72
4-5	Anisotropic displacement parameters for NBT at room temperature, determined from a Rietveld refinement of the neutron diffraction data. 73
4-6	Summary of the refined lattice parameters and fitting values of NBT at 15 K from a Rietveld refinement of the neutron diffraction data. 74
4-7	Atomic positions and anisotropic displacement parameters for NBT at 15 K, determined from a Rietveld refinement of the neutron diffraction data. 75
5-1	Refined isotropic displacement parameters for calcined and sintered NBT from a structural refinement and PDF fit results. 95
6-1	Refined phase proportions, lattice parameters, cell volume, and criteria of fit parameters for all Rietveld refinements. 111
7-1	Depolarization temperatures, T_d (°C), measured by <i>in situ</i> converse d_{33} , <i>ex situ</i> direct d_{33} and permittivity in all investigated compositions. 124
7-2	Refined phase proportions, lattice parameters, cell volume, and criteria of fit parameters for samples with increasing La content at room temperature. 125
7-3	Refined phase proportions, lattice parameters, cell volume, and criteria of fit parameters for the 1 at% La sample at selected temperatures. 126
8-1	Depolarization temperatures, T_d (°C), measured by Raman spectroscopy, <i>in situ</i> converse d_{33} , <i>ex situ</i> direct d_{33} and synchrotron XRD. 150

8-2	Refined lattice parameters and Bragg fitting values for the samples with increasing Fe-modification.....	151
8-3	Refined lattice parameters and Bragg fitting values for 1 at% Fe-modified NBT with increasing temperature.	152
B-1	Refined lattice parameters and profile fits of calcined and sintered NBT.....	175
B-2	Refined atomic positions in calcined and sintered NBT.....	176
B-3	Refined occupancies in calcined and sintered NBT.....	177
C-1	Refined atomic positions and isotropic displacement parameters (\AA^2) for samples with increasing La content at room temperatures.....	178
C-2	Refined atomic positions and isotropic displacement parameters (\AA^2) for the 1 at% La doped NBT sample at selected temperatures.	179
D-1	Refined atomic positions and isotropic displacement parameters (\AA^2) for the selected Fe modified NBT samples at room temperature.....	180
D-2	Refined atomic positions and isotropic displacement parameters (\AA^2) for the 1 at% Fe sample at selected temperatures.	181

LIST OF FIGURES

<u>Figure</u>		<u>page</u>
1-1	Phase equilibrium diagram for the $\text{Na}_2\text{O}-\text{Bi}_2\text{O}_3-\text{TiO}_2$ system at 1000°C , reproduced from Uchida and Kikuchi. ¹⁹	31
1-2	Comparison of the different phases of NBT.....	32
2-1	X-ray diffraction patterns at selected temperatures during the calcination process.....	42
2-2	Compilation of the XRD patterns recorded during the heating of the reactant powders and solid-state synthesis of NBT.....	43
2-3	Integrated intensity of the $2\theta = 33^\circ$ reflection of NBT reactants, the 33° reflection of NBT, and the 31° reflection of the intermediate phase.....	44
2-4	Two types of behavior observed in the formation of NBT reflections.....	45
2-5	Schematic diagrams of possible phase formation mechanisms.	46
2-6	The relationship between corresponding planes of $\alpha\text{-Bi}_2\text{O}_3$ and NBT at selected 2θ angles.....	47
2-7	Comparison of the atomic arrangement in $\alpha\text{-Bi}_2\text{O}_3$ and NBT.....	48
3-1	Synchrotron XRD pattern of calcined NBT powder and results of crystal structure refinement.....	59
3-2	Synchrotron XRD pattern of sintered NBT powder and results of crystallographic refinement.....	60
4-1	Powder neutron diffraction pattern of sintered NBT powders (x) along with the results of the calculated fit (-).....	76
4-2	Powder diffraction patterns of sintered NBT powders from X-ray (x) and neutron (x) diffraction with the results of the calculated fits (-).....	77
4-3	Thermal ellipsoids of NBT at room temperature obtained from a combined refinement of X-ray and neutron diffraction data.....	78
4-4	Thermal ellipsoids of NBT at room temperature obtained from a refinement of the neutron diffraction data.....	79
4-5	Thermal ellipsoids of NBT at 15 K obtained from a refinement of the neutron diffraction data.....	80
4-6	Schematic of the oxygen octahedral tilting calculation.	81

5-1	Powder diffraction patterns of sintered (x) and calcined (x) NBT using neutron and X-ray diffraction data with the results of the calculated fits (-).	96
5-2	Fourier maps represented as 3D isosurfaces showing the total scattering density in the NBT unit cell for neutron and X-ray Bragg profiles.	97
5-3	Results of fitting 1-20 Å X-ray $G(r)$ s and neutron $G(r)$ s with the Cc average structure model for calcined and sintered NBT samples.	98
5-4	An examination of A-site ordering using PDF models.	99
5-5	Calculated bond lengths from the 'box-car fitting' method for both calcined and sintered NBT.	100
5-6	The calculated bond valence sums for elements in calcined and sintered NBT.	101
5-7	Reverse Monte Carlo fits to the neutron PDF of calcined and sintered NBT. ...	102
5-8	Schematic diagram showing folded RMC models, which produce "point clouds" of atoms at each crystallographic site.	103
5-9	Partial pair distribution functions from the RMC model of a sintered sample....	104
5-10	Pseudo-cubic representation of the NBT unit cell showcasing the arrangement of the three unique oxygen lattice positions relative to Bi.....	105
6-1	The evolution of selected Bragg reflections of NBT from room temperature to 600°C.	112
6-2	Rietveld refinement of the XRD pattern measured at 250°C.	113
7-1	Piezoelectric properties of unmodified and La-modified NBT.	127
7-2	The thermal depolarization properties of NBT, measured <i>in situ</i> and <i>ex situ</i>	128
7-3	Permittivity at selected frequencies was measured with temperature for NBT samples modified with La in compositions ranging from 0-1.5 at%.	129
7-4	Excerpts of high resolution XRD patterns of NBT with varying La modification.	130
7-5	Rietveld refinement of a high resolution XRD pattern of 1% La-modified NBT showing the observed pattern (x) and the calculated fit (—).....	131
7-6	Excerpts of high resolution XRD patterns of 1% La-modified NBT at selected temperatures.	132

7-7	Selected areas of XRD patterns of A) unmodified and B) 1% La modified NBT plotted as a function of temperature.	133
8-1	Longitudinal piezoelectric coefficient d_{33} measured as a function of temperature for various compositions of Fe-modified NBT.....	153
8-2	Permittivity and loss measured as a function of temperature at 0.1, 1, 10, 100, and 1000 kHz for unmodified and 0.5 at% Fe modified NBT.....	154
8-3	Excerpts of high resolution XRD patterns of NBT with varying Fe concentrations.	155
8-4	Rietveld refinement of a high resolution XRD pattern of 1% Fe-modified NBT showing the observed pattern (x) and the calculated fit (—).....	156
8-5	Excerpts of high resolution XRD patterns of 1% Fe-modified NBT at selected temperatures.	157
8-6	Selected areas of XRD patterns of A) unmodified and B) 1% Fe modified NBT as a function of temperature.....	158
8-7	Raman spectra of unmodified and Fe-modified NBT samples.	159
8-8	Variation of A_1 phonon line center ($\sim 270 \text{ cm}^{-1}$) as a function of temperature for all Fe modified compositions.	160
A-1	SEM images of NBT reactant powders.....	170
A-2	SEM images of calcined NBT powders.	171
A-3	SEM images of a cracked surface of sintered NBT pellets.....	172
A-4	Total scattering function, plotted as $Q(S(Q)-1)$, for undoped sintered NBT powder.....	173
A-5	Neutron $G(r)$ of undoped sintered NBT powder.....	174
E-1	Relative permittivity measured as a function of frequency for unmodified and Fe- and La- modified NBT samples.	185
E-2	Tan δ measured as a function of frequency for unmodified and Fe- and La-modified NBT samples.	186
E-3	Displacement measured as a function of small applied voltages for a poled unmodified NBT sample.	187
E-4	Converse d_{33} calculated as a function of applied field unmodified and Fe- and La- modified NBT samples.	188

E-5	Normalized converse d_{33} values as a function of applied field unmodified and Fe- and La- modified NBT samples.	189
E-6	Diffraction patterns of undoped NBT as a function of applied electric field. The results shown were measured parallel to the applied field.	190
E-7	Diffraction patterns of 1 at% La modified NBT as a function of applied electric field. The results shown were measured parallel to the applied field.	191
E-8	Diffraction patterns of 1 at% Fe modified NBT as a function of applied electric field. The results shown were measured parallel to the applied field. ..	192

LIST OF ABBREVIATIONS

PZT	Lead zirconate titanate
NBT	Sodium bismuth titanate
E_c	Coercive field
P_r	Remanent polarization
S_i	Electric field induced strain
E_j	Applied electric field
d_{ij}	Piezoelectric coefficient
D_i	Dielectric displacement
σ_j	Applied stress
d_{33}	Longitudinal piezoelectric coefficient
ϵ_0	Permittivity of free space
ϵ_r	Relative permittivity
k_p	Electromechanical coupling factor
T_d	Depolarization temperature
T_c	Curie temperature
XRD	X-ray diffraction
BTO	$\text{Bi}_4\text{Ti}_3\text{O}_{12}$
SEM	Scanning electron microscope
R_p	R -pattern
R_{wp}	R -weighted pattern
MPB	Morphotropic phase boundary
B_{ij}	Thermal displacement tensor
B	Thermal parameter
U	Atomic vibration parameter

ω	Oxygen octahedral tilting angle
TEM	Transmission electron microscopy
DFT	Density functional theory
PDF	Pair distribution function
S(Q)	Total scattering function
$g(r)$	Atomic pair distribution function
ρ_0	Number density of atoms in the system
G(r)	Reduced pair distribution function
RMC	Reverse Monte Carlo
R_w	Weighted residual from PDFgui fits (equivalent to R_{wp} from GSAS)
BVS	Bond valence sum
$n(r)$	Partial pair distribution function

Abstract of Dissertation Presented to the Graduate School
of the University of Florida in Partial Fulfillment of the
Requirements for the Degree of Doctor of Philosophy

STRUCTURE AND PROPERTIES OF SODIUM BISMUTH TITANATE
FERROELECTRIC CERAMICS

By

Elena Aksel

May 2012

Chair: Jacob L. Jones

Major: Materials Science and Engineering

Piezoelectric materials are commonly used in sensor and actuator technologies due to their unique ability to couple electrical and mechanical displacements. Applications of piezoelectric materials range from diesel engine fuel injectors, sonar, ultrasound, and nanopositioners in scanning microscopes. Changing environmental regulations and policies have led to a recent surge in the research of lead-free piezoelectric materials. One such system currently under investigation is sodium bismuth titanate ($\text{Na}_{0.5}\text{Bi}_{0.5}\text{TiO}_3$) or NBT. It has recently been investigated with the addition of chemical modifiers as well as part of various solid solutions with other compounds. However, research into the structure and properties of NBT is still in its infancy. The aim of this dissertation was to develop a comprehensive understanding of the crystal structure and property relationships in NBT.

First, the formation of the NBT phase during solid state processing was examined using *in situ* X-ray diffraction. It was determined that NBT forms through a particle conversion mechanism of the Bi_2O_3 particle. The average and local room temperature structure of calcined and sintered NBT were examined using both high resolution synchrotron X-ray diffraction and neutron diffraction techniques. It was determined that

the room temperature average structure of this material is best modeled using the monoclinic Cc space group rather than the previously accepted rhombohedral $R3c$ space group. A combined high resolution XRD and neutron diffraction Rietveld refinement provided refined lattice parameters, atomic positions, and displacement parameters. The departure of the local structure of NBT from the average structure was examined through the Pair Distribution Function analysis. It was determined that Na^+ and Bi^{3+} , which share the A-site, have differing bonding environments with their surrounding O^{2-} ions.

In order to understand the origin of the piezoelectric depolarization behavior of NBT, crystal structure refinements were undertaken at elevated temperatures. It was determined that a fraction of the material is present in short range regions and could not be described using the average Cc structure. It was therefore modeled using the prototype cubic phase of the $Pm\bar{3}m$ space group. It was proposed that thermal depoling in NBT occurs due to the loss of long-range ferroelectric order along with a decreasing volume fraction of the major Cc phase and the associated percolation of a nanoscale disordered phase.

Finally, effect of a donor (La_A^\bullet , where A denotes the A-site) and an acceptor (Fe_B' , where B denotes the B-site) chemical modification on the temperature dependent structure and properties was explored. It was shown that La substitution decreased the depolarization temperature with an associated higher fraction of the $Pm\bar{3}m$ phase, while Fe modification led to an increase in the depolarization temperature and a decrease in the fraction of the $Pm\bar{3}m$ phase. The correlation between the changes in

depolarization temperature and the $Pm\bar{3}m$ phase fraction supports the hypothesis that the local scale disordered portion of the material influences the depolarization of NBT.

CHAPTER 1 INTRODUCTION

Motivation

Piezoelectric materials are commonly used in sensor and actuator technologies due to their unique ability to couple electrical and mechanical displacements, *i.e.*, to change electrical polarization in response to an applied mechanical stress or mechanically strain in response to an applied electric field.¹ As such, they have been referred to as “smart” ceramics, because they are susceptible to a change in the environment and respond to it. Compared to other electromechanical transduction technologies, piezoelectric materials offer a high pressure per density ratio for actuator devices, high environmental and chemical stability, and capabilities of operating at high temperatures and frequencies. Applications of piezoelectric materials range from buzzers to diesel engine fuel injectors, sonar, ultrasound, and nanositioners in scanning microscopes. The most commonly used piezoelectric ceramic is lead zirconate titanate ($\text{Pb}[\text{Zr}_x\text{Ti}_{1-x}]\text{O}_3$), also known as PZT. The wide application range of this material is attributed to its high piezoelectric coefficient, stability at high temperatures, as well as the ease of property modification through chemical substitution.²

With changing environmental regulations and policies, there is a strong push to replace lead (Pb) in these materials. This has led to a recent surge in the research of lead-free piezoelectric materials.³⁻⁷ However, the piezoelectric ceramics industry is still overwhelmingly dominated by the use of high lead ceramic components as there currently are no suitable lead-free replacements.^{8,9} Part of the challenge of finding a lead-free substitute for PZT is a lack in the fundamental understanding of the structure-

property relationship in novel materials. One such system that is currently under intense investigation as a possible replacement to PZT is sodium bismuth titanate ($\text{Na}_{0.5}\text{Bi}_{0.5}\text{TiO}_3$) or NBT. It has recently been investigated with the addition of chemical modifiers as well as part of various solid solutions with other compounds.¹⁰⁻¹⁵ However, research into the structure and properties of NBT is still in its infancy.

Fundamentals of Piezoelectricity

This description of the fundamentals of piezoelectricity is reprinted with permission from E. Aksel and J. L. Jones, "Advances in Lead-Free Piezoelectric Materials for Sensors and Actuators," *Sensors*, Vol. 10, No. 3, pp. 1935-1954 (2010).⁶ The only crystallographic requirement for a material to exhibit piezoelectricity is that it must be non-centrosymmetric. Examples of non-centrosymmetric crystal structures that are used in piezoelectric devices include aluminum nitride (AlN) and quartz. In many piezoelectric materials, a spontaneous polarization also exists due to the separation of negative and positive charge centers in the crystallographic unit cell. A characteristic example of a structure which exhibits a spontaneous polarization at certain temperatures is the perovskite structure, ABO_3 . In this structure, the body-centered atom (B) and the oxygen octahedron (O_3) displace non-uniformly relative to the corner atom (A), resulting in a non-centrosymmetric structure. As the perovskite structure is cooled from a high temperature cubic phase (centrosymmetric), it can undergo several different phase transitions and eventually transform to tetragonal, rhombohedral, orthorhombic, or monoclinic structures at different temperatures. The temperature at which the structure transforms from the high-temperature cubic phase to the first structure exhibiting a spontaneous polarization typically coincides with the Curie temperature. When cooling a material through the Curie temperature, different regions of the material take on

different crystallographic orientations of the lower symmetry crystal structure. These regions are referred to as domains and they are separated from each other by domain walls.

Ferroelectricity is the ability of a material to change its direction of spontaneous polarization in response to the application of an electric field. The electric field required for this reorientation to occur is known as the coercive field and typically involves the motion of a ferroelectric domain wall. There is often a distribution of local coercive fields in a polycrystalline material since there may be compositional variations across a grain or different stress states of different grains. The macroscopically observed coercive field (E_c) is the electric field required to obtain zero macroscopic polarization due to compensating positive and negative local polarization states.

Upon cooling from the high processing temperatures required for ceramic materials, polycrystalline ceramics exhibit neither a net macroscopic spontaneous polarization nor piezoelectricity at the macroscopic length scale. This is because the structure is composed of an equal number of all possible domain orientations, each with a spontaneous polarization oriented in a different direction. Since the material contains many domains, all oriented in different directions, the local areas of spontaneous polarization cancel each other and the material does not exhibit a net macroscopic polarization. For a polycrystalline material to exhibit piezoelectricity at the macroscopic length scale it must go through a poling process wherein an electric field is applied and the domains are aligned more closely parallel to the electric field direction. After poling, the material will have a net macroscopic polarization parallel to the direction of the poling field and will exhibit piezoelectricity at the macroscopic length scale.

The converse piezoelectric effect describes the strain generated in a piezoelectric material in response to an applied electric field. This effect is written as:

$$S_i = d_{ij}E_j \quad (1-1)$$

where S_i is the electric field induced strain, E_j is the applied electric field and d_{ij} is the piezoelectric coefficient. The piezoelectric coefficient is actually a third rank tensor, even though it is written in Equation (1-1) in reduced matrix notation by representing the mechanical strain as a 1-dimensional matrix with elements $i = 1, 2 \dots 6$. The converse piezoelectric effect is exploited in actuator devices.

For sensing applications, the direct piezoelectric effect describes a change in polarization due to an applied stress and is written as:

$$D_i = d_{ij}\sigma_j \quad (1-2)$$

where D_i is the dielectric displacement and σ_j is the applied stress.

In Equation (1-1) and (1-2), the coordinate axes are defined by the polarization of the sample and are assigned to the 3-direction. When an electric field is applied parallel to the 3-direction and strain is also measured in the 3-direction, the piezoelectric coefficient of relevance is the longitudinal piezoelectric coefficient, d_{33} :

$$S_3 = d_{33}E_3 \quad (1-3)$$

The piezoelectric coefficients described by the direct and converse piezoelectric effects are mathematically equivalent. Therefore, the longitudinal piezoelectric coefficient described by the converse piezoelectric effect (Equation (1-3)) is equivalent to the longitudinal piezoelectric coefficient described by the direct piezoelectric effect:

$$D_3 = d_{33}\sigma_3 \quad (1-4)$$

Another important property of a piezoelectric material is permittivity, which is related to how much electrical potential energy can be stored in a given volume of the material under the influence of an electric field. This is often maximized near phase transitions and its distribution with temperature is broad in relaxor ferroelectric materials. Often, the permittivity is reported relative to the permittivity of free space ($\epsilon_{33}^T/\epsilon_0$), also called the relative permittivity (ϵ_r) or often the dielectric constant. Finally, the electromechanical coupling factor (k_p) relates the electrical energy output to the total mechanical energy input or vice versa.¹⁶

The properties of a piezoelectric material can be improved with small addition of substitutional impurities, or dopants, as previously exploited in designing the properties of PZT. Depending on the type of dopant and its position in the unit cell, the structure and properties of a material will change in different ways. In the case of PZT, donor doping involves dopant ions which are more positive in valence than the ions they are replacing and this leads to a “soft” ferroelectric material behavior.¹⁷ Some of the property changes associated with this type of doping include a decrease in the coercive field, increased dielectric constant, and an increased electromechanical coupling factor.¹⁷ On the other hand, acceptor doping in PZT involves a dopant ion which is less positive in valence than the host ion and this leads to a “hard” ferroelectric material behavior.¹⁷ Several characteristic changes are attributed to this type of doping and include a moderately lowered electrical resistivity, higher coercive field, and a relatively lower dielectric constant.¹⁷ “Hard” PZT materials are also often more difficult to pole and depole.

NBT Background

Although NBT was first reported in the 1960s by Smolenskii *et al.*,¹⁸ it did not receive much attention until the recent surge in lead-free materials development in the past two decades.³ In 1978 Uchida and Kikuchi examined the phase equilibria of the $\text{Na}_2\text{O-Bi}_2\text{O}_3\text{-TiO}_2$ system which contains NBT.¹⁹ This phase diagram is reproduced in Figure 1-1. Early structural studies describe NBT as having a rhombohedral lattice.²⁰⁻²² Vakhrushev reported superstructure reflections indicating tilting of a single axis (corresponding to what is now known as the $P4bm$ phase²³) above $\sim 300^\circ\text{C}$ and tilting of all three axes (corresponding to what is now often referred to as the room temperature $R3c$ structure) at lower temperatures.²¹ Between approximately 250°C and 300°C , the existence of both tilting systems suggested a mixed phase region.²¹ In 1995, Suchanicz and Kwapulinski observed a rhombohedral phase up to 250°C , mixed rhombohedral and tetragonal to $\sim 400^\circ\text{C}$, and tetragonal to $\sim 525^\circ\text{C}$.²² In 2002, Jones and Thomas confirmed a single phase rhombohedral $R3c$ structure with the $a^-a^-a^-$ tilt system up to 255°C , a region of phase coexistence ranging from at least $307 - 327^\circ\text{C}$, a tetragonal $P4bm$ structure with the $a^0a^0c^+$ tilting system to $\sim 500^\circ\text{C}$, and a cubic $Pm\bar{3}m$ structure above 540°C .²⁴ A diagram comparing the pseudo-cubic NBT unit cell in the $Pm\bar{3}m$, $P4bm$, and $R3c$ space groups is given in Figure 1-2.

Using transmission electron microscopy, it was found that at room temperature, nano-scale tetragonal ($P4bm$) platelets exist within a rhombohedral ($R3c$) matrix, and the $P4bm$ superlattice reflections increase in intensity with heating until the material transitions to a tetragonal phase.^{25, 26} By utilizing visibility criteria to determine the symmetry of these platelet-like inclusions at room temperature, it was established that

they are regions with octahedral tilting $a^0a^0c^+$.²⁷ At 200°C, an intergrowth of orthorhombic (*Pnma*) platelet-shaped domains inside a *R3c* matrix was observed, and increased in volume fraction up to 300°C.²⁶

Recent single crystal experiments by Gorfman and Thomas suggested that the average structure of NBT single crystals is inconsistent with the rhombohedral system but is better described by the monoclinic space group *Cc*.²⁸ The relationship between the *Cc* unit cell and the pseudo-cubic unit cell is shown in Figure 1-2D. In addition, first-principles calculations based on density functional theory (DFT) were utilized to examine potential A-site with the conclusion that short range chemical ordering is expected.²⁹ Recently, Jeong *et al.* compared the short range structure of NBT to that of its solid solution with $\text{Bi}_{0.5}\text{K}_{0.5}\text{TiO}_3$ through neutron total scattering studies with Reverse Monte Carlo modeling.³⁰ They report that, on a 0-4 Å length scale, the bonding environment of Bi with O is different from that of Na with O, due to a large displacement of Bi from its average position.³⁰

NBT has a high Curie temperature, T_c , of 325°C and a piezoelectric constant (d_{33}) of 73 pC/N,³¹ making it a promising substitute for PZT. Table 1-1 compares several properties of NBT with commercial PZT. Although this material shows potential as a lead-free substitute for PZT, it also has some drawbacks, e.g. the low piezoelectric constant, high coercive field, low depolarization temperature, and high conductivity.³¹ Properties, such as depolarization temperature, T_d , of ferroelectric materials are often modified with the use of chemical substitution, known as doping.¹⁶

One common type of aliovalent modification in PZT is with the use of donor dopants, which lead to a “softening” of the material.³² This type of doping often leads to

higher permittivity and piezoelectric coupling but little change in the Curie temperature.³² A commonly used donor dopant in the ferroelectric ceramic PZT is La^{3+} , which substitutes for the Pb^{2+} on the A-site.³² Recent literature studies have examined the effects of La modification in NBT. Watanabe *et al.* reported that with the addition of 1at% La to NBT, the d_{33} increased from 70 to 82 pC/N, and free permittivity increased from about 350 to 450.³³ Additionally, it decreased the T_d from 180 to 150°C.³³ Herabut and Safari found that the addition of 1.72 at% La increased the d_{33} from 58 to 91 pC/N and the relative permittivity from 240 to 550.¹¹ They also found that La substitution caused the structure of NBT to approach cubic.¹¹ These changes in NBT properties with La modification, while not as pronounced as in PZT, show that La affects both the properties and structure of this material.

Another type of aliovalent modification in PZT is with the use of acceptor dopants, such as the substitution of Fe^{3+} ions for the Zr^{4+} and Ti^{4+} B-site ions.³² Extensive studies have shown that chemical modification of Ti-based perovskite ferroelectrics with Fe generally leads to so-called material “hardening” characterized by a decrease in the permittivity and piezoelectric coupling factor accompanied by an increase in the mechanical and electrical quality factor.^{32, 34} Effects of Fe modification on NBT include a slight decrease in the T_c , resistivity, and planar coupling factor as well as an increase in the coercive field,³⁵ consistent with Fe modified PZT. Davies *et al.* showed an increase in the T_d with substitution of Fe or Mn on the perovskite B-site.³⁶ These modifiers also increased the piezoelectric coefficient at higher temperatures prior to piezoelectric depolarization.³⁶

Objective of Research

The aim of this work is to develop a comprehensive understanding of the structure and property relationships in NBT. The intent is that this will aid in the development of novel lead-free materials. The following are the main objectives:

1. To develop an understanding of the local and average crystallographic structure of NBT.
2. To correlate changes in the piezoelectric properties to structural changes with temperature.
3. To examine the impact of chemical modification on the structure and properties of NBT.

Dissertation Outline

The formation of the NBT phase during solid state processing is examined in Chapter 2. The average and local room temperature structure of NBT, as determined from X-ray and neutron studies, is described in Chapters 3 – 5. Chapter 3 describes the room temperature structure of NBT from high resolution X-ray diffraction measurements, Chapter 4 expands on those results using a combined approach with the addition of neutron diffraction data, and Chapter 5 investigates the local structure of NBT using the Pair Distribution Function. The evolution of the structure as a function of temperature is then discussed in Chapter 6. Finally, the effect of a donor (La_A^* , where A denotes the A-site) and an acceptor (Fe_B' , where B denotes the B-site) chemical modifier on the temperature dependent structure and properties is presented in Chapters 7 and 8, respectively.

Table 1-1. Summary of the piezoelectric and ferroelectric properties of NBT and PZT

Property	NBT	Commercial PIC 151 $\text{Pb}_{0.99}\text{[Zr}_{0.45}\text{Ti}_{0.47}(\text{Ni}_{0.33}\text{Sb}_{0.67})_{0.08}]\text{O}_3$	Commercial Navy II PZT (K350 Piezo Technologies)
Piezoelectric constant (pC/N)	73 [31]	503 [37]	390 [38]
Remnant polarization ($\mu\text{C}/\text{cm}^2$)	38 [39]	35 [37]	40
Coercive field (kV/mm)	7.3 [40]	1 [41]	2
Curie temperature ($^{\circ}\text{C}$)	325 [31]	260 [41]	360 [38]
Depolarization temperature ($^{\circ}\text{C}$)	187 [31]	254 [41]	-

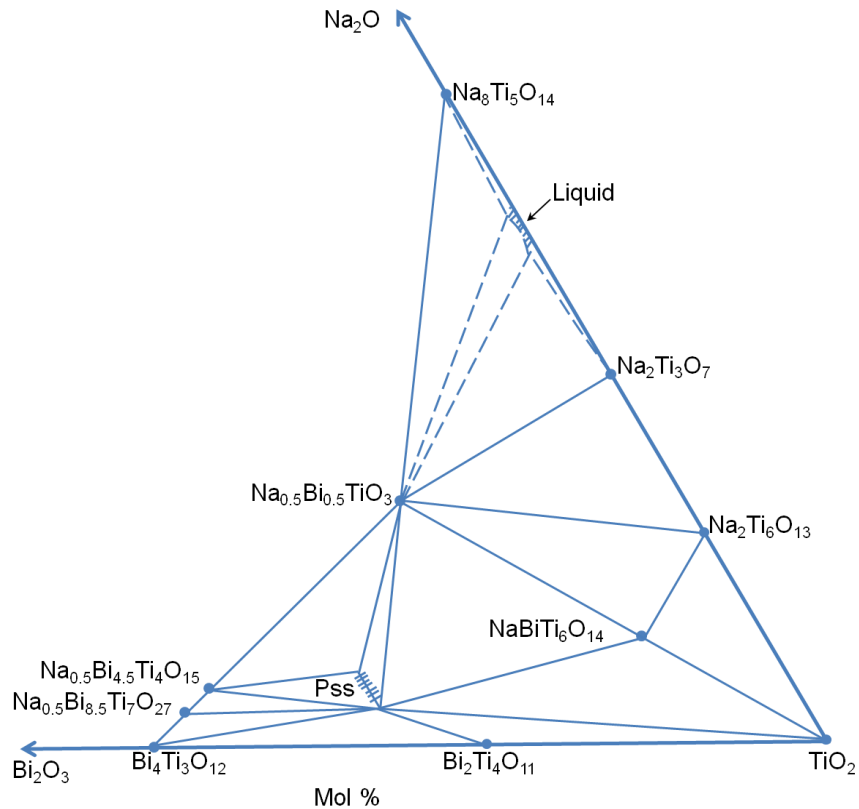


Figure 1-1. Phase equilibrium diagram for the Na₂O-Bi₂O₃-TiO₂ system at 1000°C, reproduced from Uchida and Kikuchi.¹⁹ Pss represents the solid solution of cubic pyrochlore.

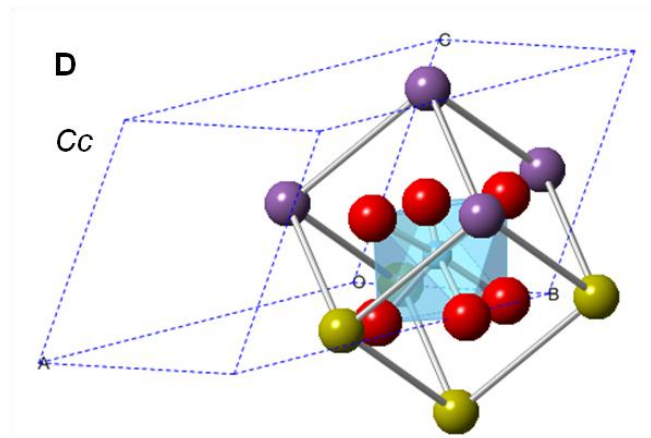
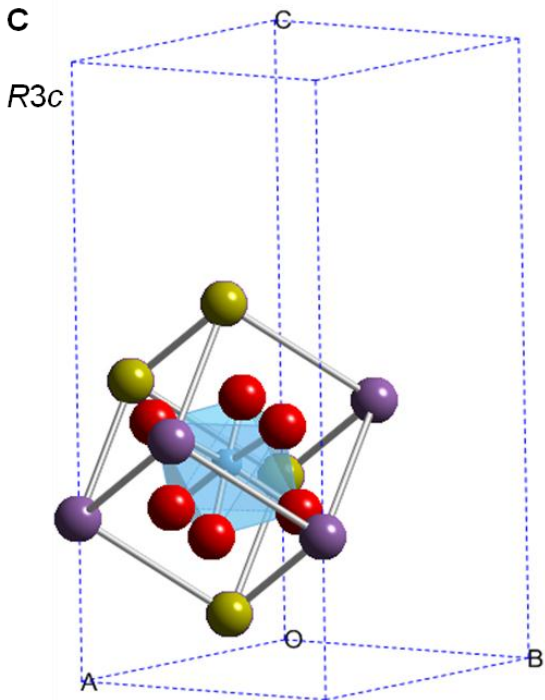
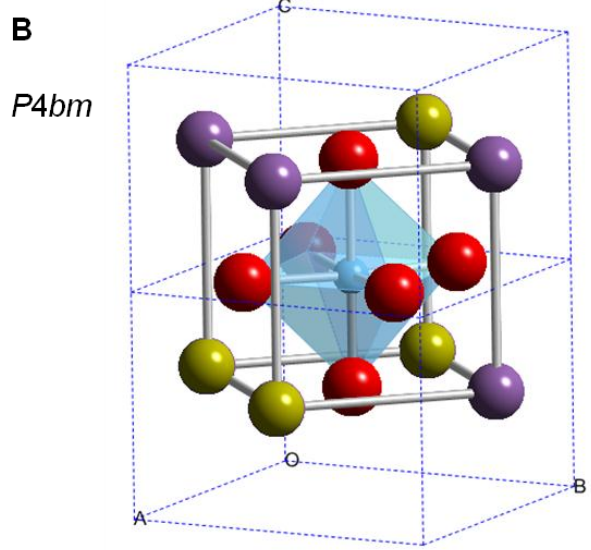
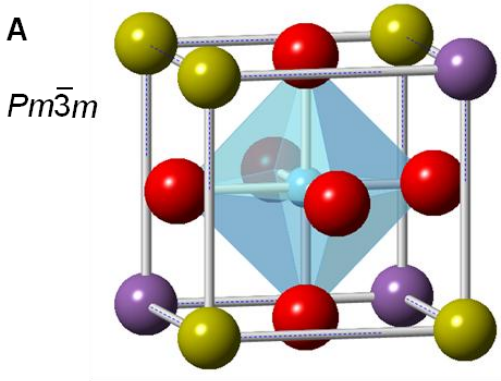


Figure 1-2. Comparison of the different phases of NBT. A) Cubic ($Pm\bar{3}m$) unit cell, B) tetragonal ($P4bm$) unit cell, C) rhombohedral ($R3c$) unit cell, and D) Monoclinic (Cc) unit cell. The pseudo-cubic unit cell is shown in each phase for comparison.

CHAPTER 2 PHASE FORMATION OF NBT DURING SOLID STATE PROCESSING

Background

Prior to delving into structure and property studies of NBT, the formation of NBT during calcination has been examined. The content of this chapter is reprinted with permission from E. Aksel and J. L. Jones, "Phase Formation of Sodium Bismuth Titanate Perovskite during Solid State Processing," *Journal of the American Ceramic Society*, Vol. 93, No. 10, pp. 3012-3016, copyright (2010) American Ceramic Society.⁴² Several processing routes for NBT have been previously reported, such as hydrothermal synthesis,⁴³ sol-gel,^{44, 45} reactive templated grain growth,⁴⁶ and the citrate method.⁴⁷ In the sol-gel synthesis route done by Rémondière *et al.*,⁴⁵ no transitory nanocrystalline phase appeared before formation of NBT. On the other hand, in the citrate method by Xu *et al.*,⁴⁷ an intermediate phase of $\text{Bi}_4\text{Ti}_3\text{O}_{12}$ (BTO) occurred in powders calcined at temperatures of 500 – 550°C. The formation of NBT via solid-state synthesis routes, however, has not yet been investigated although this is the most feasible processing method for large-scale synthesis of viable lead-free commercial ceramics.

To better understand the mechanisms present in the formation of NBT during calcination, *in situ* high temperature diffraction was applied. This is a useful method for examining phase evolution in crystalline materials.^{48, 49} For example, Wilkinson *et al.*⁴⁸ used this method to analyze the crystallization of various compositions of PZT and observed an intermediate fluorite phase prior to perovskite formation. *In situ* X-ray

Reprinted with permission from E. Aksel and J. L. Jones, *Journal of the American Ceramic Society*, **93**, 3012 (2010), copyright American Ceramic Society (2010).

diffraction (XRD) also applied by Bondioli *et al.*⁴⁹ to identify the mechanisms of formation for BaTiO₃ and observed an intermediate phase, Ba₂TiO₄, during calcination. These previous works establish a precedent for the use of *in situ* XRD in the study of phase evolution of NBT during calcination.

Experimental

Oxide powders of Bi₂O₃ (99.975% purity, Alfa Aesar, Ward Hill, MA), TiO₂ (99.85% purity, Alfa Aesar), and Na₂CO₃ (99.5% purity, Alfa Aesar) were combined in stoichiometric amounts to obtain 10 g of NBT. The mixture was ball milled in 100 mL of ethanol with 300 g of 5 mm diameter yttria-stabilized zirconia media for 20–24 h. The powder was then dried at 100°C to remove the ethanol and ground using a mortar and pestle prior to sieving with mesh size of 200 μm.

In situ powder XRD patterns were measured using a laboratory X-ray diffractometer equipped with a curved position sensitive detector (CPS120, Inel, Ardenay, France), a Cu X-ray tube source, and multilayer mirror optics for increased incident intensity. The powder was packed into an alumina crucible over a thermocouple and heated in a furnace containing an X-ray transparent window. A rate of 4°C/min was used to heat the sample continuously to a maximum temperature of 700°C. Diffraction patterns were acquired continuously during heating in sequential increments. Each diffraction pattern was measured for 60 s, representing a time-average of the structure through a 4°C range in temperature.

A peak fitting procedure was used to extract quantitative information from the measured patterns. A fourth order polynomial function was used to model the background of the entire diffraction pattern. A Pearson VII-type profile shape function

was used to fit certain individual Bragg peaks by employing a least square algorithm in the program MATLAB (The Mathworks Inc., Natick, MA; ver. 7.3.0.267).

Results and Discussion

Calcination Profile

The XRD patterns of the reactant powders prior to calcination, at an intermediate temperature of 560°C during calcination, and following calcination at 700°C are shown in Figure 2-1. In the XRD pattern recorded after calcination, the peaks are identified as NBT with no observed secondary phases. To obtain a more extensive understanding of the calcination process, all diffraction patterns measured throughout the calcination procedure are shown in Figure 2-2. The initial XRD pattern at room temperature is that of the reactant powder mixture, and is equivalent to the “before calcination” pattern in Figure 2-1D. At approximately 500°C, the formation of the NBT perovskite phase commences, with the simultaneous appearance of a secondary transient phase of low intensity. The secondary transient phase subsequently disappears at approximately 650°C. With increasing temperature, shifts in the 2θ positions of some of the reflections were also noted. For example, a reflection at $2\theta \approx 47^\circ$, corresponding to the (041) plane of Bi_2O_3 transitions continuously during heating to become the (002) plane of NBT.

Transient Phases

As observed in the *in situ* diffraction measurements in Figure 2-2, several unknown reflections appear and disappear during heating. This occurs between 500 and 650°C, with reflections at $2\theta \approx 31^\circ$ and $2\theta \approx 43^\circ$. A previous study of the formation of NBT through a sol–gel route by Rémondière *et al.*⁴⁵ did not find transient phases during the heating process. However, the transient peaks observed in the present work appeared at $\sim 500^\circ\text{C}$ and disappeared at $\sim 650^\circ\text{C}$ (Figure 2-2). In the same prior work,

the diffraction patterns were measured at discrete temperature increments of 100°C and therefore may have missed subtle transient or intermediate diffraction peaks which maximize in intensity at intermediate temperatures. The continuous and sequential collection of diffraction data during calcination in the present work allowed for such observations.

To identify the transient peaks, a diffraction pattern acquired at an intermediate temperature of 560°C during the *in situ* calcination experiment is also shown in Figure 2-1C. The transient intermediate peaks at $2\theta \approx 31^\circ$ and $2\theta \approx 43^\circ$ cannot be identified as reflections of either the reactants nor the final perovskite phase. In a study by Morozov *et al.*,⁵⁰ the formation of BTO from Bi_2O_3 and TiO_2 became noticeable at temperatures above 600°C only after the formation of intermediate $\text{Bi}_{12}\text{TiO}_{20}$ at approximately 500°C. These temperatures agree with the temperature range in which the unknown transient peaks are observed in the present study. To identify the unknown peaks, an additional experiment was undertaken in which only Bi_2O_3 and TiO_2 were calcined together without Na_2CO_3 . The powders were combined in the same fraction as in the previous NBT experiment, ball milled, and then heated using the same conditions as in the NBT experiment. The XRD pattern obtained at 700°C is shown in Figure 2-1A. The highest intensity reflections in the reaction of Bi_2O_3 and TiO_2 correspond to the transient peaks observed at $2\theta \approx 31^\circ$ and $2\theta \approx 43^\circ$ during the *in situ* NBT calcination experiment. In previous studies of the reaction between Bi_2O_3 and TiO_2 , it was observed that $\text{Bi}_{12}\text{TiO}_{20}$ forms at approximately 500°C and gradually transforms to BTO above 600°C.⁵⁰ Since the two observed peaks at $2\theta \approx 31^\circ$ and $2\theta \approx 43^\circ$ may correspond separately to the BTO and $\text{Bi}_{12}\text{TiO}_{20}$ phases, respectively, the same phase evolution

likely occurs in the present work although conclusive evidence of the phase sequence of the transient phase(s) is not presently determined. The significance of this observation is that a secondary reaction occurs between Bi_2O_3 and TiO_2 during the processing of NBT.

Figure 2-3 shows the integrated intensity as a function of temperature during the heating cycle for the following diffraction peaks: the sum of the two reactant peaks, (111) of Na_2CO_3 and (122) of Bi_2O_3 which overlap and are positioned at $2\theta \approx 33^\circ$, the (110) of NBT at $2\theta \approx 33^\circ$, and the transient peak positioned at $2\theta \approx 31^\circ$. It is apparent from this figure that NBT perovskite begins forming at approximately 425°C and is fully formed at approximately 600°C . It is also evident that the unknown transient peak becomes measurable at 500°C and is no longer present by 630°C , consistent with the temperatures at which Bi_2O_3 and TiO_2 form both $\text{Bi}_{12}\text{TiO}_{20}$ and BTO.⁵⁰ It is likely that the observed temperatures are rate-dependent and the temperatures at which the reactions are completed may be decrease if lower heating rates are used.

Mechanism

To further explore the NBT perovskite phase formation, an enlarged view of pertinent 2θ reflections is shown in Figure 2-4. The Bragg peak evolution from the starting mixture to the final perovskite phase illustrates two different types of behavior. Within certain 2θ ranges including $22^\circ < 2\theta < 24^\circ$ and $32^\circ < 2\theta < 34^\circ$, the perovskite peaks form discontinuously from the reactant peaks (e.g., Figures 2-4A and B). Within other 2θ ranges including $39^\circ < 2\theta < 41^\circ$, $46^\circ < 2\theta < 48^\circ$, and $57^\circ < 2\theta < 59^\circ$, the perovskite Bragg peaks form continuously from the peaks the reactant phases (e.g., Figures 2-4C-E). The perovskite peaks which form continuously from the reactant peaks correspond to 2θ positions where only reflections from the Bi_2O_3 reactant are present. The continuity of

the latter diffraction peaks with temperature is used in the present work to develop a proposed particle conversion mechanism for the formation of NBT. The continuous transition between the reactant and perovskite peaks suggests that one of the reactants may act as a host for the perovskite structure formation. A schematic in Figure 2-5A illustrates such a mechanism, in which the Bi_2O_3 particle acts as a structural host for the diffusion-dependent conversion process. An alternate mechanism where a perovskite particle forms via nucleation and growth (as previously proposed by Morozov *et al.*⁵⁰ for the formation of BTO) is shown in Figure 2-5B for comparison.

At room temperature, Bi_2O_3 exists in the α phase, which adopts a monoclinic symmetry.⁵¹ Previous work on Bi_2O_3 by Zhukov *et al.*⁵¹ found the presence of a metastable phase consisting of tetragonal β - Bi_2O_3 and body centered cubic γ - Bi_2O_3 between 500 and 650°C. Morozov *et al.*⁵⁰ suggested that a phase transition from α - Bi_2O_3 to γ - Bi_2O_3 occurred during the calcination of BTO. In order to examine the possibility of α -to- γ phase transition of Bi_2O_3 between 500 – 650°C, an additional *in situ* diffraction experiment was performed in the present work where Bi_2O_3 powder was heated to 700°C in the absence of the other reactant powders. However, no metastable phase was observed. Therefore, the changes observed in the transition to the perovskite phase in Figure 2-4 are unlikely to be associated with a phase transition in Bi_2O_3 .

It is proposed in the present work that Bi_2O_3 serves as a structural host for the particle conversion into the NBT perovskite. To understand the mechanism of NBT conversion, the structure of α - Bi_2O_3 is compared with that of NBT. For the diffraction peaks which show a continuous behavior during calcination, such as the ones

in Figures 2-4C-E, the corresponding α - Bi_2O_3 and NBT planes are compared in Figure 2-6. While keeping the respective α - Bi_2O_3 and the NBT unit cells at a constant orientation, the planes of the two phases which appear at closely positioned 2θ values also appear at similar orientations for all three cases. On the other hand, for discontinuous peaks, this relationship is not observed. The similarity in the orientation of the planes in the NBT and α - Bi_2O_3 phases and their continuous transition to a different lattice spacing value during the development of NBT suggests that NBT develops from a particle conversion of the Bi_2O_3 particle, supporting the mechanism shown in Figure 2-5A. This suggests that appropriate concentrations of other necessary constituent elements diffuse into Bi_2O_3 and this structure transforms into the NBT perovskite structure. Figure 2-7 shows an example of the atomic arrangement in α - Bi_2O_3 and NBT for the continuous peak at 47° . At this 2θ position the (041) plane of α - Bi_2O_3 is compared to the (002) plane of NBT. The α - Bi_2O_3 unit cell with the (041) plane is shown in Figure 2-7A. To simplify the comparison to NBT the extra oxygen atoms present in α - Bi_2O_3 are not shown in Figure 2-7B. The NBT unit cell with the (002) plane is shown in Figure 2-7C. Figures 2-7B and C highlight the similarity between the atomic arrangement in α - Bi_2O_3 and NBT around the (041) and (002) planes, respectively. The different colored circles surrounding the Bi atoms in Figures 2-7B and C are used to indicate a possible way for the positions of Bi in α - Bi_2O_3 to shift to their positions in NBT during calcination.

Transmission electron microscope micrographs of samples interrupted during sintering showed that BaTiO_3 formation during solid-state processing occurs via an analogous structural transformation of either the anatase or rutile TiO_2 particle into

perovskite BaTiO_3 .⁵² Interestingly, in both rutile and anatase TiO_2 , Ti has a coordination number of 6, as it does in BaTiO_3 . On the other hand, in the case of Bi_2O_3 , Bi has a coordination number of 5, while its coordination number in NBT is 12. This implies that the conversion mechanism in NBT may be more complex than that of BaTiO_3 as it will require a rearrangement of the O atoms surrounding Bi along with the diffusion of Na and Ti. The particle conversion of Bi_2O_3 to NBT hypothesis is also supported by the lack of a similar orientation between the planes of Bi_2O_3 and NBT for the discontinuous peaks in NBT formation. In this case the perovskite peaks form discontinuously (Figures 2-4A and B), as there are no similar bismuth oxide planes at those orientations from which they can transition.

Comparison of the ionic conduction, atomic packing factor, and ionic radii of the three reactants provides further support for the hypothesis that Bi_2O_3 may be the host for the conversion into NBT. The ionic conduction, due to the migration of O^{2-} ions, in Bi_2O_3 is higher than that of TiO_2 .^{53, 54} Since conduction in these oxides is due to migration of O^{2-} , it indicates that diffusivity of O^{2-} is higher in Bi_2O_3 than in TiO_2 . This implies that diffusivity of the other ions may also be higher in Bi_2O_3 . The ionic conductivity of Na_2CO_3 is higher than that of the other two reactants; however, in this case, ionic conduction occurs mainly through migration of the Na^+ .⁵⁵ Due to their high diffusivity in the Na_2CO_3 particle, Na^+ ions may migrate to the surface of the particle and subsequently diffuse into the Bi_2O_3 particle. The atomic packing factors of Bi_2O_3 , TiO_2 , and Na_2CO_3 are approximately 0.47, 0.65, and 0.63, respectively. This indicates that Bi_2O_3 is less densely packed than the other two reactants and has a higher void volume for interstitial diffusion into the unit cell. Also, the ionic radii of Na^+ (1.39 Å) and Ti^{4+}

(0.605 Å) are smaller than that of Bi^{3+} (1.45 Å),⁵⁶ implying that the interstitial diffusion of Na^+ and Ti^{4+} would require less energy.

The proposed diffusion-dependent particle conversion mechanism occurs under the standard processing conditions used in the present work. Because the Bi_2O_3 particle transforms in the NBT perovskite phase, the final particle size of NBT will be strongly limited by the initial particle size of Bi_2O_3 . Thus, a smaller final particle size of NBT may require a smaller starting particle size of Bi_2O_3 . However, the specific mechanism identified in the present work may also be strongly influenced by additional factors including particle size and heating rate. For example, the reaction may proceed through nucleation and growth under different circumstances than through diffusion of Na, Ti, and O into Bi_2O_3 . The particle size distribution of the starting powders may affect the formation mechanism as smaller particles that possess a higher specific surface area will behave differently during this process than larger particles.

Summary

The solid-state reaction during the formation of NBT from reagent oxides and carbonates is investigated using *in situ* XRD. Based on evidence from the X-ray measurements, it is proposed that the necessary constituent elements diffuse into Bi_2O_3 , leading to the conversion of a Bi_2O_3 particle to an NBT particle through a diffusion-dependent process. Also, a small fraction of previously unreported transient phases was observed during calcination. The extra reflections associated with these phases are observed between 500 – 650°C and are associated with a reaction between Bi_2O_3 and TiO_2 . The perovskite phase of NBT begins forming at 500°C and is the only phase present at 700°C.

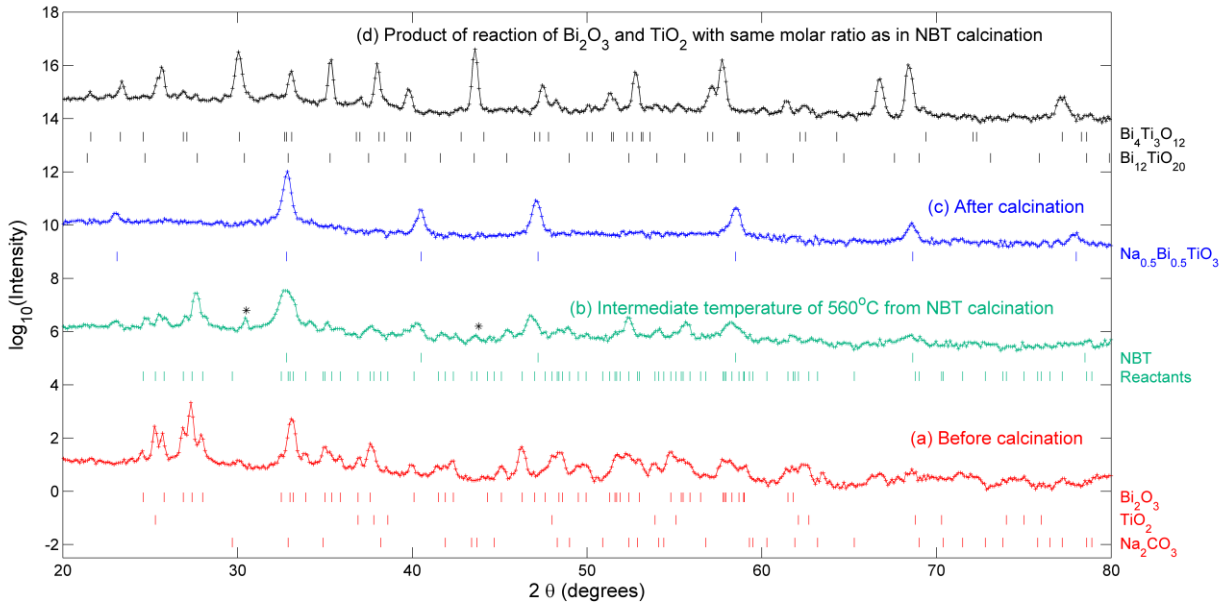


Figure 2-1. X-ray diffraction patterns at selected temperatures during the calcination process. The patterns are on a \log_{10} scale to enhance detail. A) The mixed reactant powders before calcination, B) a pattern measured during calcination at 560°C , C) after the calcination process. Transient peaks are identified in part C with an asterisk (*). D) Diffraction pattern of the product of the reaction of Bi_2O_3 and TiO_2 combined in the same molar ratio as in the NBT calcination.

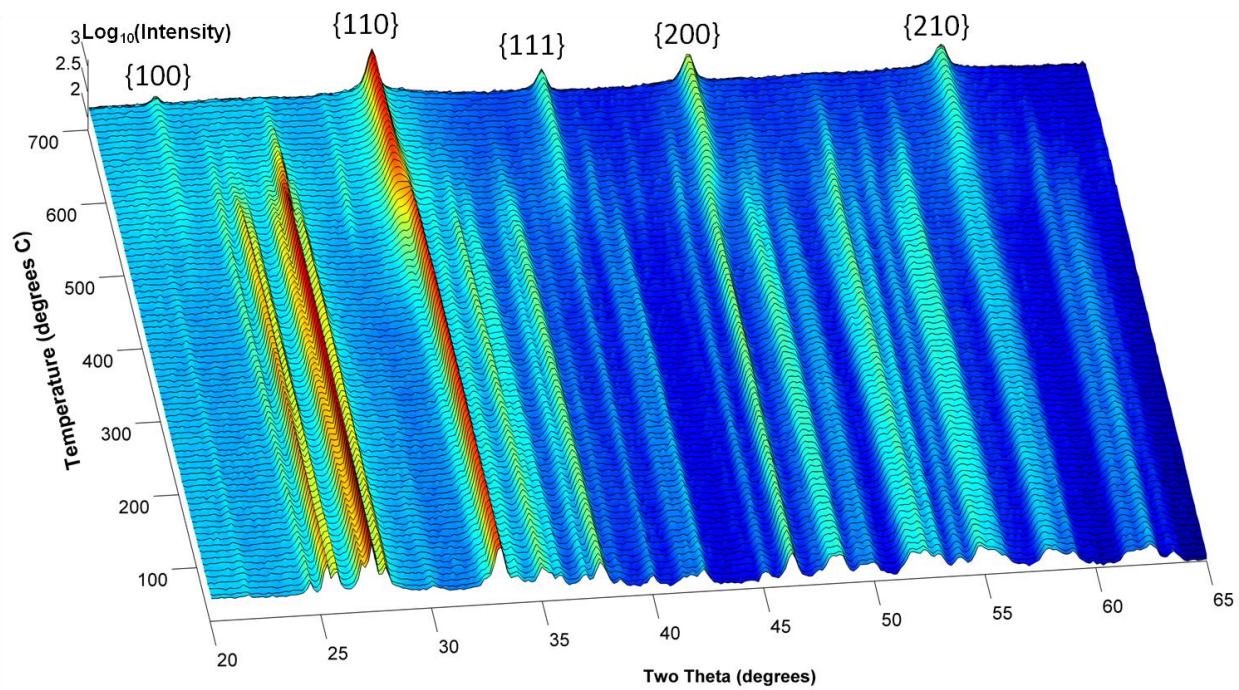


Figure 2-2. Compilation of the XRD patterns recorded during the heating of the reactant powders and solid-state synthesis of NBT. The perovskite peaks are labeled relative to the pseudo-cubic unit cell.

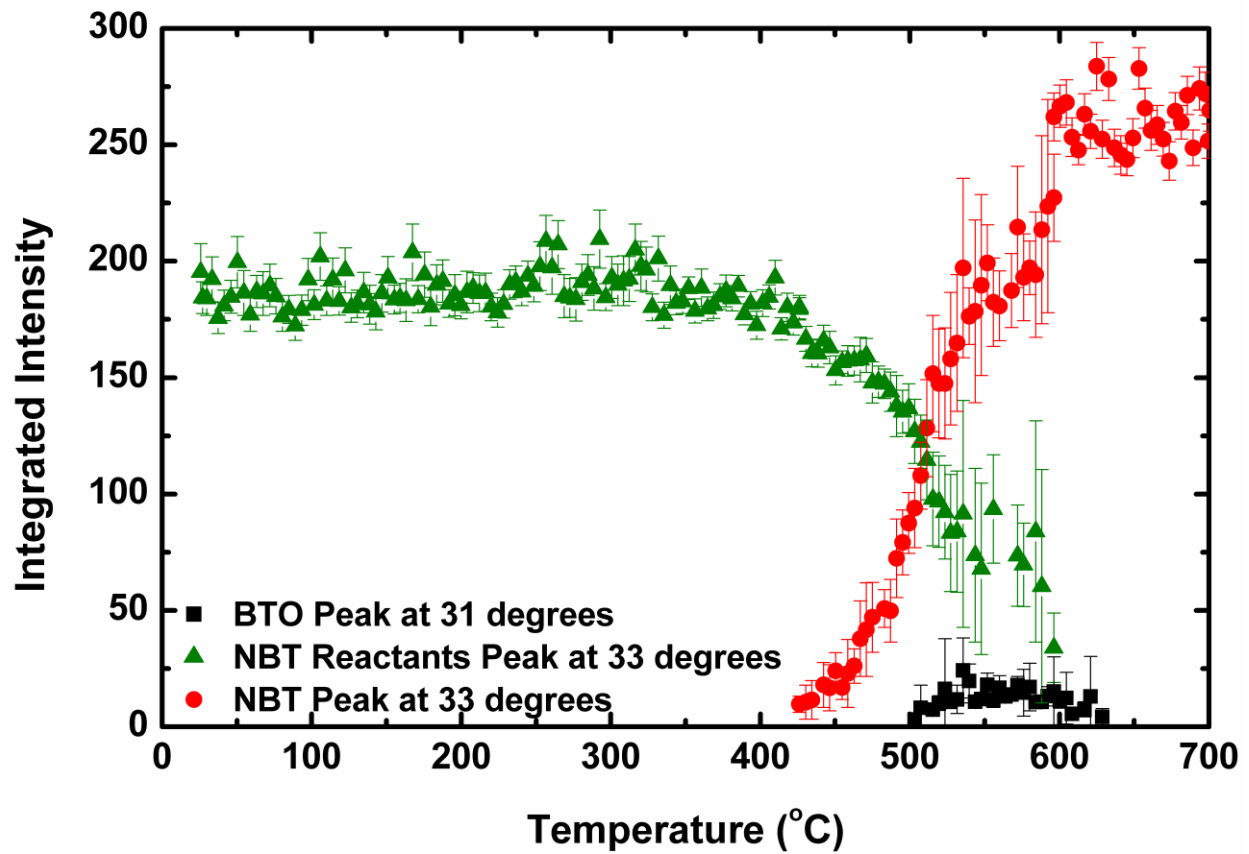


Figure 2-3. Integrated intensity of the $2\theta = 33^\circ$ reflection of NBT reactants, the 33° reflection of NBT, and the 31° reflection of the intermediate phase associated with a reaction between Bi_2O_3 and TiO_2 . Error bars show the 95% confidence interval for each fitted reflection.

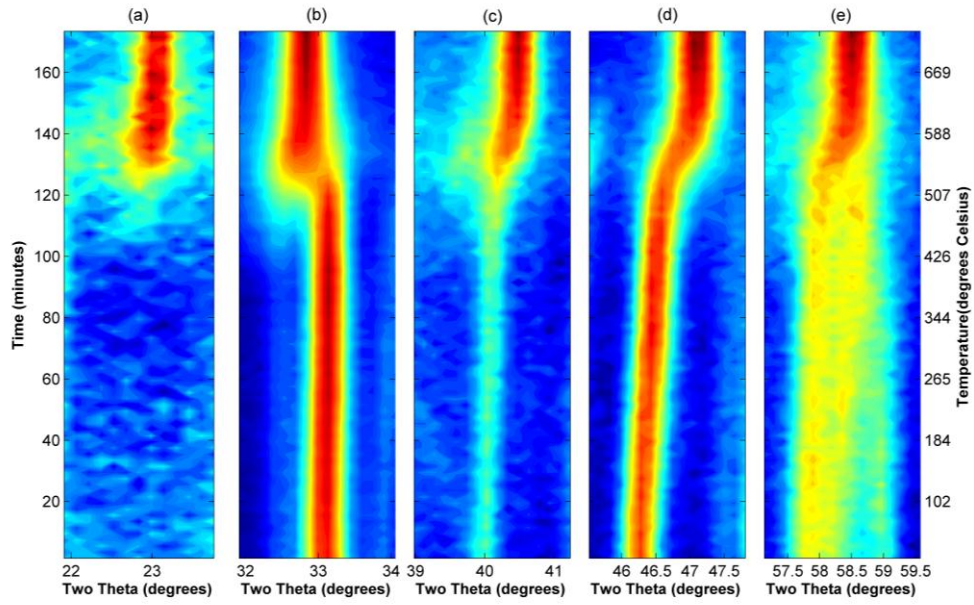


Figure 2-4. Two types of behavior observed in the formation of NBT reflections. In parts A-B the perovskite reflections form discontinuously, while in parts C-E the perovskite reflections form as a continuation of the reactant reflections.

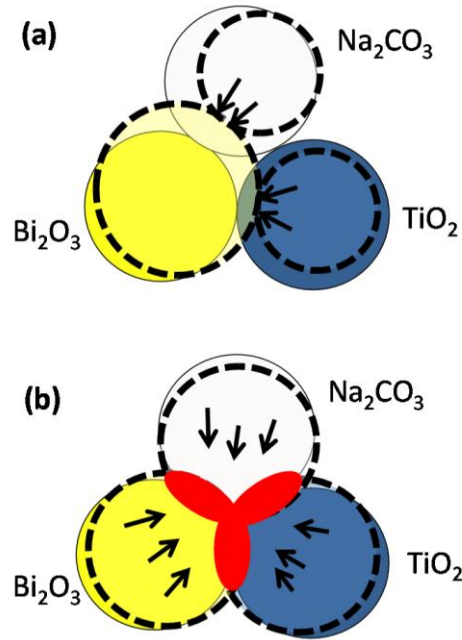


Figure 2-5. Schematic diagrams of possible phase formation mechanisms. A) Proposed conversion mechanism in which required constituents diffuse into Bi₂O₃ and this particle transforms into the NBT perovskite structure. B) An alternative nucleation and growth mechanism in which a reaction between the oxides occurs at the surface and leads to the nucleation of the final phase.

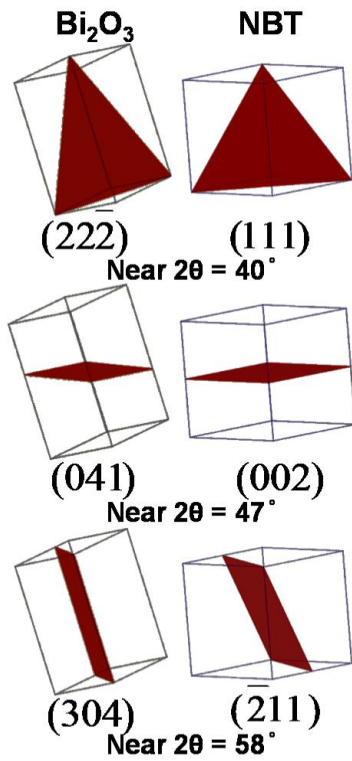


Figure 2-6. The relationship between corresponding planes of $\alpha\text{-Bi}_2\text{O}_3$ and NBT at selected 2θ angles.

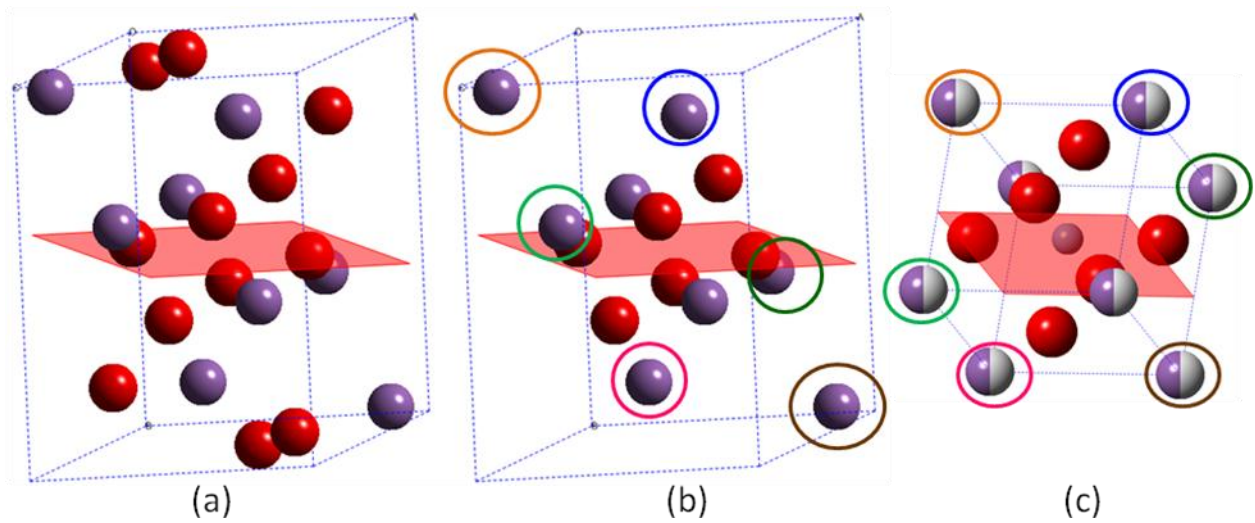


Figure 2-7. Comparison of the atomic arrangement in $\alpha\text{-Bi}_2\text{O}_3$ and NBT. A) The $\alpha\text{-Bi}_2\text{O}_3$ unit cell with the (041) plane shown. B) The $\alpha\text{-Bi}_2\text{O}_3$ unit cell with the extra oxygen atoms removed for easier comparison to NBT. C) The NBT unit cell with the (002) plane shown. The colored circles surrounding the Bi atoms in parts B and C indicate the cations with corresponding positions in $\alpha\text{-Bi}_2\text{O}_3$ and NBT.

CHAPTER 3 LONG RANGE AVERAGE ROOM TEMPERATURE STRUCTURE OF NBT USING HIGH-RESOLUTION X-RAY DIFFRACTION

Motivation

The average crystallographic room temperature symmetry of NBT has historically been stated as in the space group $R3c$.²⁴ However, recent single crystal experiments by Gorfman and Thomas suggested that the average structure of NBT single crystals is inconsistent with the rhombohedral system but is better described by the monoclinic space group Cc .²⁸ There also remains some debate over the structural transitions of NBT with changes in temperature.^{24, 26, 57, 58} This chapter presents high-resolution synchrotron XRD measurements of calcined and sintered NBT at room temperature and the corresponding crystallographic refinement of the structures using the Rietveld method. The content of this chapter is reprinted with permission from E. Aksel, J. S. Forrester, J. L. Jones, P. A. Thomas, K. Page, and M. R. Suchomel, "Monoclinic crystal structure of polycrystalline $\text{Na}_{0.5}\text{Bi}_{0.5}\text{TiO}_3$," Applied Physics Letters, Vol. 98, No. 152901, copyright (2011) American Institute of Physics.⁵⁹

Experimental

NBT ceramics were synthesized using solid-state processing. Oxide powders of Bi_2O_3 (99.975% purity, Alfa Aesar), TiO_2 (99.85% purity, Alfa Aesar), and Na_2CO_3 (99.5% purity, Alfa Aesar) were combined in stoichiometric amounts to obtain 10 g of $\text{Na}_{0.5}\text{Bi}_{0.5}\text{TiO}_3$. The particle sizes of the starting powders were examined using a scanning electron microscope (SEM), and are shown in Appendix A Figure A-1. The mixture was ball milled in 100 mL of ethanol with 300 g of 5 mm diameter yttria

Reprinted with permission from E. Aksel, J. S. Forrester, J. L. Jones, P. A. Thomas, K. Page, and M. R. Suchomel, Applied Physics Letters 98, 152901 (2011), copyright American Institute of Physics (2011).

stabilized zirconia media for 20-24 h. The powder was then dried at 100°C and ground using a mortar and pestle in order to pass through a 200 µm STM sieve. This mixture was calcined at 800°C for 2 h using heating and cooling rates of 4 and 5°C/min, respectively. An SEM image of the calcined powders is also shown in Appendix A Figure A-2. Green pellets were obtained by mixing the powders with organic binder polyvinyl alcohol and uniaxially pressing in a 10 mm diameter die using 60 MPa. The green pellets were fired at 1100°C for one h in alumina crucibles using heating and cooling rates of 4 and 5°C/min, respectively. A cracked surface of a sintered pellet was used for examination of the grain size in an SEM (Appendix A Figure A-3). The sintered pellets were crushed into fine powder and annealed at 400°C for 3 h in a closed alumina crucible to thermally anneal residual stresses induced by the grinding process.

High-resolution synchrotron XRD patterns were measured in transmission geometry on beamline 11-BM at the Advanced Photon Source at Argonne National Laboratory. To minimize X-ray absorption during the measurement, the powders were loosely packed in 0.8 mm diameter polyimide tubes pre-lined with amorphous silicone-based grease. Samples were spun at 60 Hz during data collection to improve powder crystallite averaging. The diffraction patterns were measured at room temperature using a monochromatic X-ray beam. The resolution is $\Delta Q/Q = 1.7 \times 10^{-4}$, which correlates to an instrumental contribution to peak full width at half maximum (FWHM) of approximately $0.005^\circ 2\theta$ at the measurement energy.⁶⁰ This resolution is achieved by the use of a scintillator based multicrystal analyzer detector at 11-BM,⁶¹ which represents state-of-the-art angular resolution for powder diffraction measurements. Diffraction patterns for the calcined powder were measured using an X-ray wavelength

of 0.458739 Å over the 2θ range 3.0°–30°. For the sintered powders, the wavelength was 0.413629 Å and the 2θ range was 3.0°–27.0°. Both measurements utilized a 0.001° 2θ step-size. The experiments were done at different wavelengths due to a change in the operating conditions of the beamline between the two measurements. To confirm that a change in wavelength did not affect the comparison of the two powders, calcined powders were later measured using a wavelength of 0.413614 Å and the same results were observed.

Crystal structure refinements were carried out using the Rietveld analysis program GSAS.^{62, 63} Parameters refined included the 2θ zero, scale factor, 16 polynomial background parameters in a shifted Chebyshev model (diffuse scattering resulted in an irregular background, requiring this large number of polynomial parameters), lattice parameters, atomic positions, isotropic atomic displacement parameters, and cation site occupancies. Due to the low X-ray scattering factor of Na, the atomic position and displacement parameter of Na were constrained to equal those of Bi in all the refinements, but the site occupancies were refined independently. An explanation of the least squares refinement approach and criteria of fit used in Rietveld analysis is given in Appendix A. See Appendix B for all refinement outputs and quality of fit indicators in Tables B-1–B-3.

Results and Discussion

Figure 3-1 shows the results of two crystallographic refinements using the diffraction pattern of calcined NBT; one refinement used the $R3c$ space group as the model (Figure 3-1A) and the other used the Cc space group as the model (Figure 3-1B). For consistency in discussing specific reflections from different space groups, the

reflection indices shown in the figures and subsequent discussion are relative to the pseudo-cubic perovskite unit cell. The rhombohedral $R3c$ space group for the calcined NBT produces a good fit with an $R_p = 5.56\%$. Using the monoclinic Cc space group allows for slight improvement of the fit to an $R_p = 5.16\%$. Thus, both space groups show reasonably similar quality of fits for the XRD patterns of calcined powders.

Figure 3-2 shows the results of three crystallographic refinements using the XRD pattern of sintered NBT; one refinement used the $R3c$ space group (Figure 3-2A), a second refinement used two independent $R3c$ space groups (Figure 3-2B), and the third one used the Cc space group (Figure 3-2C). A comparison of the insets in Figures 3-1 and 3-2 highlights a major difference in the patterns from the calcined (Figure 3-1) and sintered (Figure 3-2) materials. The 110 diffraction peak of the calcined powder (Figure 3-1) is relatively broad and symmetric, which allows it to be nearly equally modeled using either the $R3c$ or Cc space group. Peak broadening in the diffraction patterns of calcined NBT caused by small grain size or micro-strains may have contributed to some misinterpretation of the structure in the past. However, the 110 diffraction peak of the sintered powder (Figure 3-2) clearly shows the existence of at least three separate peaks.

Since the $R3c$ space group only allows for two 110 peaks, the model shown in Figure 3-2A cannot fully account for the measured XRD pattern, which explains the high R_p value of 8.44%. Figure 3-2B shows the crystallographic refinement wherein two independent $R3c$ phases were employed. Such a case may exist, for example, if surface effects such as volatilization create a two phase structure. It was possible to fit the pattern to two independent $R3c$ phases ($R_p = 5.97\%$) by allowing the lattice

parameters of the two phases to vary to significantly different values and allowing the occupancy of Bi to reduce by 5% in one of the phases. The Bi-deficient phase (see “phase 2” in Appendix B) exhibits lattice parameters that display a reduced ferroelastic distortion, but a similar cell volume to “phase-1” and phases obtained in other refinements. While two independent $R3c$ phases could reasonably fit the diffraction pattern, it is unlikely that this combination of phases accurately represents the actual material structure. For example, other authors have reported that a Bi deficiency does not significantly affect spontaneous strain.⁶⁴ Moreover, since the ceramics were sintered as pellets, it would be expected that the amount of the bismuth deficient phase should be low because of the small surface to volume ratio. However, the calculated phase fraction (29% by volume) of the bismuth deficient phase is higher than expected for such a case. The surface area to volume increases after the sintered ceramics are crushed into powder. However, subsequent thermal treatment (annealing at 400°C) is well below the Bi_2O_3 volatilization temperature of 825°C and similarly, it is below the Na_2O volatilization temperature of 1132°C.⁶⁵

Figure 3-2C shows the refinement of sintered NBT using the Cc setting proposed by Gorfman and Thomas.²⁸ The starting model was obtained by refining the neutron diffraction data from Jones and Thomas²⁴ against a Cc model adapted from that of Pandey *et al.* for PZT.⁶⁶ The quality of fit of this refinement is superior to the other two refinements for the sintered material XRD pattern ($R_p = 5.87\%$). The refined lattice parameters of the Cc setting are provided in Table 3-1 and the atomic positions along with the occupancies are given in Table 3-2. The previously reported NBT structure in the $R3c$ space group has an octahedral tilting system of $a^-a^-a^-$ with a tilt angle of 8.24°

(Ref. ²⁴) while the *Cc* space group has the tilting system $a^-a^-c^-$.⁶⁷ This indicates that both space groups have out-of-phase tilting in the x, y, and z directions although the magnitude of the tilt angle in the z-direction of the *Cc* space group is unique.⁶⁸

Several other two-phase combinations were considered and similarly dismissed as possible structural models. Since *Cm* could account for the splitting of the 110 peak in NBT, it is possible to use a combination of *R3c* and *Cm* to model both the 3/2 1/2 1/2 superlattice reflection and the 110 splitting. This model was used previously to model the morphotropic phase boundary (MPB) region in PZT.⁶⁹ However, the observed intensity profile near the pseudo-cubic 3/2 1/2 1/2 peak has an obvious profile which cannot be fully described using combinations of other space groups including the *R3c* and *Cm* model.⁶⁹ The *Cc* space group, on the other hand, has five contributing reflections to the pseudo-cubic 3/2 1/2 1/2 superlattice peak⁷⁰ which can explain the apparent asymmetry in the intensity profile.

Monoclinic perovskite structures have been observed in several other material systems. For example, Noheda *et al.* observed a monoclinic phase at the PZT MPB between rhombohedral and tetragonal phases using synchrotron X-ray diffraction.⁷¹ This observation, and a similar finding in the “giant” piezoelectric materials $\text{Pb}(\text{Zn}_{1/3}\text{Nb}_{2/3})\text{O}_3\text{-xPbTiO}_3$ and $\text{Pb}(\text{Mn}_{1/3}\text{Nb}_{2/3})\text{O}_3\text{-xPbTiO}_3$,⁷² ignited discussion over whether the existence of a monoclinic phase is a necessary or sufficient condition for large piezoelectricity. For NBT, the present work reports a monoclinic structure, although many earlier works have shown that unmodified NBT exhibits low piezoelectric coefficients.⁷³ Thus, the present structure shows no clear correlation between monoclinicity and high piezoelectricity in NBT. This result is not surprising given the

recent evidence that the presence of a long-range monoclinic phase itself does not account for high piezoelectricity but rather the “presence of structural instabilities” near MPBs is more important.⁷⁴

However, the monoclinic structure of NBT will strongly influence the domain structure and domain mobility. It is known that the degree of ferroelastic distortion has been correlated to the mobility of domain walls.^{75, 76} Because the ferroelastic lattice distortion in monoclinic NBT is exceedingly small (so much so that it is difficult to measure the distortion using conventional X-ray diffractometers), domain walls in NBT exhibit the potential for high mobility. However, since the mobility of domain walls is also controlled by additional factors such as defects, high domain wall mobility may not necessarily be observed in NBT. It may also be considered that the degree of ferroelastic distortion may be correlated to the domain size. Thus, the presence of nanodomains in NBT^{25, 77} may be at least partially contributed from the small degree of ferroelastic distortion of the *Cc* structure. The *Cc* space group assignment will also have implications to solid solutions of NBT with other perovskites and, in particular, the characteristics of related MPBs. For example, the (1-x)NBT-xBaTiO₃ solid solution exhibits an MPB at a composition of $x \approx 7\%$.^{12, 78, 79} The characteristics of this phase boundary will be affected by the space group assignment in NBT-rich compositions.

Summary

High-resolution X-ray diffraction was used to identify and model the structure of NBT using the *Cc* space group. Two following primary factors enabled the observation of the *Cc* space group: (1) the use of sintered samples, which reduce the microstructural contribution to peak broadening, and (2) the high-resolution of the X-ray diffraction instrument, which reduces the instrumental contribution to peak broadening

and allows subtle peak splitting to be measured. While a monoclinic structure has been considered in the past,⁸⁰ and single crystals have been observed to exhibit peak splitting indicative of the *Cc* space group,²⁸ the present work provides a refined structure for the *Cc* space group using powder synthesis and diffraction. The identification of the *Cc* space group has implications for the domain structure, properties, and phase equilibria in NBT solid solutions.

Table 3-1. Summary of refined lattice parameters and Bragg fitting values from the Cc refinement of sintered NBT.

a (Å)	b (Å)	c (Å)	Angle (β) (degrees)	Fitting Values
9.5261(2)	5.48308(4)	5.50794(5)	125.3442(5)	R_p 5.87% R_{wp} 8.09% χ^2 4.21

Table 3-2. Summary of refined atomic positions and occupancies resulting from the Cc refinement of the sintered material. Wyckoff positions are indicated beside each element.

	Site Positions			Occ.
	x	y	z	
Na	0	0.25	0	0.494(6)
Bi	0	0.25	0	0.498(1)
Ti,4(a)	0.2703(4)	0.2474(9)	0.7427(8)	1.004(2)
O1,4(a)	0.008(3)	0.194(1)	0.493(5)	1
O2,4(a)	0.177(1)	0.481(2)	-0.137(2)	1
O3,4(a)	0.241(1)	-0.003(2)	-0.044(2)	1

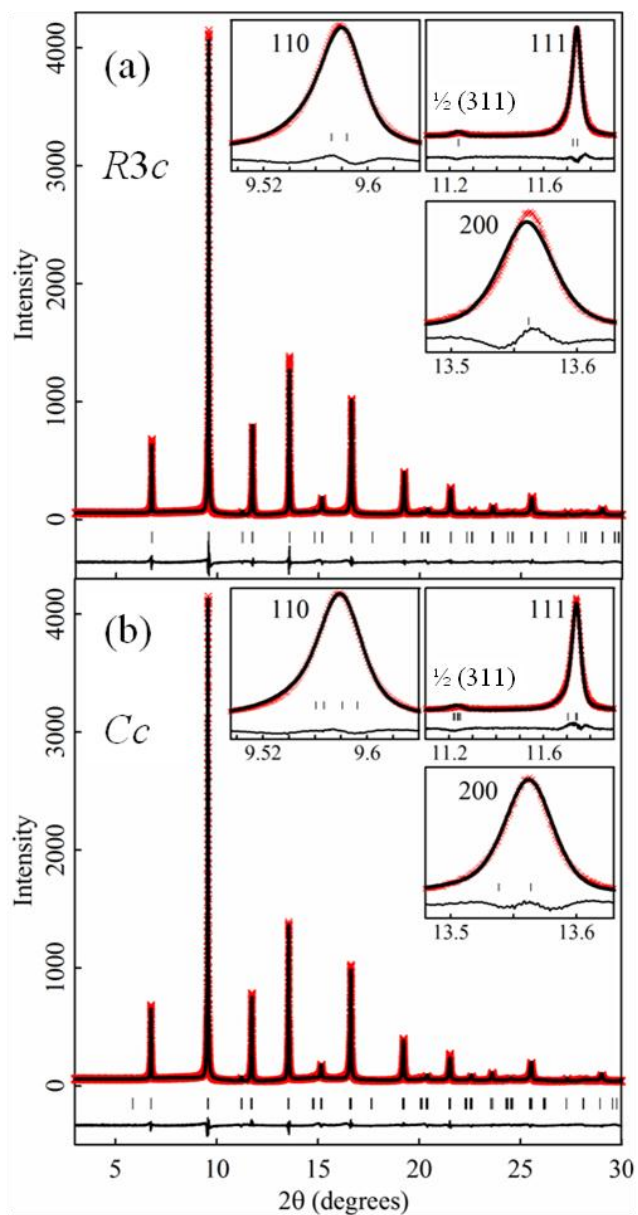


Figure 3-1. Synchrotron XRD pattern of calcined NBT powder and results of crystal structure refinement. The refinements were done using the space groups A) *R3c* and B) *Cc*. The labeled peak indices are relative to the pseudo-cubic perovskite unit cell.

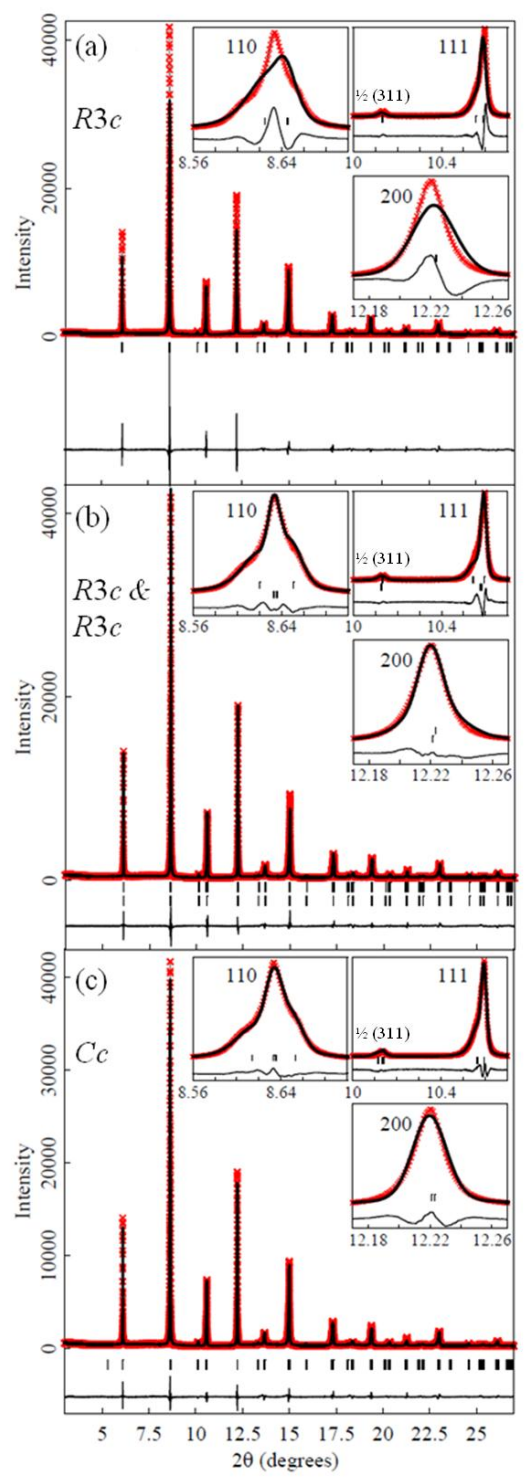


Figure 3-2. Synchrotron XRD pattern of sintered NBT powder and results of crystallographic refinement. The refinements were done using A) an $R3c$ space group, B) a mixture of two $R3c$ phases, and C) a Cc space group. The labeled peak indices are relative to the pseudo-cubic perovskite unit cell.

CHAPTER 4 AVERAGE STRUCTURE OF NBT USING X-RAY AND NEUTRON DIFFRACTION

Motivation

In Chapter 3 the application of high resolution X-ray diffraction allowed for the examination of the average room temperature structure of NBT and its identification and refinement using the *Cc* space group, rather than the previously accepted *R3c* symmetry. Although this method is sensitive to slight distortions in the material, owing to the high resolution of the described instrument, it is not suitable for detailed analyses of the light elements in NBT. The X-ray scattering factor of oxygen, 4.089, is lower than those of sodium, bismuth and titanium, (6.881, 62.425 and 13.198, respectively)⁸¹ thus making an accurate refinement of the oxygen positions and isotropic displacement parameters difficult using Rietveld refinement of XRD patterns. In the case of neutron diffraction, on the other hand, oxygen has a neutron scattering factor comparable to the other elements (i.e. 5.80 for O and 8.53 for Bi).⁸² Therefore, the coupling of the two methods can allow for a more detailed structural description of NBT. This chapter presents the results of a combined structural refinement of X-ray and neutron diffraction measurements using the Rietveld method.

Experimental

NBT ceramics were prepared using the procedure given in Chapter 3. A description of the experimental procedure and instrumental parameters of the XRD measurements is also provided in Chapter 3. Neutron scattering data were measured at room temperature and at 15 K on the neutron powder diffractometer, NPDF⁸³ at the Lujan Center at Los Alamos National Laboratory. Two g of the powder sample was loaded into a vanadium can and measured for approximately 8 h. NPDF is a total

scattering instrument and measures scatter in four banks, but only data measured in bank 3 was used for the analysis presented here. Modeling of the average structure of NBT was performed using the Rietveld analysis program GSAS,^{62, 63} using the room temperature X-ray and neutron diffraction data in combination. Anisotropic displacement parameters were refined within the model and no constraints were placed restricting Na and Bi to refine to equal displacement values (as opposed to the constraints in the XRD refinement presented in Chapter 3). An isotropic displacement parameter was used for the Ti atomic position due to the small displacement observed in Ti compared to Na and Bi. Then, the refined atomic positions and displacement parameters were used to plot thermal ellipsoids within the software package ORTEP-III to visualize atomic displacement within the crystal structure structure.⁸⁴

Results and Discussion

The results of the refinement of the neutron diffraction data are shown in Figure 4-1. This refinement was done using the *Cc* space group so that the results could be compared with the X-ray and the combined data refinements. However, since the resolution of NPDF is lower than that of 11BM, the neutron data can also be modeled well using the *R3c* space group ($R_p = 4.12\%$). The results of the combined X-ray and neutron refinement are shown in Figure 4-2 in *d*-spacing. These results may be compared to the refinements in which X-ray and neutron data were modeled independently. Table 4-1 shows the lattice parameters and angle, β , calculated using the three methods and the criteria of fit values for each refinement are given in Table 4-2. From Table 4-1, it can be observed that the refinements of the X-ray and neutron data independently provide different lattice parameters. Since the XRD measurements were carried out using a high resolution diffraction instrument, they are especially

sensitive to slight distortions in the crystal structure and can allow the extraction of very accurate lattice parameters. The combined refinement resulted in lattice parameters that are almost identical to those from the XRD refinement.

The atomic positions obtained from the three refinements are shown in Table 4-3. A comparison of the oxygen positions calculated from X-ray and neutron diffraction data again shows significant variation in the refined values. It is notable that the O refined positions in the neutron refinement are similar to those of the combined refinement. This is not surprising, as the low X-ray scattering factor of O will increase the inaccuracy of the XRD analysis in terms of atomic positions of light elements. These features further emphasize the benefits of performing combined structural refinements.

Another important aspect of the structure that can be obtained from such a refinement is the displacement of the atoms in NBT. Due to the insensitivity of X-rays to Na and O (low scattering factors), the displacement parameter of Na was constrained to equal that of Bi in the XRD refinements. The parameters for the three unique O positions were set to small values. Neutron data, on the other hand, can allow for an analysis of the displacement parameters. Since the neutron data was of high quality and the atoms have high scattering factors, refinement of anisotropic displacement parameters was possible. The anisotropic displacement can be represented as the tensor B_{ij} , given as:

$$\mathbf{B}_{ij} = \begin{pmatrix} B_{11} & B_{21} & B_{31} \\ B_{12} & B_{22} & B_{32} \\ B_{13} & B_{23} & B_{33} \end{pmatrix} \quad (4-1)$$

In this representation, the B_{11} , B_{22} and B_{33} terms represent the displacement of the ellipsoid in three orthogonal axes. For the calculated displacement values to have a physical meaning, they must obey the following three relationships:⁸⁵

$$B_{ii} > 0 \quad (4-2)$$

$$B_{ii}B_{jj} > B_{ij}^2 \quad (4-3)$$

$$B_{11}B_{22}B_{33} + B_{12}^2B_{13}^2B_{23}^2 > B_{11}B_{23}^2 + B_{22}B_{13}^2 + B_{33}B_{12}^2 \quad (4-4)$$

The thermal parameter, B , can be related to the atomic vibration parameter, U , by:

$$B = 8\pi^2U \quad (4-5)$$

Due to these constraints, all of the displacement parameters were initially refined isotropically, and were then transformed to anisotropic terms for later refinement. Due to the small isotropic displacement of Ti, it was not possible to refine it using anisotropic terms which obeyed Equations 4-2 – 4-4. Therefore, the displacement parameter of Ti was refined as isotropic in all refinements.

The displacement parameters, which were refined using the combined XRD and neutron data, are given in Table 4-4. In order to more easily visualize these parameters, they were plotted using the software package ORTEP-III (Oak Ridge Thermal Ellipsoid Plot Program for Crystal Structure Illustrations). The resulting ellipsoids are shown in Figure 4-3 on a pseudo-cubic reference unit cell. For clarity, the thermal ellipsoids of Na and Bi atoms are shown on separate unit cells, although they are defined as a random mixture in the refinements. Based on this figure, it is clear that Na and Bi have very different thermal vibration. Although both show fairly anisotropic displacement, Bi exhibits much larger anisotropic displacement than Na. Also, by comparing the projected views along the three $\langle 001 \rangle$ directions, it can be observed that the three

oxygen positions also have unique thermal vibration. All three ellipsoids appear anisotropic and the ellipsoid of O1 is much smaller than those of O2 and O3 (the different atomic positions of the three O's are described in Table 4-3). It is also worthwhile to note that in the projection shown in Figure 4-3E the displacement of Bi is smallest in the plane in which O1 shows the small ellipsoid, as compared to the other two projections.

The displacement parameters were also refined using the neutron data, independent of the X-ray data, and the results are given in Table 4-5. The ellipsoids from this refinement are shown in Figure 4-4. These results are similar to those obtained from the combined refinement. One subtle difference is that the ellipsoids of Na, O2, and O3 appear slightly bigger in Figure 4-4 than in Figure 4-3, relative to the Bi ellipsoid.

The change in thermal vibration was also investigated at a temperature of 15 K. Previous work from Jones and Thomas examined the structure of NBT single crystals using neutron diffraction and did not report any structural transitions with decreasing temperature to 5 K.²⁴ Therefore, the neutron diffraction pattern measured at 15 K in this work was modeled using the *Cc* space group. The lattice parameters and fitting values of this refinement are given in Table 4-6 and the atomic position and displacement parameters in Table 4-7. The lattice parameters reported in Table 4-6 are smaller than those calculated for the room temperature pattern (Table 4-1), as expected based on thermal expansion. At this temperature, the displacement parameter of Na also became very small. Since it was difficult to obtain a stable refinement using anisotropic terms for Na that obeyed Equations 4-2 – 4-4, the displacement parameter of Na was refined as

isotropic. When the thermal ellipsoids for this temperature (Figure 4-5) are compared with those at room temperature (Figure 4-4), they are found to be significantly smaller due to the lower thermal energy available at 15 K for displacement. The ellipsoids of Bi still maintain a strong anisotropy, and, interestingly, the ellipsoids of O2 and O3 appear large relative to the Bi at 15 K. It is possible that the O ellipsoids are large because the structure has transitioned to one of a lower symmetry and the *Cc* space group is no longer the appropriate structure for this temperature, but the resolution of NPDF is insufficient to confirm this change. It is clear, however, that the differences in the thermal vibration of Na and Bi remain even at 15 K.

The environment of the A-site can be examined by a comparison of the different bond lengths between the A-site and the oxygens. In the perovskite structure, the A-site has a coordination number of 12 with four different bonds with each of the three unique O positions. In the refinement, the Na and Bi are constrained to share the same special position in the unit cell, which is not refined due to space group restrictions. The distance from this position to the refined O positions can then be used to obtain (Na/Bi)-O bond lengths. Using the results of the combined refinement for both the O1 and O2 positions, the bond lengths are calculated as two distinct values of approximately 2.5 Å and two of ~3.0 Å. For the O3 position, the four bond lengths appear to all be close to the 2.7-2.8 Å range. This result is consistent with the atomic positions refined using only the neutron data. These trends in the bond distances may be indicators of the different bonding environments of Na and Bi. In Chapter 5 the local structure of this material is discussed and a model is used in which Na and Bi are examined as two unique sites. Those results indicate that on a local scale, the distances

of the Na-O bonds are spread symmetrically around the average bond length, while the Bi-O bonds have a bi-modal distribution. The bond length calculations in this section indicate that when Na and Bi share the same atomic position, the O1, O2, and O3 are probably forced to atomic positions which can satisfy the unique bonding environments of the A-site Bi and Na.

Another component of the structure that can be determined from the refinements is the degree of oxygen octahedral tilting. One method for calculating this tilting angle is from the atomic positions of O relative to the undistorted B-site position. In the case of a cubic cell, the ideal Ti position is at 0.5 0.5 0.5 (the fractional coordinates of this position are 0.25 0.25 0.75 in the monoclinic setting). An angle, α , can then be measured between the ideal Ti, the refined O position, and another Ti (a simplified schematic of this angle is shown in Figure 4-6). This α angle can then be used to calculate the tilting angle, ω , using the following relation,

$$\omega = \frac{180 - (\alpha)}{2} \quad (4-6)$$

Since there are three unique O positions in the *Cc* setting (*cf.* Table 4-3), three tilt angles can be calculated. The *Cc* space group has an $a^-a^-c^-$ tilting system, and should therefore have two unique tilting angles. Using the combined room temperature refinement, the tilting angles calculated are approximately 10°, 12° and 2°. With the neutron data alone, the tilting angles are calculated as approximately 11°, 11°, and 3°. At 15 K the tilting angles change considerably to 10°, 15°, and 8°. It appears that at room temperature the tilting angles correspond to the tilting system expected for the *Cc* space group, but at 15 K the tilting increases and the structure appears to be more distorted. The increased distortion is consistent with the large O thermal displacement

parameters seen in Figure 4-5. In the work of Jones and Thomas, where NBT was modeled using the $R3c$ space group, a slight increase in the tilting angle with decreasing temperature was also observed.²⁴ This behavior of increased octahedral tilting at lower temperatures was also reported in other systems, such as $\text{Bi}_{0.9}\text{Nd}_{0.1}\text{FeO}_3$.⁸⁶

Summary

A combined refinement approach was used to explore specific aspects of the structure of NBT at room temperature. The results in this chapter showcase the benefits of using such an approach as opposed to relying on X-ray or neutron diffraction alone. The refined parameters were used to examine atomic isotropic and anisotropic displacement, bond lengths, and octahedral tilting in NBT. A comparison of the displacement parameters showed that although Na and Bi share the same site, Bi experiences larger anisotropic thermal vibration in NBT than Na. A large anisotropy was also present in the thermal ellipsoids of O. An analysis of the (Na/Bi)-O bond lengths indicated the unique bonding environment of the A-site in this material. This bonding environment is investigated in detail using local structure measurements in Chapter 5. The room temperature structure was also compared to that at 15 K and a decrease in thermal displacement and lattice parameter values was observed. A comparison of the octahedral tilting angles at room temperature to the 15 K structure shows that an increase in distortion occurs with cooling, which may be associated with a low temperature phase transition.

Table 4-1. Lattice parameters of NBT at room temperature determined from a structural refinement using only X-ray diffraction data, only neutron diffraction data, and a combination of the two sets of data.

	X-ray refinement	Neutron refinement	Combined refinement
a (Å)	9.5261(2)	9.5088(6)	9.5237(2)
b (Å)	5.48308(4)	5.4771(2)	5.48217(4)
c (Å)	5.50794(5)	5.5011(2)	5.50666(5)
Angle β (°)	125.3442(5)	125.230(4)	125.3422(6)

Table 4-2. Fitting values of the refinement of NBT at room temperature using only X-ray diffraction data, only neutron diffraction data, and a combination of the two sets of data.

	X-ray refinement	Neutron refinement	Combined refinement
Fitting	R_p 5.87%	R_p 4.08%	X-ray R_p = 5.52%
Values	R_{wp} 8.09%	R_{wp} 5.57%	R_{wp} = 7.61%
			Neutron R_p = 4.11%
			R_{wp} = 5.72%
			Total R_p = 4.54%
			R_{wp} = 6.23%

Table 4-3. Atomic positions for NBT at room temperature determined from a structural refinement using only X-ray diffraction data, only neutron diffraction data, and a combination of the two sets of data.

	X-ray refinement			Neutron refinement			Combined refinement		
	x	y	z	x	y	z	x	y	z
Na	0	0.25	0	0	0.25	0	0	0.25	0
Bi	0	0.25	0	0	0.25	0	0	0.25	0
Ti	0.2703(4)	0.2474(9)	0.7427(8)	0.253(1)	0.256(2)	0.729(2)	0.2555(4)	0.2524(8)	0.7300(5)
O1	0.008(3)	0.194(1)	0.493(5)	-0.0019(9)	0.1986(4)	0.456(2)	-0.0024(4)	0.1997(2)	0.4568(8)
O2	0.177(1)	0.481(2)	-0.137(2)	0.2021(5)	0.482(1)	-0.065(2)	0.1985(2)	0.4862(6)	-0.077(1)
O3	0.241(1)	-0.003(2)	-0.044(2)	0.2588(6)	0.005(1)	-0.016(3)	0.2586(2)	0.0095(5)	-0.012(1)

Table 4-4. Anisotropic displacement parameters for NBT at room temperature, determined from a combined X-ray and neutron Rietveld refinement.

Anisotropic Displacement Parameters (\AA^2)						
	U_{11}	U_{22}	U_{33}	U_{12}	U_{13}	U_{23}
Na	0.019(5)	0.010(3)	0.020(5)	0.003(3)	0.011(5)	0.005(6)
Bi	0.053(1)	0.0330(6)	0.069(1)	0.013(1)	0.049(1)	0.006(3)
Ti	0.0021(2)	0.0021(2)	0.0021(2)	-	-	-
O1	0.0018(8)	0.0056(5)	0.005(2)	0.001(1)	0.001(1)	0.001(1)
O2	0.0159(7)	0.017(1)	0.024(2)	-0.003(1)	0.015(2)	-0.011(1)
O3	0.0162(9)	0.014(1)	0.018(2)	0.003(2)	0.011(2)	0.012(2)

Table 4-5. Anisotropic displacement parameters for NBT at room temperature, determined from a Rietveld refinement of the neutron diffraction data.

	Anisotropic Displacement Parameters (\AA^2)					
	U_{11}	U_{22}	U_{33}	U_{12}	U_{13}	U_{23}
Na	0.02(1)	0.024(8)	0.04(1)	0.01(1)	0.03(1)	0.01(2)
Bi	0.053(1)	0.0330(6)	0.069(1)	0.013(1)	0.049(1)	0.006(3)
Ti	0.0027(5)	0.0027(5)	0.0027(5)	-	-	-
O1	0.002(2)	0.007(1)	0.004(3)	-0.001(3)	0.000(2)	-0.001(3)
O2	0.023(2)	0.022(2)	0.029(4)	-0.003(3)	0.020(3)	-0.010(3)
O3	0.025(3)	0.021(3)	0.024(4)	0.001(5)	0.016(4)	0.011(4)

Table 4-6. Summary of the refined lattice parameters and fitting values of NBT at 15 K from a Rietveld refinement of the neutron diffraction data.

a (Å)	b (Å)	c (Å)	Angle β (°)	Fitting Values
9.4785(6)	5.4669(4)	5.49886(33)	124.9991(35)	$R_p = 4.09\%$ $R_{wp} = 5.63\%$

Table 4-7. Atomic positions and anisotropic displacement parameters for NBT at 15 K, determined from a Rietveld refinement of the neutron diffraction data.

	Site Positions			Anisotropic Displacement Parameters* (\AA^2)					
	x	y	z	U_{11}	U_{22}	U_{33}	U_{12}	U_{13}	U_{23}
Na	0	0.25	0	0.0052(9)	0.0052(9)	0.0052(9)	-	-	-
Bi	0	0.25	0	0.011(5)	0.025(5)	0.024(3)	0.012(4)	0.009(3)	0.007(9)
Ti	0.238(1)	0.262(2)	0.7095(9)	0.0002(5)	0.0002(5)	0.0002(5)	-	-	-
O1	-0.0226(8)	0.1952(4)	0.454(2)	0.003(2)	0.006(1)	0.007(2)	0.002(3)	0.001(2)	0.001(4)
O2	0.1854(5)	0.482(1)	-0.088(1)	0.011(2)	0.016(2)	0.011(2)	-0.004(2)	0.008(2)	-0.008(2)
O3	0.2454(7)	-0.018(6)	-0.056(1)	0.024(3)	0.023(4)	0.026(3)	0.005(3)	0.018(3)	0.015(3)

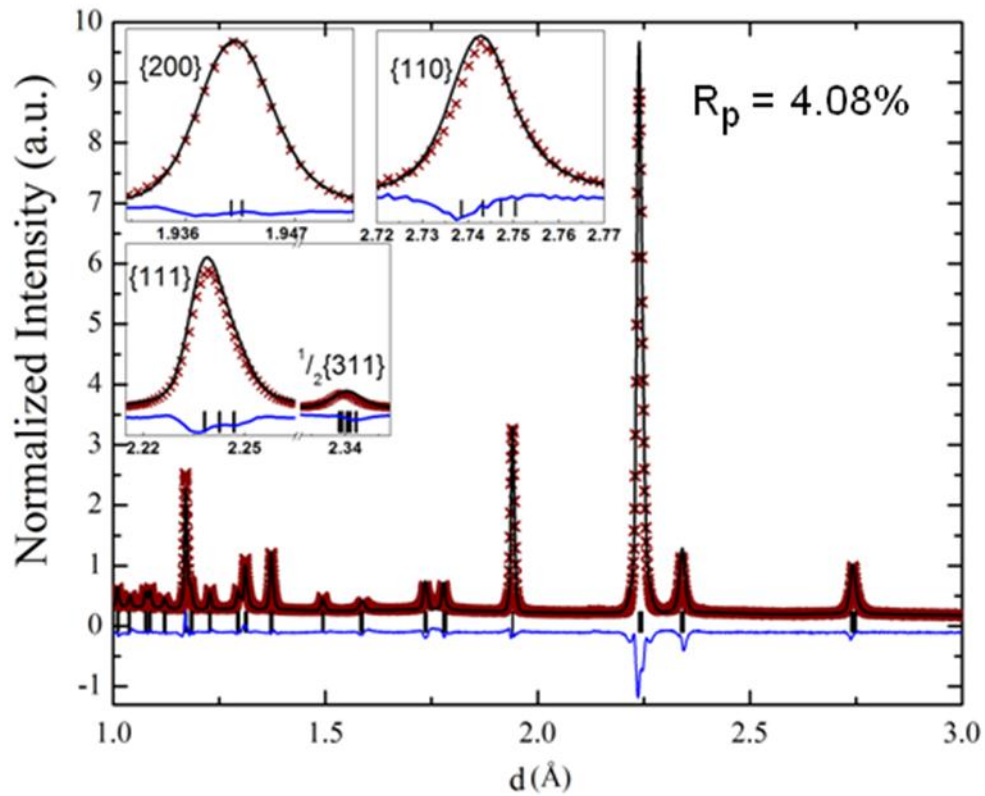


Figure 4-1. Powder neutron diffraction pattern of sintered NBT powders (x) along with the results of the calculated fit (-). Reflection markers for the C_c phase are shown as vertical lines with the difference pattern below the diffraction pattern. The labeled peak indices are relative to the pseudo-cubic perovskite unit cell. The Bragg R value (R_p) for the fit is also indicated in the figure.

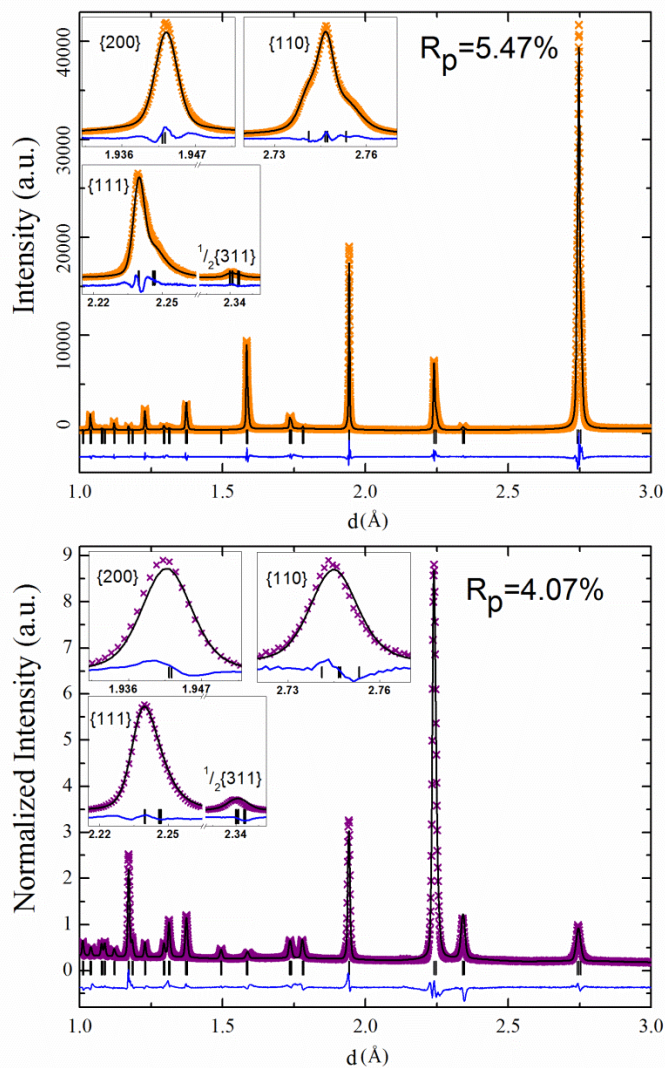


Figure 4-2. Powder diffraction patterns of sintered NBT powders from X-ray (x) and neutron (x) diffraction. The results of a calculated fit (-) using both the X-ray and neutron diffraction patterns for each type of powder are also shown. Reflection markers for the Cc phase are shown as vertical lines with the difference pattern below the diffraction pattern. The labeled peak indices are relative to the pseudo-cubic perovskite unit cell. The Bragg R values (R_p) for each fit are also indicated in the figure.

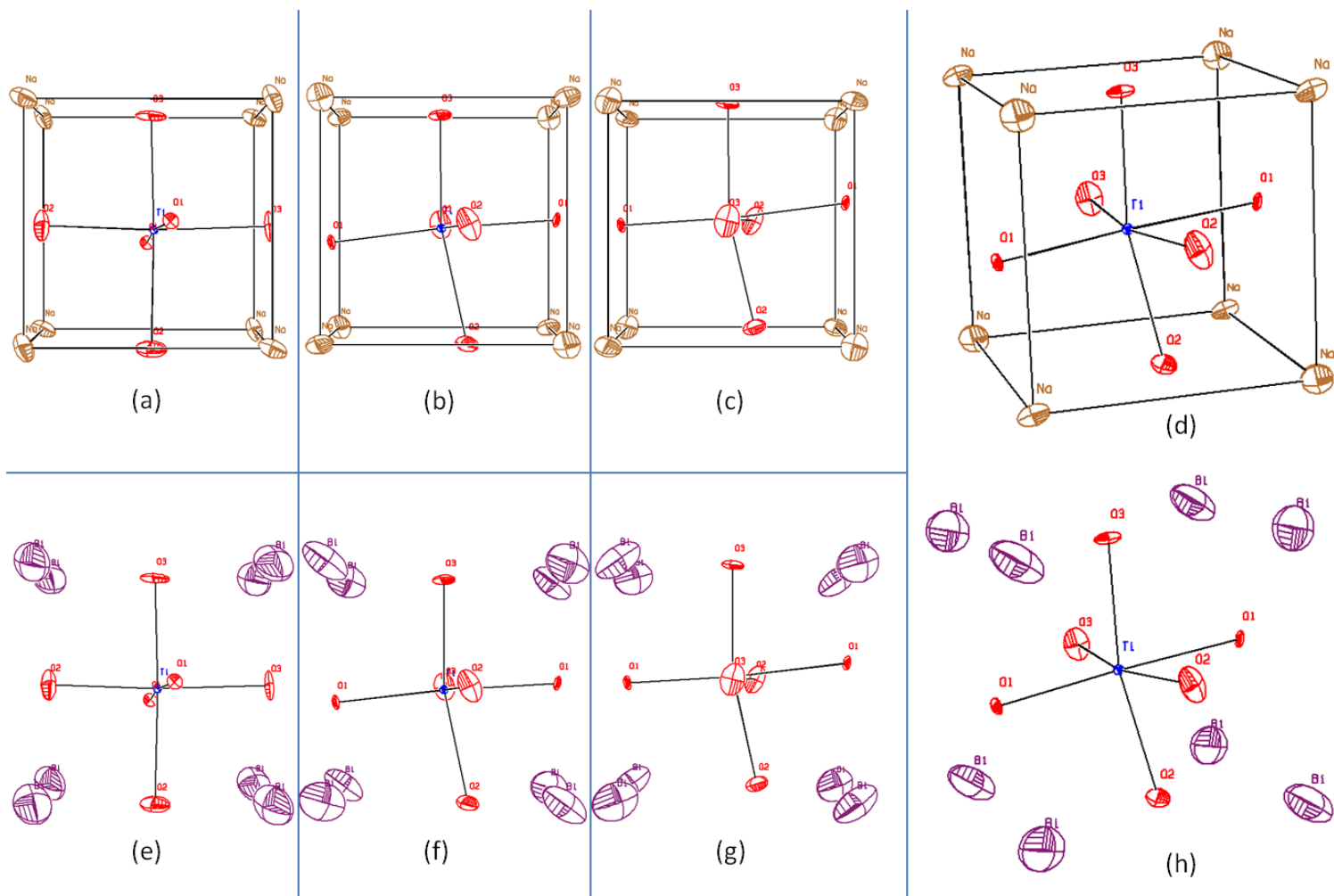


Figure 4-3. Thermal ellipsoids of NBT at room temperature obtained from a combined refinement of X-ray and neutron diffraction data. Na and Bi are shown as unique sites for clarity; they are modeled as sharing the A-site in a random arrangement. Parts A-C show projections of the pseudo-cubic unit cell along the $\langle 001 \rangle$ direction, and part D shows the pseudo-cubic unit cell with only Na on the A-site. Parts E-G show projections of the pseudo-cubic unit cell along the $\langle 001 \rangle$ direction, and part H shows the pseudo-cubic unit cell with only Bi on the A-site.

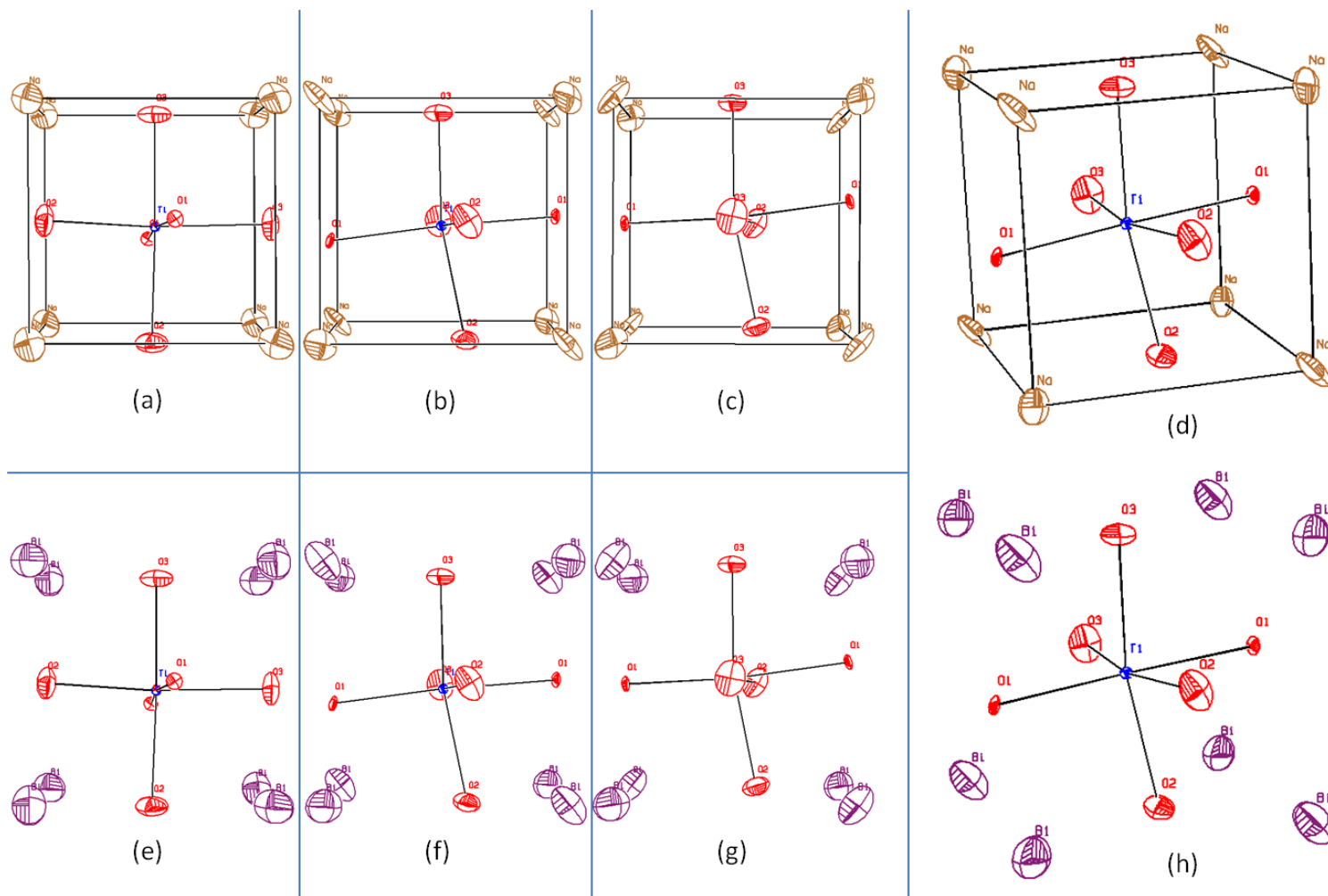


Figure 4-4. Thermal ellipsoids of NBT at room temperature obtained from a refinement of the neutron diffraction data. Na and Bi are shown as unique sites for clarity; they are modeled as sharing the A-site in a random arrangement. Parts A-C show projections of the pseudo-cubic unit cell along the $\langle 001 \rangle$ direction, and part D shows the pseudo-cubic unit cell with only Na on the A-site. Parts E-G show projections of the pseudo-cubic unit cell along the $\langle 100 \rangle$ direction, and part H shows the pseudo-cubic unit cell with only Bi on the A-site.

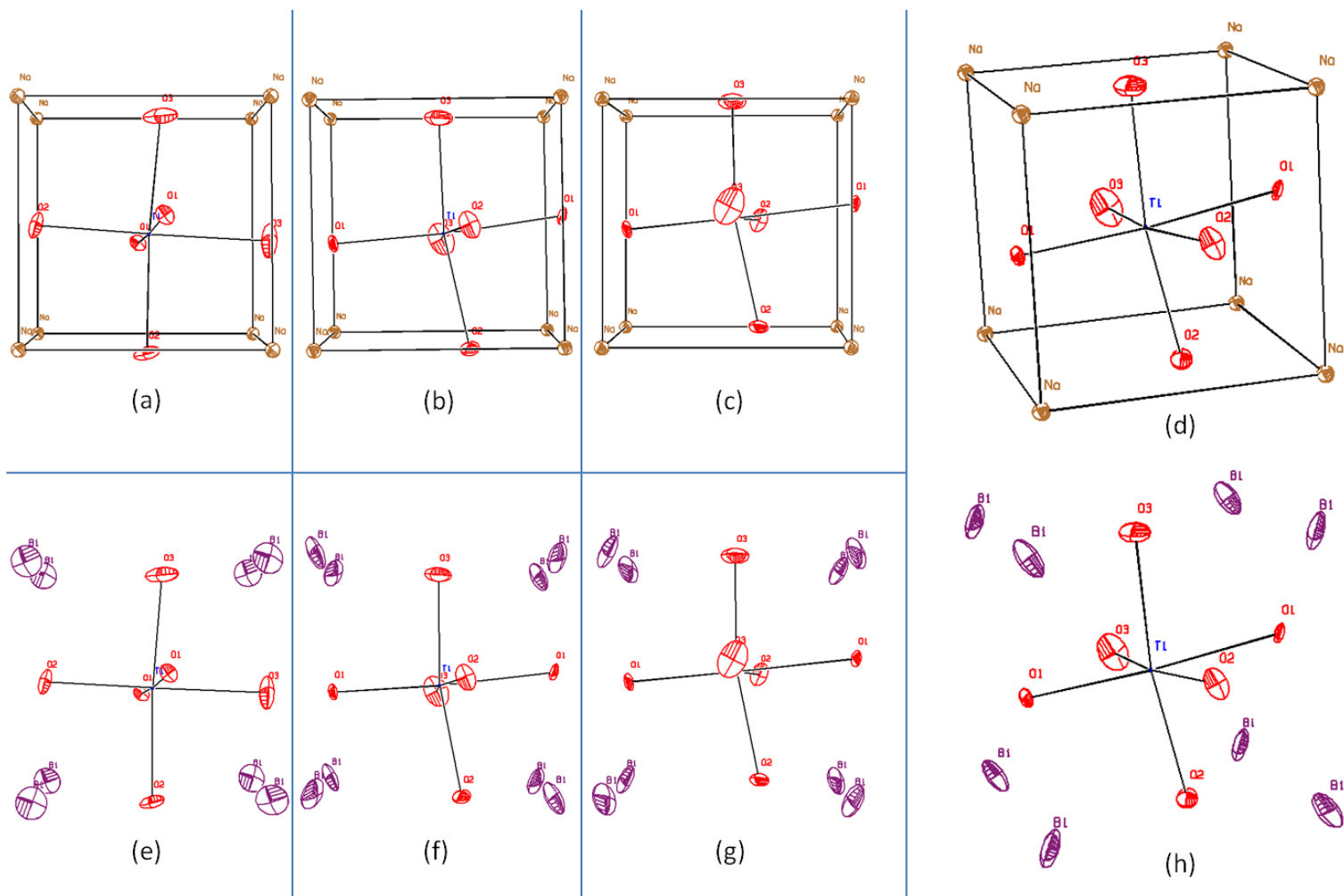


Figure 4-5. Thermal ellipsoids of NBT at 15 K obtained from a refinement of the neutron diffraction data. Na and Bi are shown as unique sites for clarity; they are modeled as sharing the A-site in a random arrangement. Parts A-C show projections of the pseudo-cubic unit cell along the $\langle 001 \rangle$ direction, and part D shows the pseudo-cubic unit cell with only Na on the A-site. Parts E-G show projections of the pseudo-cubic unit cell along the $\langle 001 \rangle$ direction, and part H shows the pseudo-cubic unit cell with only Bi on the A-site.

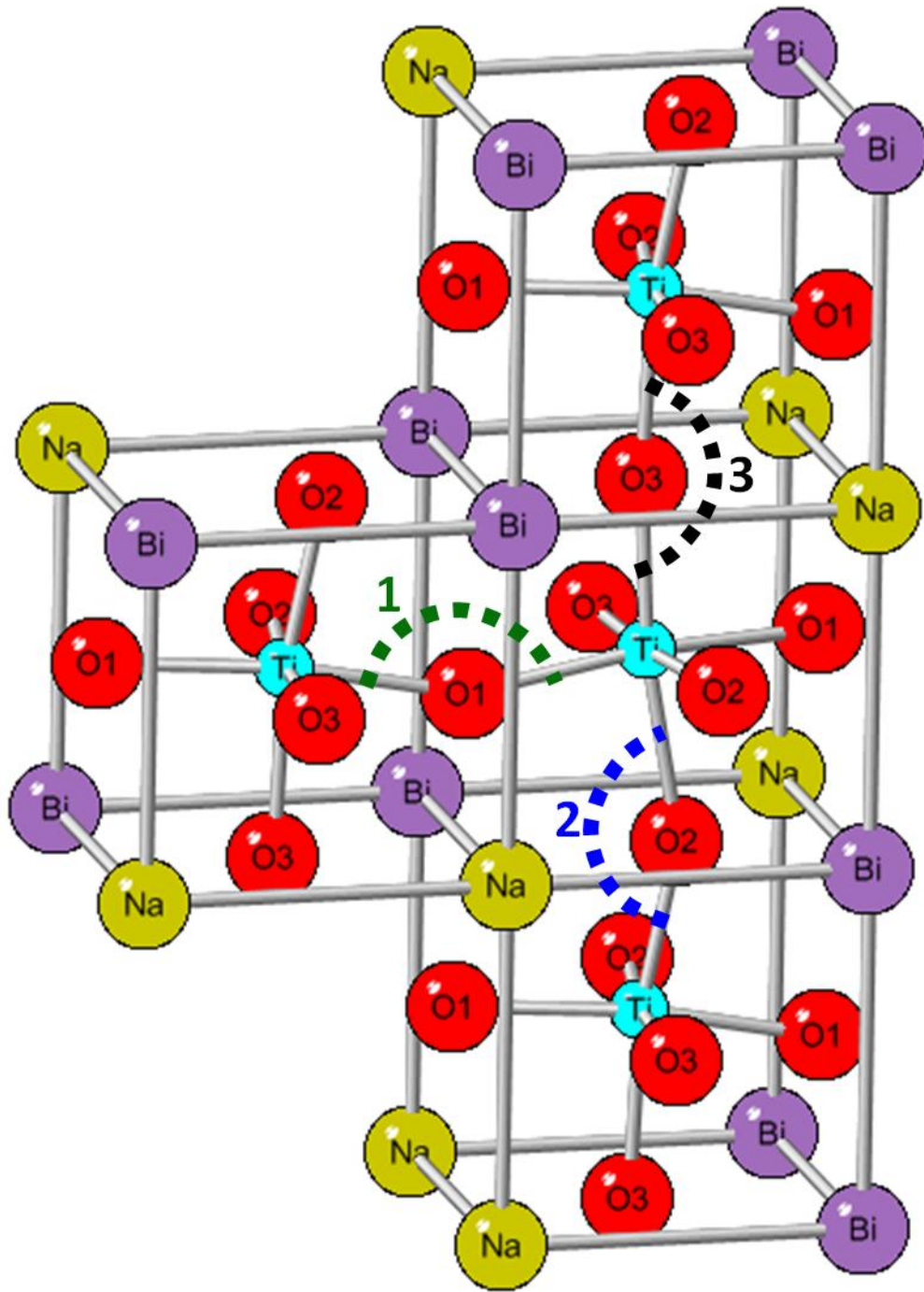


Figure 4-6. Schematic of the oxygen octahedral tilting calculation. The angle is determined using the non-distorted Ti position (0.5 0.5 0.5 in the pseudo-cubic unit cell), and each of the three unique oxygens. The three unique α angles are marked with the numbers 1, 2, and 3 in the figure.

CHAPTER 5 LOCAL ATOMIC STRUCTURE DEVIATION FROM AVERAGE STRUCTURE OF NBT

Motivation

Chapters 3 and 4 investigated the average structure of NBT, however, this appears to be even more complex with reports of a unique short range structure in this material. A study of NBT using transmission electron microscopy (TEM) found the presence of nano-scale platelets of tetragonal ($P4bm$) structure within the NBT matrix ($R3c$ or Cc) at room temperature.²⁵ This finding was also supported by studies of NBT single crystals through diffraction contrast images in TEM.²⁷ In addition, first-principles calculations based on density functional theory (DFT) were utilized to examine potential A-site with the conclusion that short range chemical ordering is expected.²⁹

As mentioned in Chapter 4, a complete crystal structure description of NBT must include a description of the mixed A-site occupancy of Bi^{3+} and Na^+ . Because the X-ray scattering factors of Bi^{3+} and Na^+ are significantly different (i.e., 62.425 Bi^{3+} and 6.881 Na^+)⁸¹, X-ray scattering can be used to distinguish between atoms on this site. However, X-rays are not sensitive to O^{2-} (i.e. a scattering factor of 4.089 for O^{2-})⁸¹, and neutrons are more often used to characterize oxygen positions and occupancies in materials because O^{2-} has a neutron scattering factor comparable to the other ions (i.e. 5.80 for O^{2-} and 8.53 for Bi^{3+})⁸².

Total scattering methods are now well-recognized tools capable of extracting reliable and meaningful information on the short range order of complex materials.^{87, 88} A brief description of the process for obtaining a PDF measurement is given in Appendix A. To probe local structural distortions⁸⁹ and ordering,⁹⁰ pair distribution function (PDF) studies have been utilized in a variety of perovskites, including different

ferroelectric materials.⁹¹⁻⁹⁴ Recently, Jeong *et al.* compared the short range structure of NBT to that of its solid solution with $\text{Bi}_{0.5}\text{K}_{0.5}\text{TiO}_3$ through neutron total scattering studies with Reverse Monte Carlo modeling.³⁰ They report that, on a 0-4 Å length scale, the bonding environment of Bi with O is different from that of Na with O, due to a large displacement of Bi from its average position.³⁰

The large difference in the scattering factors of Na^+ and Bi^{3+} in response to X-rays makes this technique a more sensitive method to probe potential A-site ordering, while neutrons are more sensitive to the lighter ions, like O^{2-} . Thus, a combined analysis using both X-ray and neutron scattering can be used to examine both potential A-site ordering and the oxygen positions around this site, making such an approach ideal. This method provides a sensitive probe to examine the differences between the local structure of NBT and its newly determined long-range structure.⁵⁹

Experimental

Materials used for this analysis were the same materials described in Chapter 3. The diffraction measurements used for the analysis in this chapter are the synchrotron XRD measurements described in Chapter 3 and the neutron diffraction measurements described in Chapter 4. Extraction steps were followed in order to obtain the experimental pair distribution function from scattering data utilizing the program PDFgetN⁹⁵ and a $Q_{\text{max}} = 35 \text{ \AA}^{-1}$.

X-ray PDF measurements were completed at room temperature at the 11-ID-B beam line at the Advanced Photon Source (APS) at Argonne National Laboratory using a General Electric amorphous Si two-dimensional (2D) detector. The sample to detector distance was fixed at 117.13 mm, and synchrotron XRD with the wavelength of 0.2127 Å and a beam size of 0.2 mm x 0.2 mm were utilized. Each measurement was carried

out in multiple exposures and then, 2D data sets were integrated using the program FIT2D.⁹⁶ The program PDFGETX2⁹⁷ was used with standard corrections to extract the experimental PDF using a $Q_{\max}=22 \text{ \AA}^{-1}$.

The model of the average structure presented here builds on the model of the combined refinement given in Chapter 4. The same combined refinement approach was utilized here to model both the calcined and sintered data. Least-squares refinements to the experimental PDF data were carried out with the aid of PDFgui software.⁹⁸

Calibration of the NPDF and 11-ID-B instrument, using standard samples, provided parameters describing the PDF dampening envelope due to instrument resolution and the PDF peak broadening due to intensity noise⁹⁹ and these were fixed during analysis. Reverse Monte Carlo (RMC) simulations were performed using RMCprofile¹⁰⁰ with 5 x 10 x 10 supercells starting from the Rietveld-refined Cc structure, with 10,000 total atoms in each supercell. These simulations were fit to $D(r)$ using the convention of Keen¹⁰¹ and run for 16 h on single 2 GHz cores (about 2.4×10^7 moves). Simulations were constrained by periodic boundary conditions and hard-sphere nearest neighbor cutoffs, but not by lattice symmetry. No bunching occurred at the hard-sphere distances. RMC fits were performed for neutron data only, since it offered superior resolution (higher usable limit of momentum transfer Q) and similar cross-sections for each atom. Parameters for bond valance sum calculations followed those used by Brese and O'Keefe.¹⁰²

Results and Discussion

Rietveld Analysis

Diffraction patterns measured for both calcined and sintered NBT are shown in Figure 5-1. As described in Chapter 3, calcined powders contribute more to peak

broadening in the diffraction patterns than sintered samples of NBT. Therefore, the insets of the X-ray measurements in Figure 5-1 show a more pronounced peak splitting in the sintered powders. Due to this lack of peak splitting, the calcined pattern can be fit to a lower weighted residual, R_w , value (equivalent to the R_{wp} value described in Equation A-3). The long-range average structure of each of the calcined and sintered materials was determined using a combined Rietveld refinement of the X-ray and neutron diffraction patterns. A closer examination of the diffraction patterns on a logarithmic scale (not pictured) shows a large modulation in the background due to diffuse scattering in the material, indicating that NBT may have a local structure which differs from the average structure.

The observed Bragg intensities were used to create Fourier maps of the NBT Cc unit cell using both neutron and XRD data (Figure 5-2). These agree well with the previously-published Cc space group that describes the average crystallographic structure on a long length scale.⁵⁹ The Fourier maps display scattering density in the unit cell, and symmetry of these maps is determined by the space group. All atoms in the NBT Cc cell lie on $4a$ Wyckoff positions with site symmetry 1 (no symmetry constraints), so any off-centering or static displacements should be evident in large, anisotropic, or irregular isosurfaces of scattering density on each site. Instead, only spherical scattering density is observed at each site. Large Bi displacements would be especially evident in the X-ray Fourier map due to its large cross section. The small spherical isosurfaces here may be interpreted as suggesting that simply adding A-site displacements alone is insufficient describe any disorder in the Cc model (which already contains a very asymmetric Bi coordination in the average structure).

Small Box PDF Modeling

The pair distribution functions measured for calcined and sintered NBT using both X-ray and neutron total scatter are shown in Figure 5-3 on a 1-20 Å range. The X-ray and neutron results have very different peak intensities due to the different scattering factors of the two methods. A brief comparison of the results from the calcined and sintered samples shows no obvious differences between these two measurements. The experimental X-ray and neutron PDFs were initially fit using PDFgui with the average *Cc* structure model obtained from prior Rietveld analyses. For the refinement in PDFgui of the neutron PDF data the lattice parameters, atomic positions, and atomic displacement parameters were refined within the setting of the *Cc* space group (Figure 5-3C and D). Similar parameters were used for the X-ray PDF data refinement (Figure 5-3A and B), except that the atomic positions of O²⁻ ions were fixed to those from the neutron refinement and isotropic O²⁻ atomic displacement parameter were constrained to be equivalent among the three unique O²⁻ sites.

The results of this initial fitting, displayed in Figure 5-3, prompt several immediate observations. First, in all cases the model structure describes the higher-*r* region of the PDF more closely than the lower-*r* region of the PDF, suggesting a departure of the local atomic structure from the long-range average structure. This is also supported by the presence of diffuse scattering in the diffraction patterns of the material. Second, the X-ray PDF data (top panels) are more poorly described by the average structure model than the neutron PDF data (bottom panels). This suggests Bi³⁺ ions (much more heavily weighted in the X-ray data than in the neutron data) have a prominent role in the local atomic disorder. Finally, a comparison of the R_w values and the difference curves for the model fits of both X-ray and neutron $G(r)$ functions indicates that the calcined sample

data are not as well described by the average structure model as the sintered sample data. This suggests a greater departure from the long-range structure in the material calcined at 800°C prior to the sintering step at 1100°C. The R_w value calculated in PDFgui is similar to the R -weighted pattern (R_{wp}) value calculated in GSAS (Equation A-3).

Inspection of the atomic displacement parameters from the Rietveld and PDF refinement, presented in Table 5-1, allows a comparison between the atomic displacement parameters calculated in the PDF fit and those calculated using the Rietveld method. A large decrease in the Na/Bi atomic displacement parameter is observed in the PDF refinement. This implies that the refined oxygen atomic positions create a more stable environment for the A-site in the PDF model. Final refined values indicate that the calcined powder has slightly closer values to the average structure, compared to the sintered powder (Table 5-1).

Several different local structure models were employed to understand the departure of the local atomic structure from the long range average structure, as well as the differences between calcined and sintered states of the material. First, the influence of A-site ordering was explored because there is evidence of short range A-site ordering reported from DFT calculations.²⁹ The results of one such model using the sintered structure are given in Figure 5-4. In order to create a model of an ordered structure, the experimental average structure of sintered NBT was first refined in PDFgui with random A-site ordering using the 1-10 Å range in the PDF (corresponding to fraction layered phase = 0 in Figure 5-4A). The A-site atoms of the refined structure were then changed into a layered arrangement with layers perpendicular to the monoclinic c -axis (as shown

in Figure 5-4A). The same region of the PDF was then modeled by varying the phase fractions of the ordered and disordered phases while maintaining all other parameters constant.

In Figure 5-4A, the trend in R_w of the fit with varying phase fractions of the ordered and disordered phases is shown. For both calcined and sintered samples, the agreement factor between observed and calculated X-ray data is increasingly disparate as the fraction of layered phase is increased during modeling. There is little change observed between the agreement factors for the neutron data. Figures 5-4B and C demonstrate that neutron PDF is not as sensitive to this type of atomic ordering relative to X-ray PDF. A closer look at the 6-7 Å region of the calculated X-ray PDFs shows that the random model allows for a larger split in the peak with a larger intensity at the higher r side. A comparison of this feature with the measured PDF shown in Figure 5-3 indicates that this feature of the random model is consistent with the measurement. Although a number of other superstructures were trialed with chemical short range ordering of the A site cations, but none were found to better describe the data than the model with fractionally occupied (shared) sites. Since A-site ordering was not beneficial in improving the PDF fit of NBT, it is not considered to be the source of the deviation of the local structure.

Since A-site ordering is not the source of the local structure deviation, another approach, the so-called ' r -range refinement' or 'box-car fitting' was utilized. It is an emerging strategy that is used to extract quantitative information about the *length scale* of local atomic order from the Pair Distribution Function analysis of complex materials. In order to extract information concerning the local cation bonding environments in NBT,

the neutron PDF was first modeled using only the 1-11 Å range. The neutron PDF is then described by refining the structural model over separate and successive 10 Å intervals in real space. The PDF of the first 1-6 Å was also refined separately for comparison. In this range, the step size is small compared to the lattice parameter (>5 Å). Thus, they were kept constant at their initial values obtained from the refinement in the 1-11 Å range, while the atomic positions and displacement parameters were refined. In all of the successive steps, the lattice parameters, atomic positions, and atomic displacement parameters were refined at each step and then evaluated as a function of length-scale in the material.

Figure 5-5 presents box plots of the bond lengths extracted from the 'box-car fitting' of the neutron PDF data over increasing intervals in real space. The averages (shown in the insets) and standard deviations (indicated by the edges of the boxes) are calculated from the six unique Ti-O bond lengths and the 12 unique (Bi/Na)-O bond lengths. Since the bond lengths with oxygen are of interest and the Na/Bi position is constrained, the neutron PDF was used for this analysis rather than the XRD PDF due to the previously mentioned higher sensitivity to the oxygen positions. The error bars shown for the average bond lengths in the insets of the figure are propagated from the error calculated for each bond length in the refinement. The spread in the bond distances is also highlighted by the whiskers of the boxes, which represent the minimum and maximum value at each r interval.

It is clear from the insets of Figure 5-5 that the average bond lengths of (Bi/Na)-O are longer in the first 10 Å range than at higher r . A similar, but less pronounced trend is also observed in the Ti-O bond lengths. In addition, at lower r values, the spread in the

(Bi/Na)-O bond lengths is greater compared to the higher r range. A comparison between calcined and sintered powders indicates that while the average (Bi/Na)-O bond lengths in the first 10 Å are larger, the spread in the bond lengths at high r is less for the calcined powders than sintered powders. These results for higher r in both the calcined and sintered powders are consistent with the average structure calculated using the Rietveld method. Also, it should be noted that the spread in the (Bi/Na)-O bond lengths is much greater than that in the Ti-O bond lengths. This is contrary to the expected result since Bi^{3+} is a much heavier atom than Ti^{4+} .

The bond lengths calculated from the average structure and the 'box-car fitting' of the neutron PDF were used to determine the bond valence sum (BVS) of Bi^{3+} , Na^+ , and Ti^{4+} .⁹⁷ The results of this calculation as a function of r are given in Figure 5-6. The figure indicates that in the average structure Bi^{3+} has a BVS of 2.26 in calcined and 2.33 in sintered NBT, which is significantly lower than the ideal 3. On the other hand, Ti^{4+} has a BVS of 4.05 in calcined and 4.01 in sintered NBT rather than the ideal 4. The change in the bond length of (Bi/Na)-O on the local scale seen in Figure 5-5 may therefore be due to A-site or O^{2-} atomic motion, allowing for a higher BVS for Bi^{3+} .

It is important to note that, since this is a small box approach, the Bi^{3+} and Na^+ positions are constrained to be identical in the model. This is a significant limitation because accommodation of the Bi^{3+} lone pair often results in distorted Bi-O coordination, and thus local dipoles, but no such disorder is expected for Na^+ . While this type of cation-specific structural information cannot be determined using a small box approach, it can be examined using Reverse Monte Carlo analysis, as discussed in the next section.

Reverse Monte Carlo Modeling

In order to observe the distinct atomic arrangements that give rise to the low- r disorder observed in this system and accommodate the different bonding environments of Bi and Na, Reverse Monte Carlo refinement of the neutron PDF was employed. Fits to calcined and sintered samples are shown in Figure 5-7. These fits reproduce the experimental data more closely than the least-squares refinements in Figure 5-3 because the large-box RMC model is not constrained by Cc symmetry, enabling many more degrees of freedom. No significant differences are observed between calcined and sintered samples. In both cases, bond valence sums indicate average positive valences of 1.39, 3.09, and 3.99 for Na, Bi, and Ti, respectively. Since the Na valence is far from its expected value, new simulations were run with BVS constraints applied such that each cation is fixed to its nominal valence over the entire course of the RMC simulation. The fits to data shown in Figure 5-7 were performed with BVS constraints applied, and no difference in the quality of fit is seen versus BVS-unconstrained simulations. Therefore, results in the subsequent figures are given for simulations where the valences of all cations are constrained to be within ± 0.05 of the nominal values of Na^+ , Bi^{3+} , and Ti^{4+} .

Folding the large RMC model into a single unit cell produced “point clouds” of approximately a thousand atoms at each crystallographic site. These are plotted as a function of real space for a sintered sample in Figure 5-8. Only Na atoms are shown on the A-sites in Figure 5-8A, and only Bi are shown in Figure 5-8B. As there is no obvious difference in cation distribution between Na and Bi, it is possible that the differences in Na/Bi coordination are not a simple matter of Bi^{3+} off-centering. This is corroborated by the Fourier map of Bragg scattering in Figure 5-2, which shows a spherical neutron and

X-ray cross-section on the A-sites, implying that Bi^{3+} does not prefer a simple displacement along a certain crystallographic direction. Displacement of nearby O^{2-} anions in response to the central cation may play a role in satisfying Na^+ and Bi^{3+} valence. This result is contrary to the previous finding of Jeong *et al.* that Bi^{3+} has a large degree of directional off-centering, possibly because an $R3c$ space group was used as the starting model while this work has a Cc starting model.³⁰ The large displacement seen by Jeong *et al.* with respect to a the higher-symmetry $R3c$ cell³⁰ are contained within the average structure of the Cc model. This difference between the two models provides further support for the classification of NBT as a monoclinic Cc system. Consequently, the asymmetric Bi^{3+} environment is obtained without incoherent Bi^{3+} displacements which had been reported for other Bi^{3+} containing materials such as the pyrochlore $\text{Bi}_2\text{Ti}_2\text{O}_7$.¹⁰³

Since the RMC model contains thousands of distinct Na and Bi cations, each with a unique coordination, the *partial* pair distribution functions $n(r)$ that show only Na-O or Bi-O distances found in the simulated model can be selectively plotted. These distributions are shown in Figure 5-9. Each distribution is divided into three curves, showing the bond distances of Na and Bi to the three distinct O anions in the 4a Wyckoff positions in the Cc cell. Between the panels of Figure 5-9, vertical ticks show the A-O bonds present in the Cc cell (they apply to both Na^+ and Bi^{3+} in the average structure) as determined from Rietveld refinement of the combined diffraction data. The partial pair distributions are broader than the A-O distances from the average structure, in part due to instrumental broadening, while Na-O bonds are nearly symmetric about their average distance. On the other hand, Bi-O bonds are more asymmetric than the

Cc model suggests. It appears that the Cc structure is a compromise, lying between the disparate cation environments of Na^+ and Bi^{3+} . This result, in combination with the small box BVS calculation, implies in order for both Na^+ and Bi^{3+} to satisfy the sum charge of their bonds with O^{2-} , they each form a unique bonding environment with the surrounding oxygen atoms.

Comparison of the partial pair distributions of the bond distances of Bi^{3+} with each of the three unique O^{2-} positions (Figure 5.9B) shows that while the Bi-O1 and Bi-O2 bond lengths have a fairly even bimodal distribution, the Bi-O3 bond lengths have only a slight bimodal feature. Figure 5.10 compares the configuration of the three unique O^{2-} positions around the A-site. It is apparent in Figure 5.10 that the O1 and O2 positions are offset from the edges formed by the Ti^{4+} ions, creating a long and short bond with Bi^{3+} along each direction. In contrast, the O3 position is directly on the edge and in a more stable environment. Therefore, it would require more energy for the O3 ion to move than for the other two O ions. This may explain the smaller splitting in the local Bi-O3 bond distance distribution.

Summary

The short range structure of sodium bismuth titanate was investigated through X-ray and neutron pair distribution studies. A small box model approach was first used to rule out the presence of local A-site ordering in NBT. Examination of the PDF through a 'box-car fitting' method showed that bond environments change as a function of length scale in the material. This method revealed that the BVS of Bi^{3+} in the average structure is significantly lower than the ideal value and could be the driving force for the departure of the local structure from the average. Since the small box model constrains Bi^{3+} and Na^+ to the same position, changes in the O^{2-} positions will affect both ions, and

therefore the positions of the O^{2-} around Bi^{3+} sites on a local scale cannot be determined using this model. The RMC method permits the positions of Na^+ and Bi^{3+} to be unique, allowing the determination of their unique bonding environments with O^{2-} . This is clearly indicated in Figure 5-8 by the asymmetry of the Bi-O partial pair distribution function. The unique local bonding environment of Bi^{3+} with O^{2-} may be formed for Bi^{3+} to achieve a BVS closer to its oxidation state as well as for the accommodation of the Bi^{3+} lone pair.

Table 5-1. Refined isotropic displacement parameters (\AA^2) for calcined and sintered NBT from a combined X-ray and neutron refinement via the Rietveld method, and PDF fit results for the X-ray and neutron data.

Calcined NBT				Sintered NBT			
Element	Rietveld (\AA^2)	Neutron PDF (\AA^2)	X-ray PDF (\AA^2)	Element	Rietveld (\AA^2)	Neutron PDF (\AA^2)	X-ray PDF (\AA^2)
Na/Bi	0.0390(1)	0.022(1)	0.01941(2)	Na/Bi	0.0386(1)	0.0193(5)	0.011767(6)
Ti	0.0031(2)	0.0067(7)	0.00615(2)	Ti	0.0005(2)	0.0075(4)	0.01799(3)
O1	0.0108(2)	0.0097(7)		O1	0.0039(3)	0.0082(4)	
O2	0.0171(2)	0.0145(9)	0.0685(1)	O2	0.0133(5)	0.0084(5)	0.03774(5)
O3	0.0204(2)	0.0206(9)		O3	0.0188(4)	0.0188(7)	

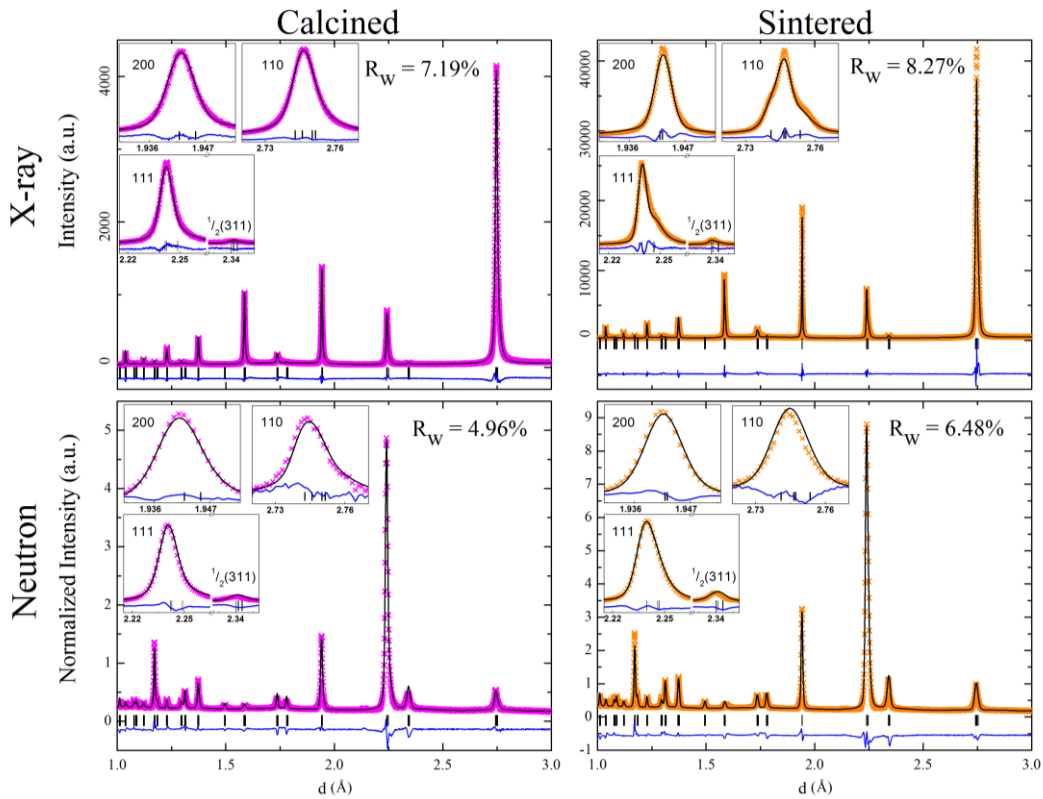


Figure 5-1. Powder diffraction patterns of sintered (x) and calcined (x) NBT powders using neutron and X-ray diffraction data. The results of a calculated fit (-) using both the X-ray and neutron diffraction patterns for each type of powder is also shown. Reflection markers for the Cc phase are shown as vertical lines with the difference pattern below the diffraction pattern. The labeled peak indices are relative to the pseudo-cubic perovskite unit cell. The Bragg R values (R_w) for each fit are also indicated.

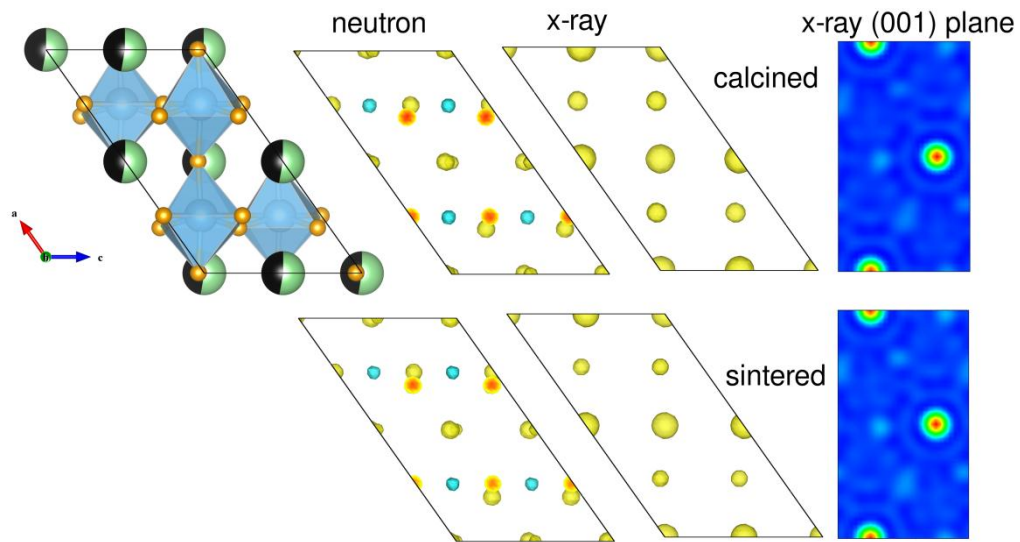


Figure 5-2. The NBT unit cell is shown on the left. The four figures in the middle are Fourier maps represented as 3D isosurfaces showing the total scattering density in the NBT unit cell for neutron and X-ray Bragg profiles. The light blue surfaces in the neutron maps indicate the negative scattering density of Ti. X-ray scattering densities on the A-sites are shown on the far right along the monoclinic (001) plane, with only spherical intensity present.

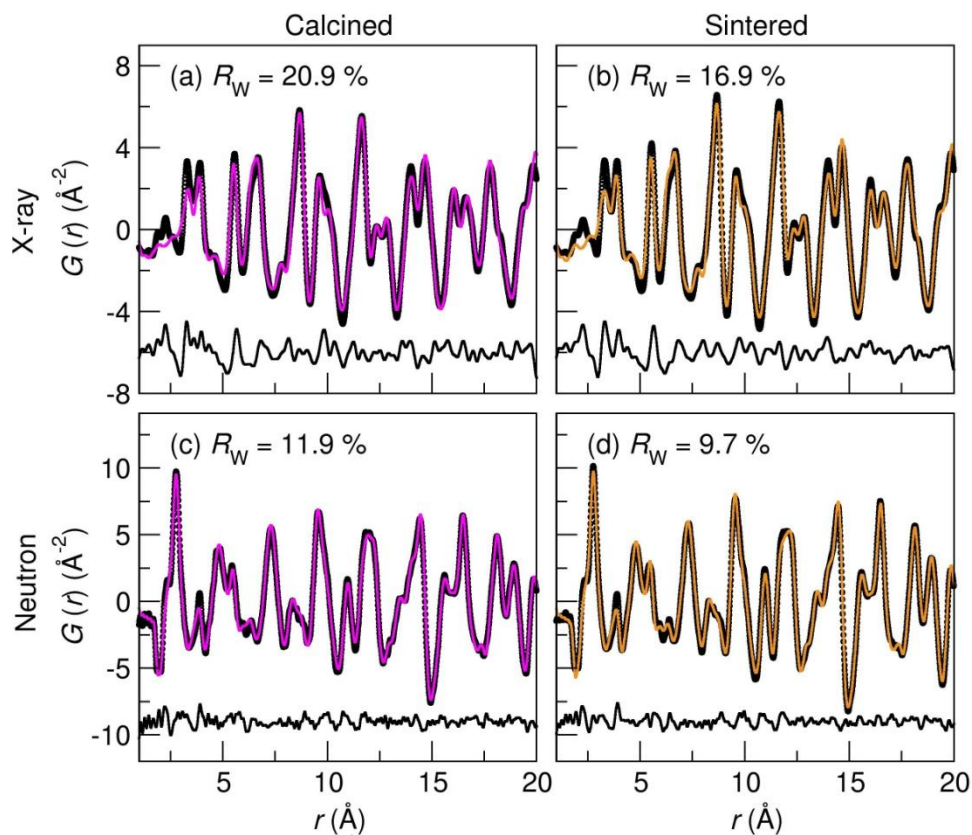


Figure 5-3. Results of fitting 1-20 Å X-ray $G(r)$ s (A, B) and neutron $G(r)$ s (C, D) with the Cc average structure model for calcined and sintered NBT samples. Data are shown as black circles, fits are given as purple and orange lines (for calcined and sintered samples, respectively) and difference curves have been offset below the data and fits in black. Refined goodness of fit parameters (R_w) are shown in each panel. Note X-ray and neutron data are on different intensity scales.

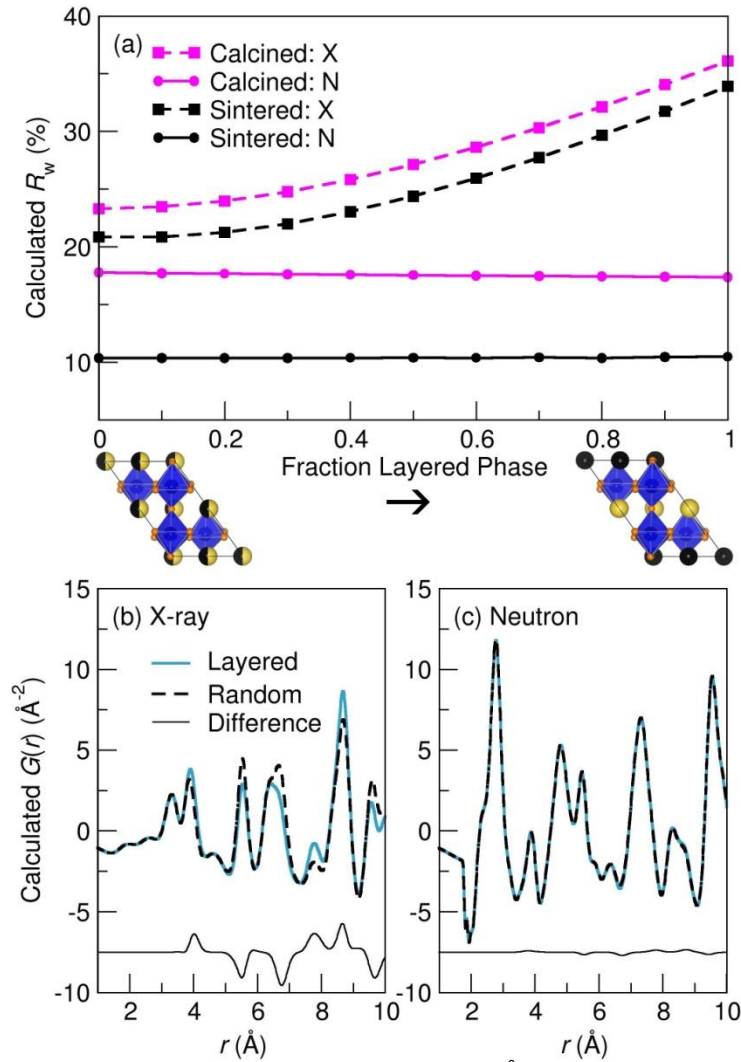


Figure 5-4. An examination of A-site ordering: A) 10 \AA PDF refinement R_w values (goodness of fit) for sintered (black) and calcined (purple) data sets with different fractions of mixed-site A cation and layered A cation structure models. Neutron results are circles and solid lines through the points, while X-ray results are squares and dashed lines through the points. In the lower two panels, 10 \AA X-ray B) and neutron C) PDF calculations are displayed for the two end-member model structures (at fraction of layered phase = 0 and 1). The random structure calculations are shown in black dashed lines and the layered structure calculations are displayed in blue solid lines.

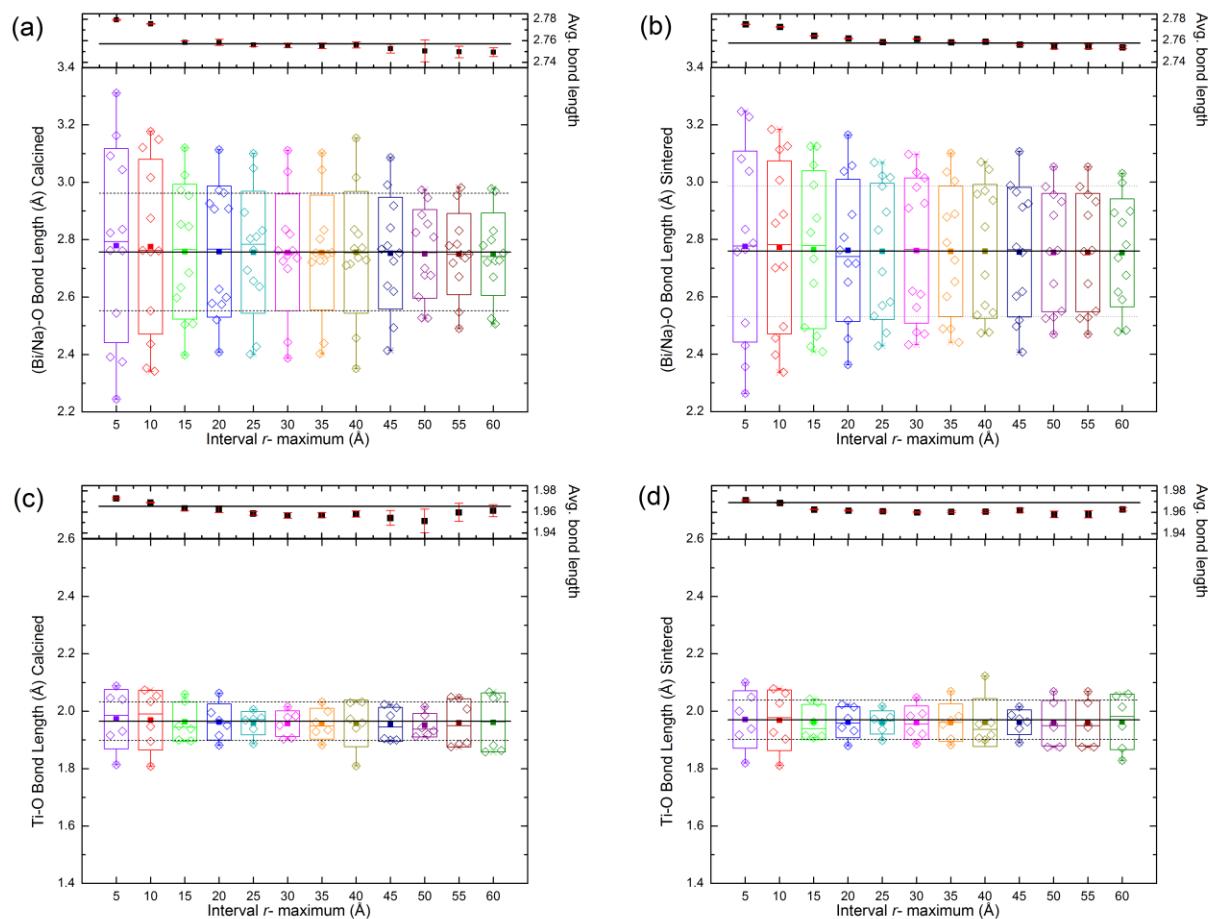


Figure 5-5. Calculated bond lengths from the 'box-car fitting' method for both calcined and sintered NBT. A) – B) (Bi/Na)-O, and C) – D) Ti-O bond lengths. The box plots at each r value indicate the spread in the bond lengths for that calculation. The edges of the box represent one standard deviation from the mean and the whiskers are the minimum and maximum values. The closed symbols for each data set are the mean values while the open symbols show all of the bond lengths. The solid line in each plot is the average bond length calculated from the atomic positions refined through the Rietveld method and the dashed lines show one standard deviation from the mean. The inset in each plot shows the average bond lengths from the 'box-car fitting' on a smaller y-scale for clarity (all insets have the same y-range).

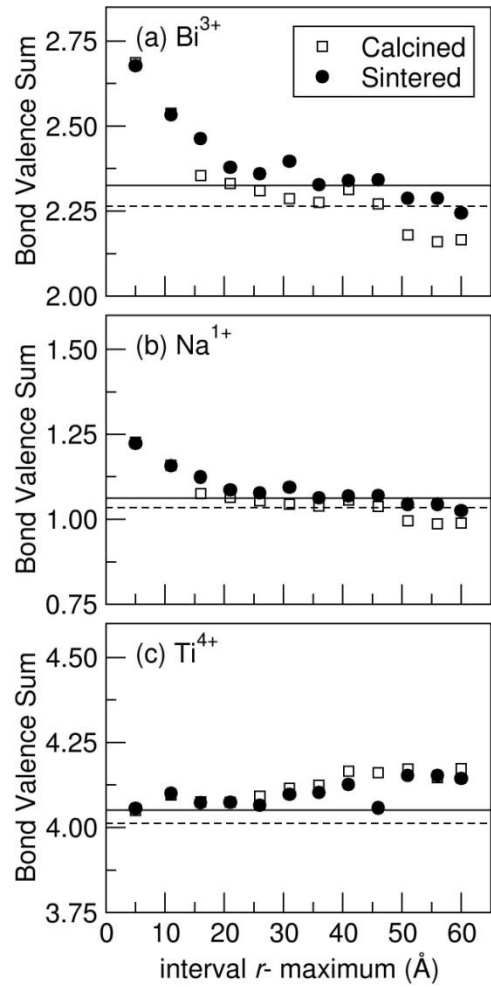


Figure 5-6. The calculated bond valence sums for elements in calcined and sintered NBT. A) Bi^{3+} , B) Na^{+} , and C) Ti^{4+} . The dashed and solid lines represent the BVS calculated from the average structure obtained using the Rietveld method for calcined and sintered NBT, respectively.

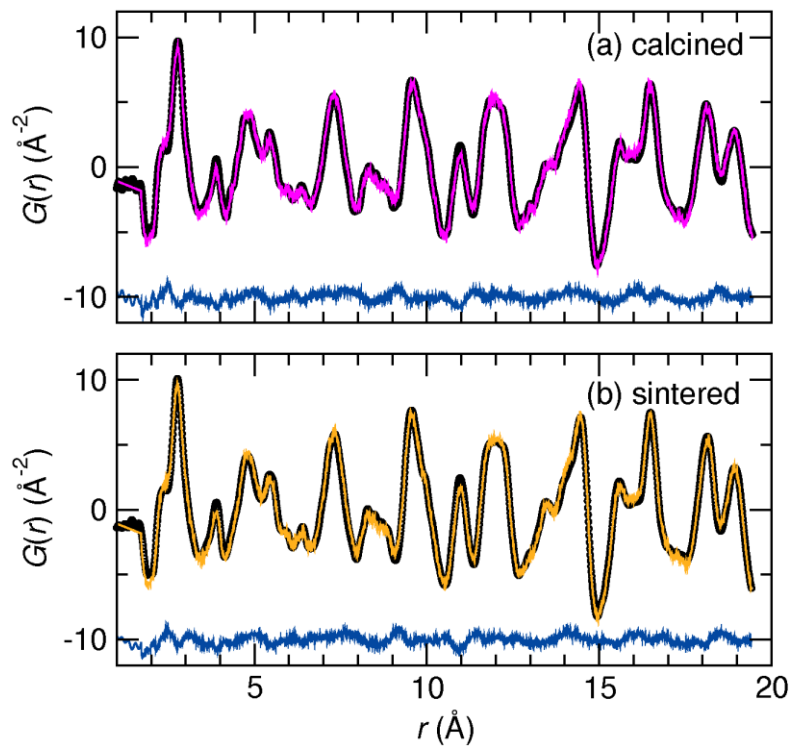


Figure 5-7. Reverse Monte Carlo fits to the neutron PDF of A) calcined and B) sintered NBT. Both simulations were conducted with BVS constraints to maintain the nominal cation valences.

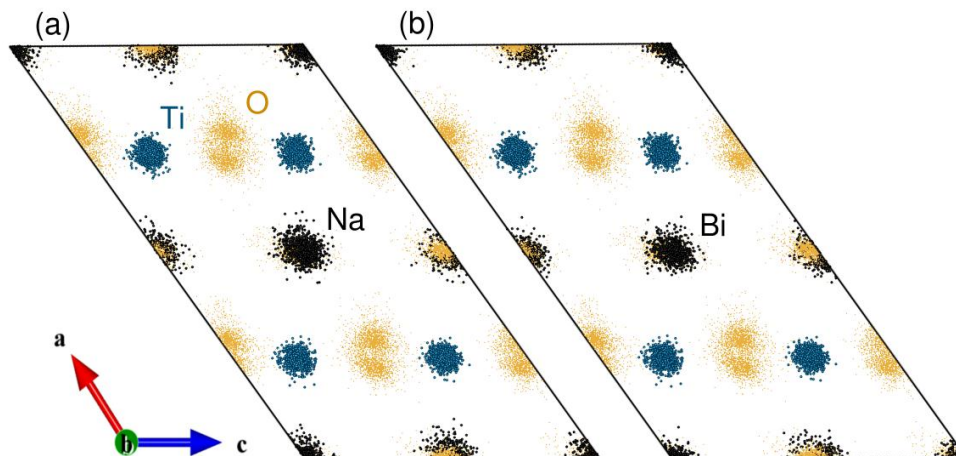


Figure 5-8. Schematic diagram showing folded RMC models, which produce “point clouds” of atoms at each crystallographic site. No significant differences are observed when a single model is plotted to show only A) Na^+ and B) and Bi^{3+} cations, implying that Bi^{3+} does not simply displace off-center, and does not have significantly larger displacement than Na^+ .

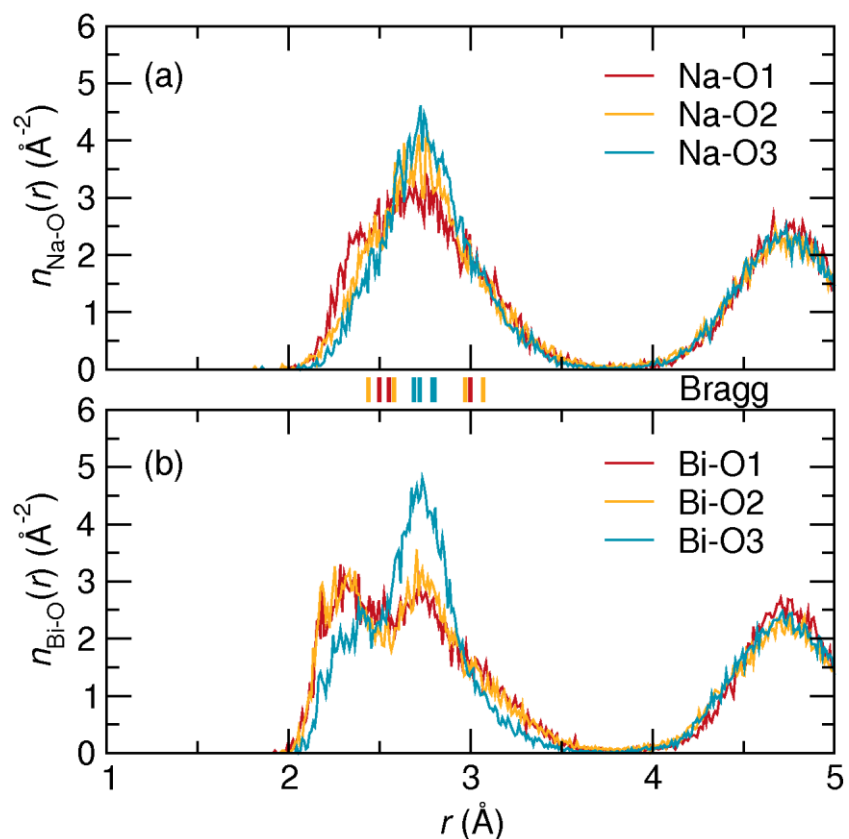


Figure 5-9. Partial pair distribution functions from the RMC model of a sintered sample. A) Almost symmetric bond distance distributions of Na-O (a). Tick marks between the two panes show the Rietveld-refined bond distances in the Cc cell. B) For Bi-O, the asymmetry observed in the Cc cell is greatly amplified. Distances are shown to each of the three distinct O atomic positions on 4a sites in the Cc cell.

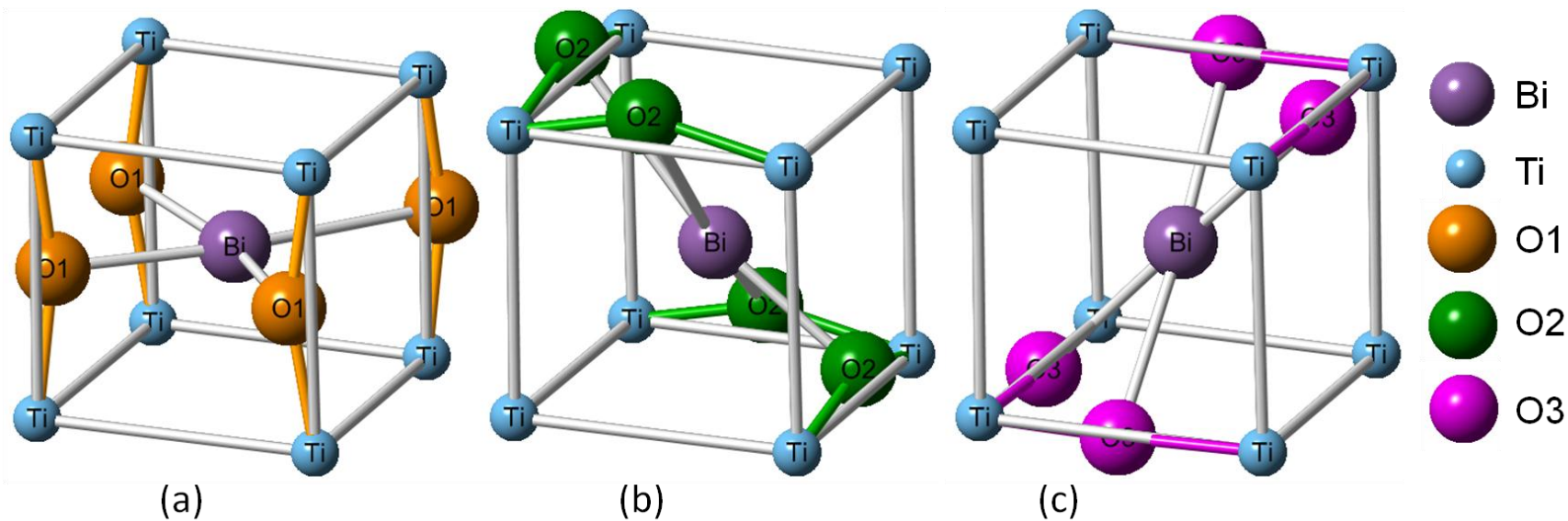


Figure 5-10. Pseudo-cubic representation of the NBT unit cell showcasing the arrangement of the three unique oxygen lattice positions relative to the Bi-site. A) O1, B) O2, and C) O3 positions.

CHAPTER 6 PHASE TRANSITION SEQUENCE OF NBT USING HIGH-RESOLUTION X-RAY DIFFRACTION

Motivation

The structure of NBT, both at room temperature and at elevated temperatures has been the subject of much debate in literature. The content of this chapter is reprinted with permission from E. Aksel, J. S. Forrester, B. Kowalski, P. A. Thomas, and J. L. Jones, "Phase transition sequence in sodium bismuth titanate observed using high-resolution X-ray diffraction," Applied Physics Letters, Vol. 99, no. 222901, copyright (2011) American Institute of Physics.¹⁰⁴ Early structural investigations of NBT report a rhombohedral lattice.²⁰⁻²² Vakhrushev reported superstructure reflections indicating tilting of a single axis (corresponding to what is now known as the $P4bm$ phase²³) above $\sim 300^\circ\text{C}$ and tilting of all three axes (corresponding to what is now often referred to as the room temperature $R3c$ structure) at lower temperatures.²¹ Between approximately 250°C and 300°C , the existence of both tilting systems suggested a mixed phase region.²¹ In 1995, Suchanicz and Kwapulinski observed a rhombohedral phase up to 250°C , mixed rhombohedral and tetragonal to $\sim 400^\circ\text{C}$, and tetragonal to $\sim 525^\circ\text{C}$.²² Jones and Thomas confirmed a single phase rhombohedral $R3c$ structure with the $a^-a^-a^-$ tilt system up to 255°C , a region of phase coexistence ranging from at least $307 - 327^\circ\text{C}$, and a tetragonal structure with the $a^0a^0c^+$ tilting system to $\sim 500^\circ\text{C}$.²⁴ However, these early structural analyses indicate no phase transition between room temperature and 250°C , though piezoelectric thermal depoling occurs at temperatures of $\sim 190^\circ\text{C}$ (e.g., Ref. ³¹). Above this temperature, the ferroelectric polarization hysteresis loop

Reprinted with permission from E. Aksel, J. S. Forrester, B. Kowalski, J. L. Jones, and P. A. Thomas, Applied Physics Letters **99**, 222901 (2011), copyright American Institute of Physics (2011).

becomes pinched¹⁰⁵, a feature often associated with an antiferroelectric structure. Thus, an antiferroelectric phase was widely reported in early literature as existing between 200°C and 250°C.¹⁰⁶

Using transmission electron microscopy, it was found that at room temperature, nano-scale tetragonal ($P4bm$) platelets exist within a rhombohedral ($R3c$) matrix, and the $P4bm$ superlattice reflections increase in intensity with heating until the material transitions to a tetragonal phase.^{25, 26} By utilizing visibility criteria to determine the symmetry of these platelet-like inclusions at room temperature, it was established that they are regions with octahedral tilting $a^0a^0c^+$.²⁷ At 200°C, an intergrowth of orthorhombic ($Pnma$) platelet-shaped domains inside a $R3c$ matrix was observed, and increased in volume fraction up to 300°C.²⁶ Thus, the higher temperature intergrowth of $Pnma$ and $P4bm$ platelets correlates with the piezoelectric thermal depoling temperature.^{26, 31} The completion of the $Pnma$ intergrowth correlates with the Curie temperature of ~320°C.^{18, 26}

As described in Chapter 3, based on high resolution powder XRD studies, the room temperature structure of NBT can be best modeled using the monoclinic Cc space group. This structure, exhibiting an $a^-a^-c^-$ octahedral tilting system, is a subgroup of the $a^-a^-a^-$ tilting system in the previously assumed $R3c$ structure. The subtle monoclinic distortions of the Cc space group provide an additional dimension into understanding the temperature dependence of the phase transitions in NBT. In particular, the observation of a lower symmetry room temperature space group than $R3c$ offers an opportunity to re-investigate the piezoelectric thermal depoling behavior at ~190°C (Ref. ³¹) and the sequence of transitions from $R3c$ to the high temperature $Pm\bar{3}m$ structure.

Therefore, this chapter presents high temperature powder XRD of NBT using the same high resolution instrument as in Chapter 3.⁵⁹

Experimental

Crushed sintered ceramics of NBT were measured at beamline 11-BM at the Advanced Photon Source using the processing, instrumental parameters, wavelengths, and refinement approach described in Chapter 3.⁵⁹ Samples were heated at 5°C/min to 600°C while 1.25 min XRD patterns with a step size of 0.002° in 2θ were measured. On cooling, 50 min patterns with a 0.001° step in 2θ were measured at select temperatures due to their position in the phase diagram: 600°C, 400°C, 300°C, 250°C, 100°C, and 25°C. A cooling rate of 5°C/min was used between these temperatures.

Results and Discussion

Figure 6-1 shows selected Bragg reflections of NBT from room temperature to 600°C. At room temperature, the 111 reflection appears asymmetric, the 110 reflection is relatively broad, and the $\frac{1}{2}(311)$ superlattice reflection is relatively intense. From 195°C to 280°C, the 111 reflection asymmetry decreases, the 110 reflection narrows, and the $\frac{1}{2}(311)$ superlattice intensity decreases. These features suggest a change in the long-range structure starting at ~195°C. Above 280°C, the 200 reflection splits into two distinct peaks, the 111 peak becomes more symmetric, and the $\frac{1}{2}(311)$ peak disappears while the $\frac{1}{2}(310)$ peak appears. This is consistent with the previously reported $P4bm$ phase²³ existing between 280°C and ~510°C. Above this temperature, all peaks are indexed by the cubic $Pm\bar{3}m$ space group.

The six diffraction patterns measured for 50 min on cooling were modeled using the Rietveld refinement program GSAS.⁶² The initial structural models used the monoclinic space group Cc (for 25°C, 100°C, and 250°C), the tetragonal space group

P4bm (for 300°C and 400°C), and the cubic space group $Pm\bar{3}m$ (for 600°C). *Cc* was chosen to model the 100°C and 250°C patterns because peak splitting indicated equivalent (but more subtle) distortions as observed in the room temperature pattern, which a *R3c* model could not adequately represent.⁵⁹ Although the long-range average structure of NBT at room temperature is best modeled using the *Cc* space group, local disorder in the material can lead to small variations in the diffraction patterns which are not entirely modeled using a single *Cc* phase. The local disordered regions may include anti-phase boundaries, domain walls, local A-site ordering, microstrains, or platelets of *P4bm* or *Pnma* structure. Thus, in the refinements at 25°C, 100°C, and 250°C, a second phase with space group $Pm\bar{3}m$ was added to the model. In all cases, the criteria of fit were improved, indicating that a cubic phase can model this disorder. Such an approach has been previously used to describe other perovskite systems, such as LaMnO_3 .¹⁰⁷

Selected refinement results are given in Table 6-1, and the model at 250°C is shown in Figure 6-2. Of particular note is the increase in fraction of the cubic ($Pm\bar{3}m$) phase with increasing temperature from 2 wt. % at 25°C to 30 wt. % at 250°C. Since this phase is used to model the short-range regions in the material, the large volume fraction may be associated with the increase of nano-scale domains within the *Cc* matrix phase. The growth in volume fraction of the nano-scale platelets presented in previous literature²⁵⁻²⁷ may correlate with the cubic volume fraction increase calculated in the present work. It should be noted that the presence of a long-range *Pnma* or *P4bm* phase was not observed in the present work due to the absence of associated superlattice reflections ($\frac{1}{2}(0ee)$ or $\frac{1}{2}(oee)$, respectively). Additionally, the intensity of the

$\frac{1}{2}(311)$ reflection decreases between 195°C and 280°C, which may be associated with either a decrease in the amplitude of tilt or a decrease in the phase fraction of a tilted phase.

Summary

The present structural observations can be correlated to the piezoelectric thermal depoling behavior of NBT, which was previously observed near 190°C³¹ and measured for these materials³⁶ as starting at ~140°C and completing at ~200°C. Because these temperatures do not correlate with any discrete phase transition temperatures measured in the present work, a structural transition from *Cc* to another higher symmetry space group (e.g., *R3c*) is not the origin of piezoelectric thermal depoling in this structure. Rather, thermal depoling is correlated with an increase in a material volume fraction which is only present at a short range (modeled here as a cubic phase). This material fraction cannot be ascribed to the long-range *Cc* space group and may be associated with the growth of *Pnma* or *P4bm* platelets. Therefore, one possible origin of the thermal depoling behavior is the loss of long-range ferroelectric order by a decreasing the volume fraction of the major *Cc* phase or the associated percolation of disordered material.

Table 6-1. Refined phase proportions, lattice parameters, cell volume, and criteria of fit parameters for all Rietveld refinements.

Temp (°C)	Space group	Phase Frac.	a (Å)	b (Å)	c (Å)	β (°)	Cell Vol. (Å ³)	Cell Vol.* (Å ³)	Criteria of Fit
25	<i>Cc</i>	98%	9.5268(2)	5.48234(3)	5.50854(3)	125.3607(6)	234.631(5)	58.658	$R_p = 4.97\%$
	<i>Pm</i> $\bar{3}$ <i>m</i>	2%	3.88497(2)	3.88497(2)	3.88497(2)	90	58.6357(5)	58.636	$R_{wp} = 6.87\%$ $\text{Chi}^2 = 3.513$
100	<i>Cc</i>	91%	9.5212(2)	5.48621(5)	5.51295(6)	125.285(1)	235.066(6)	58.767	$R_p = 4.67\%$
	<i>Pm</i> $\bar{3}$ <i>m</i>	9%	3.88750(3)	3.88750(3)	3.88750(3)	90	58.7503(8)	58.750	$R_{wp} = 6.18\%$ $\text{Chi}^2 = 2.080$
250	<i>Cc</i>	70%	9.53996(7)	5.50072(3)	5.51361(3)	125.2970(6)	236.147(3)	59.037	$R_p = 3.95\%$
	<i>Pm</i> $\bar{3}$ <i>m</i>	30%	3.893460(3)	3.893460(3)	3.893460(3)	90	59.02108(8)	59.021	$R_{wp} = 5.01\%$ $\text{Chi}^2 = 1.364$
300	<i>P4bm</i>	-	5.507792(9)	5.507792(9)	3.899572(8)	90	118.2965(4)	59.148	$R_p = 4.06\%$ $R_{wp} = 5.11\%$ $\text{Chi}^2 = 1.428$
400	<i>P4bm</i>	-	5.515262(9)	5.515262(9)	3.905851(8)	90	118.8086(4)	59.404	$R_p = 3.91\%$ $R_{wp} = 4.90\%$ $\text{Chi}^2 = 1.310$
600	<i>Pm</i> $\bar{3}$ <i>m</i>	-	3.912135(5)	3.912135(5)	3.912135(5)	90	59.8744(1)	59.874	$R_p = 4.24\%$ $R_{wp} = 5.70\%$ $\text{Chi}^2 = 1.778$

* Cell volume calculated for all space groups was transformed into a single pseudo-cubic unit cell.

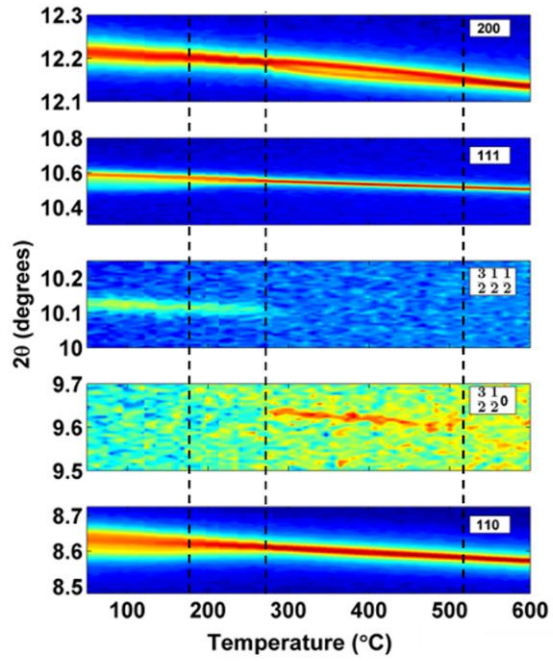


Figure 6-1. The evolution of selected Bragg reflections of NBT from room temperature to 600°C.

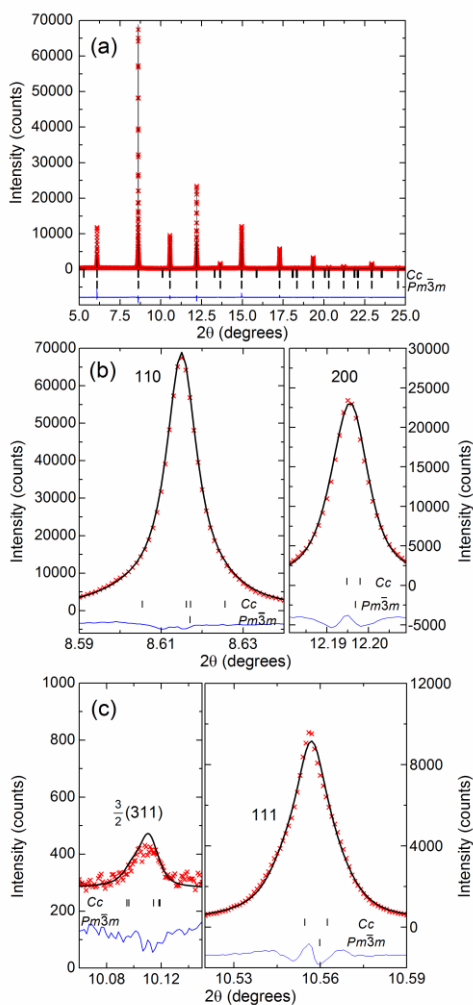


Figure 6-2. Rietveld refinement of the XRD pattern measured at 250°C. A) The whole pattern showing the observed pattern (x) and the calculated model (—), hkl markers for the *Cc* and *Pm* $\bar{3}$ *m* phases, and the difference pattern. B) Detail of the 110 and 200 peaks, and C) the $\frac{1}{2}$ (311) and 111 peaks.

CHAPTER 7 STRUCTURE AND PROPERTIES OF LA-MODIFIED NBT AT AMBIENT AND ELEVATED TEMPERATURES

Motivation

In Chapter 6, the changes in NBT structure with temperature were investigated in order to understand the underlying mechanism of thermal depolarization. Properties, such as T_d , of ferroelectric materials are often modified with the use of chemical substitution.¹⁶ One common type of aliovalent modification in PZT is with the use of donor dopants, which lead to a “softening” of the material.³² This type of doping often leads to higher permittivity and piezoelectric coupling but little change in the Curie temperature.³² A commonly used donor dopant in the ferroelectric ceramic PZT is La^{3+} , which substitutes for the Pb^{2+} on the A-site.³² The addition of 2 at% La leads to an increase in the d_{33} from 200 to 250 pC/N and only a slight decrease in the T_c from 390 to 381°C.¹⁰⁸ Also, in the case of another PZT-based composition, the addition of 1 at% La caused a doubling in the measured d_{33} value, from 305 to 640 pC/N and a large increase in the free dielectric constant from 1138 to 1800.¹⁰⁹ In a different study, modification of PZT with concentrations of ≥ 1 at% La led to a decrease in the T_c as well as a reduced c/a ratio.¹¹⁰

Recent literature studies have also examined the effects of La modification in NBT. Watanabe *et al.* reported that with the addition of 1at% La to NBT, the d_{33} increased from 70 to 82 pC/N, and free permittivity increased from about 350 to 450.³³ Additionally, it increased the T_m slightly from 340 to 348°C, but decreased the T_d from 180 to 150°C.³³ Herabut and Safari found that the addition of 1.72 at% La increased the d_{33} from 58 to 91 pC/N and the relative permittivity from 240 to 550.¹¹ They also found that La substitution caused the structure of NBT to approach cubic.¹¹ These changes in

NBT properties with La modification, while not as pronounced as in PZT, show that La affects both the properties and structure of this material. This chapter examines more closely the changes in the structure and properties of NBT with varying amounts of La. In addition, phase transitions with temperature are also examined.

Experimental

Ceramic samples were prepared using solid state synthesis as described in Chapter 3 with the addition of La_2O_3 to obtain concentrations of 0, 0.5, 1.0, 1.5, and 2.0 at% La. The addition of La_2O_3 to the samples was compensated for by a stoichiometric reduction in Na_2CO_3 and Bi_2O_3 (the two reactants were reduced in equal amounts). Prior to electrical measurements, electrodes were applied to the major faces of the samples via gold sputtering. Polarization and displacement were measured at room temperature in response to an applied bipolar electric field of triangular waveform with an amplitude of 9 kV/mm and frequency of 1 Hz. The ceramics were initially unpoled and were cycled several times until a fully saturated response was achieved. Polarization was measured using a 15 μF capacitor in a Sawyer–Tower circuit and displacement was measured using an optical sensor.

For electrical property measurements, gold electrodes were sputter deposited onto the major faces of all samples followed by electrical poling at 4 kV/mm for 5 min in a silicone oil bath held at 80°C. The electric field was removed from the samples while they were held in the 80°C oil bath. The samples were set aside for approximately 24 h, after which the direct longitudinal piezoelectric coefficient was measured using a Berlincourt d_{33} meter (APC Ceramics, Mackeyville, PA). Samples were heated from 25°C to 550°C using a heating rate of 2°C/min while permittivity and loss were

measured at five frequencies: 100 Hz, 1 kHz, 10 kHz, 100 kHz, and 1 MHz, using a precision LCR meter (Hewlett Packard).

For poled samples all compositions, the converse piezoelectric coefficient was measured *in situ* during heating. In these *in situ* thermal depoling measurements, the displacement of the sample was measured using a laser Doppler vibrometer (Polytec, Waldbronn, Germany) while a sinusoidal voltage of amplitude 10 V was applied to the sample.³⁶ The sample was simultaneously heated with a heating rate of 2°C/min and each reported d_{33} value was the average of 25 readings from the laser. Separate *ex situ* thermal depoling measurements were completed in which the samples were annealed at a set temperature for 10 min in a furnace (Thermofisher model F47925, Dubuqu, IA), after which they were removed and the d_{33} was measured using a Berlincourt d_{33} meter when the sample reached room temperature.³⁶ Each reported reading was an average of five readings at different positions on the face of the pellet. The furnace set temperature was measured using both the internal furnace thermocouple and an external thermocouple placed ~1 mm above the sample surface. The set temperature was progressively increased by ~10°C increments until the samples exhibited a near-zero d_{33} value.

High-resolution XRD patterns of crushed ceramics were measured at room temperature, as described in Chapter 3, and at elevated temperatures, as described in Chapter 6. Crystal structure refinements of the powders at room and elevated temperatures were carried out using the Rietveld analysis program General Structure Analysis System.⁶² To account for the asymmetry of the peaks, profile function 4 (with Stephens asymmetry incorporated¹¹¹) yielded the closest fit to the diffraction data. The

peaks generally became more symmetrical during heating, which allowed the use of a combination of profile functions 3 and 4.

Results

Electrical Property Measurements

Polarization and strain hysteresis of the various compositions under applied electric fields at room temperature are shown in Figure 7-1. It is apparent that the substitution of La in NBT leads to only small changes in the polarization and strain measurements. The substitution of 0.5 and 1.0 at% La results in a slight decrease in the E_c (by ~ 0.5 kV/mm) and an increase in the P_r (by ~ 5 $\mu\text{C}/\text{cm}^2$). The most significant change is observed in the 1.5 at% La composition, with a decrease in the E_c field by 1 kV/mm and in the P_r by 5 $\mu\text{C}/\text{cm}^2$. The case of 2.0 at% La is different from the other compositions, showing a slight increase in E_c and no change in P_r . It appears that the slight “softening” of NBT, characterized by a decrease in E_c , ceases with the addition of 2 at% La. An examination of the strain hysteresis indicates no significant changes in the peak-to-peak strain as a function of La modification.

Prior to the temperature dependent piezoelectric coefficient and permittivity measurements, all samples were poled at the same poling conditions of 5 min at 80°C using an electric field of 4 kV/mm. The 2 at% La-modified sample did not have a measurable d_{33} after poling, and was therefore not used in the following temperature dependent measurements. Measurements of the longitudinal piezoelectric coefficient, d_{33} , as a function of temperature are shown in Figure 7-2. The experiment was conducted *in situ*, where the converse d_{33} was recorded, and *ex situ*, where the direct d_{33} was recorded. The *in situ* measurements show a general decrease in the T_d of NBT with increased La substitution. Also, a small increase in the room temperature d_{33} is found

with the addition of 0.5 and 1.5 at% La. The temperature range in which depolarization occurs increases with increasing La content until at 1.5 at% La, where the range is comparable to the unmodified sample. The *ex situ* measurements show different trends in the depolarization of these materials. It appears that the addition of 0.5 and 1.0 at% La does not change the depolarization temperature of NBT, but a sharp decrease in T_d is found for the 1.5 at% La-modified sample. A summary of both the T_d from *in situ* and *ex situ* depolarization measurements is given in Table 7-1.

Permittivity and loss tangent were also measured as a function of temperature for poled and unpoled samples of the same compositions. Figure 7-3 shows the permittivity and loss tangent measured at five frequencies for unmodified and 0.5-1.5 at% La modified NBT. The T_d is generally associated with a peak in the loss tangent vs. temperature plot and an inflection point in the permittivity vs. temperature plot. This point can be seen in the poled measurements, but is indistinct in the unpoled measurement. The T_d from the permittivity vs. temperature plots shows a decrease with an increase in La content, consistent with the *in situ* converse d_{33} measurements. A summary of these temperatures is provided with the depolarization results in Table 7-1. The La-modified samples show a frequency dispersion in the permittivity around the T_d . Additional results of property measurements conducted on La-modified NBT can be found in Appendix D.

Crystallographic Structure of La-Modified NBT

Selected X-ray diffraction reflections from high resolution XRD measurements of unmodified and La-modified NBT are shown in Figure 7-4. The reflections are indexed relative to the pseudo-cubic unit cell. An initial examination of the diffraction pattern shows a decrease in the asymmetry and width of the diffraction peaks with increasing

La content. This trend holds up to the 2 at% La composition, and at this composition, a strong asymmetry reappears in the peaks. To better understand the structural changes taking place, the structure was refined via the Rietveld method. All of the compositions were modeled using a mixture of the monoclinic Cc and cubic $Pm\bar{3}m$ space groups (based on the results shown in Chapter 6). A sample refinement result for the 1 at% La modified sample is given in Figure 7-5. Hkl markers of each of the two phases calculated account for all observed peaks and it is apparent that this phase mixture provides a close fit to the data. The refined lattice parameters and phase fractions are summarized in Table 7-2. Detailed results including the refined atomic positions and isotropic displacement parameters are given in Appendix B Table B-1.

Several observations can be made from the refinement results. The addition of La to NBT leads to an increase in the fraction of the $Pm\bar{3}m$ phase until the 2% La composition is reached. A close examination of the 2 at% La diffraction pattern revealed the presence of several small peaks that could not be indexed with the Cc or $Pm\bar{3}m$ phase. This extra phase was identified as rutile (TiO_2) and was calculated to contribute approximately 0.5 wt% to the mixture. With an increasing La concentration there is a slight decrease in the unit cell volume, however there is an abrupt increase in volume at the 2.0 at% composition. It may be interpreted that the structure is no longer stable at this point and La does not substitute in NBT to the level that might be expected. Another trend in the refinement results is the change in the lattice parameters of the Cc phase with La substitution. As the concentration of La is increased to 1.5 at%, the a and c lattice parameters and the monoclinic β angle decrease while the b lattice parameter

increases. This change in the lattice parameters indicates that the *Cc* phase is becoming less distorted and closer to the prototypical cubic structure.

To understand the structural changes of La modified NBT with temperature, XRD patterns of the 1 at% La composition were measured at temperatures of 25, 100, 250, 300, 400, and 600°C (shown in Figure 7-6). A narrowing of all the peaks is observed up to 250°C. At 300°C the disappearance of the $\frac{1}{2}(311)$ and appearance of the $\frac{1}{2}(310)$ superlattice reflections along with splitting of the (200) peak can be seen. In the 600°C pattern no superlattice reflections are present and all diffraction peaks appear symmetric. Based on these observations, the diffraction patterns were modeled using the following space groups: a combination of *Cc* and $Pm\bar{3}m$ at 25, 100, and 250°C, *P4bm* at 300 and 400°C, and $Pm\bar{3}m$ at 600°C. A summary of the refined lattice parameters from the diffraction patterns at these temperatures is given in Table 7-3. Detailed refinement results are provided in Appendix B in Table B-2. The refinement results indicate that with increasing temperature, to 250°C, the monoclinic β angle of the *Cc* phase decreases. Also, within this temperature range, the fraction of the $Pm\bar{3}m$ phase increases. The tetragonal and cubic phases used to model the higher temperature structures provide a good fit to the data at those temperatures. A comparison of the pseudo-cubic unit cell volumes as a function of temperature is consistent with the trend expected from thermal expansion. These results provide valuable support for the results reported for unmodified (Chapter 6) and Fe-modified (Chapter 8) NBT.

The continuous progression of selected diffraction peaks of unmodified and 1 at% La-modified NBT with temperature is shown in Figure 7-7. It is clear from the figure that

the peak widths in the diffraction patterns of the 1at% La-modified sample (Figure 7-7B) are significantly narrower than those of the unmodified sample pattern (Figure 7-7A). Due to this decreased peak width, it is difficult to use a single peak fitting procedure (as is used for the case of Fe-modified NBT in Chapter 8) to investigate transitions in the peaks with temperature. However, qualitative observations can be made from the figure. It appears that the $\frac{1}{2}(311)$ superlattice reflection disappears at a lower temperature after La modification.

Discussion

Measurements of polarization and strain of La-modified NBT ceramics indicate that the addition of La has a small effect on the electromechanical properties of this material. Measurements of *in situ* depolarization and temperature dependent relative permittivity show more significant effects of La modification. The depolarization temperatures measured using these two methods show similar results (*cf.* Table 7-1). Interestingly, *ex situ* measurements of depolarization do not show significant changes until 1.5 at% La is added to the material. This composition also showed the greatest change in the polarization measurements.

Several factors could contribute to the discrepancy between the *in situ* and *ex situ* depolarization measurements. One key difference to note is the unique thermal profile of each experiment. In the case of the *in situ* measurements, the samples are continuously heated at 2°C/min, while in the *ex situ* measurements the samples are held for 10 min at discrete temperatures and returned to room temperature following each step. Therefore, it is possible that the activation energy required for the depolarization process to commence is higher in the 0.5 and 1.0 at% La compositions than in the 1.5 at% composition. Due to this, the 0.5 and 1.0 at% La containing

compositions may require a longer holding time at elevated temperatures to measure the T_d more accurately.

The property changes observed with La modification are correlated to the structural changes determined from the refinement of high resolution XRD patterns. The Cc structure approaching the prototypical cubic unit cell may be the underlying reason for the decreased E_c with increasing La content. A less distorted structure would have less macroscopic strains¹¹² from domains oriented in different directions and would require less energy to switch.¹¹³ Also, the reduced monoclinic distortion of the Cc phase with La modification implies that there is a decrease in oxygen octahedral tilting. This structural change could also influence the increased E_c of the 2.0 at% La modified sample, where the monoclinic distortion increased above that of the unmodified sample. Herabut and Safari demonstrated that a higher sintering temperature was required after the addition of La to NBT,¹¹ but in this work all compositions were sintered at the same temperature. Due to the procedure used in this work, it is possible that the compositions with higher La concentration have a small fraction of unreacted material in them.

Another important observation that can be made from the structural refinements of La-modified compositions is the change in the fraction of the $Pm\bar{3}m$ phase. There is a large increase in the fraction of this phase in the 0.5 and 1.0 at% La compositions, and another slight increase in the 1.5 at% La composition. This correlates with the trend of decreasing T_d with higher La substitution measured by *in situ* depolarization and temperature dependent permittivity. The XRD patterns of the 1 at% La modified sample also shows the changes in the fraction of the $Pm\bar{3}m$ phase with increasing temperature calculated through Rietveld refinements of the XRD patterns. The fraction of this phase,

which represents local regions in the material that differ from the long range structure, increases significantly with increasing temperature. This finding further supports the conclusions of Chapters 6 and 8. The depolarization of NBT based materials is accompanied by an increase in the phase fraction of short-range regions of a material that does obey the long-range Cc space group.

Summary

The properties and crystal structure of unmodified and La-modified NBT were examined as a function of La content and temperature. It was determined that the addition of La to this material is only associated with a small change in the room temperature piezoelectric properties. However, the depolarization temperature decreased consistently as La modification increased, with a 60°C decrease from unmodified to 1.5 at% La modified NBT. The changes in properties were then related to the structural changes in the material. The addition of La to NBT led to a decreased room temperature distortion of the Cc unit cell and an increased fraction of the $Pm\bar{3}m$ phase. The fraction of the $Pm\bar{3}m$ also increased with increasing temperature. This is in agreement with the findings of Chapters 6 and 8, that the depolarization of NBT is governed by an increase in the fraction of a phase which exists only in short-range regions and does not obey the average Cc structure. It is interesting to note that at 250°C, the fraction of the $Pm\bar{3}m$ phase is 15% in 1 at% Fe-modified NBT (Chapter 8), 30% in unmodified NBT (Chapter 6), and 38% in 1 at% La-modified NBT. The trend in increasing $Pm\bar{3}m$ phase fraction from Fe-modified to unmodified and La-modified NBT correlates with the trend in decreasing depolarization temperatures in those compositions.

Table 7-1. Depolarization temperatures, T_d (°C), measured by *in situ* converse d_{33} , *ex situ* direct d_{33} and permittivity in all investigated compositions.

Composition	T_d from direct d_{33} (<i>ex situ</i>) (°C)	T_d from converse d_{33} (<i>in situ</i>) (°C)	T_d from permittivity (°C)
Unmodified	210	169	176
0.5% La	215	149	142
1% La	199	116	120
1.5% La	148	111	110

Table 7-2. Refined phase proportions, lattice parameters, cell volume, and criteria of fit parameters for samples with increasing La content at room temperature.

at% La in NBT	Space group	Phase Frac.	a (Å)	b (Å)	c (Å)	β (°)	Cell Vol. (Å ³)	Cell Vol. (Å ³) ^b	Criteria of Fit
0	<i>Cc</i>	98%	9.5267(2)	5.48235(3)	5.50852(4)	125.3605(6)	234.631(5)	58.65775	$R_p = 4.98\%$
	<i>Pm</i> $\bar{3}$ <i>m</i>	2%	3.88497(2)			90	58.6358(6)		$R_{wp} = 6.85\%$ $\text{Chi}^2 = 3.488$
0.5	<i>Cc</i>	91%	9.5212(2)	5.48554(4)	5.50295(5)	125.3190(6)	234.514(5)	58.6285	$R_p = 4.81\%$
	<i>Pm</i> $\bar{3}$ <i>m</i>	9%	3.88485(1)			90	58.6303(3)		$R_{wp} = 6.42\%$ $\text{Chi}^2 = 1.806$
1.0	<i>Cc</i>	86%	9.5199(2)	5.48698(5)	5.50144(6)	125.3066(6)	234.515(6)	58.62875	$R_p = 4.62\%$
	<i>Pm</i> $\bar{3}$ <i>m</i>	14%	3.884907(6)			90	58.6330(2)		$R_{wp} = 6.11\%$ $\text{Chi}^2 = 2.409$
1.5	<i>Cc</i>	84%	9.5180(2)	5.48908(5)	5.49884(6)	125.2924(5)	234.489(6)	58.62225	$R_p = 4.67\%$
	<i>Pm</i> $\bar{3}$ <i>m</i>	16%	3.88483(4)			90	58.6295(1)		$R_{wp} = 6.22\%$ $\text{Chi}^2 = 2.864$
2.0 ^a	<i>Cc</i>	92%	9.5330(2)	5.48903(3)	5.51028(4)	125.3364(7)	235.215(5)	58.80375	$R_p = 5.26\%$
	<i>Pm</i> $\bar{3}$ <i>m</i>	7%	3.88839(1)			90	58.7905(3)		$R_{wp} = 7.11\%$ $\text{Chi}^2 = 3.748$

^a A small fraction (~0.5%) of rutile (TiO₂) is also present at this composition.

^b Cell volume calculated for the *Cc* space group was transformed into a single pseudo-cubic unit cell.

Table 7-3. Refined phase proportions, lattice parameters, cell volume, and criteria of fit parameters for the 1 at% La sample at selected temperatures.

Temp (°C)	Space group	Phase Frac.	a (Å)	b (Å)	c (Å)	β (°)	Cell Vol. (Å ³)	Cell Vol. (Å ³) ^a	Criteria of Fit
25	<i>Cc</i>	86%	9.5199(2)	5.48698(5)	5.50144(6)	125.3066(6)	234.515(6)	58.629	$R_p = 4.62\%$
	<i>Pm$\bar{3}m$</i>	14%	3.884907(6)						90
100	<i>Cc</i>	85%	9.5262(2)	5.49303(4)	5.50324(6)	125.299(5)	235.028(5)	58.757	$R_p = 4.53\%$
	<i>Pm$\bar{3}m$</i>	15%	3.887629(5)						90
250	<i>Cc</i>	62%	9.54152(7)	5.50324(5)	5.51097(5)	125.278(9)	236.236(4)	59.059	$R_p = 4.35\%$
	<i>Pm$\bar{3}m$</i>	38%	3.894027(2)						90
300	<i>P4bm</i>	-	5.50882(4)		3.89871(5)	90	118.315(2)	59.158	$R_p = 4.28\%$ $R_{wp} = 5.30\%$ $\text{Chi}^2 = 1.466$
400	<i>P4bm</i>	-	5.51614(4)		3.905036(5)	90	118.822(2)	59.411	$R_p = 4.32\%$ $R_{wp} = 5.30\%$ $\text{Chi}^2 = 1.479$
600	<i>Pm$\bar{3}m$</i>	-	3.912217(1)			90	59.87820(3)		$R_p = 4.53\%$ $R_{wp} = 5.90\%$ $\text{Chi}^2 = 1.822$

^a Cell volume calculated for all space groups was transformed into a single pseudo-cubic unit cell.

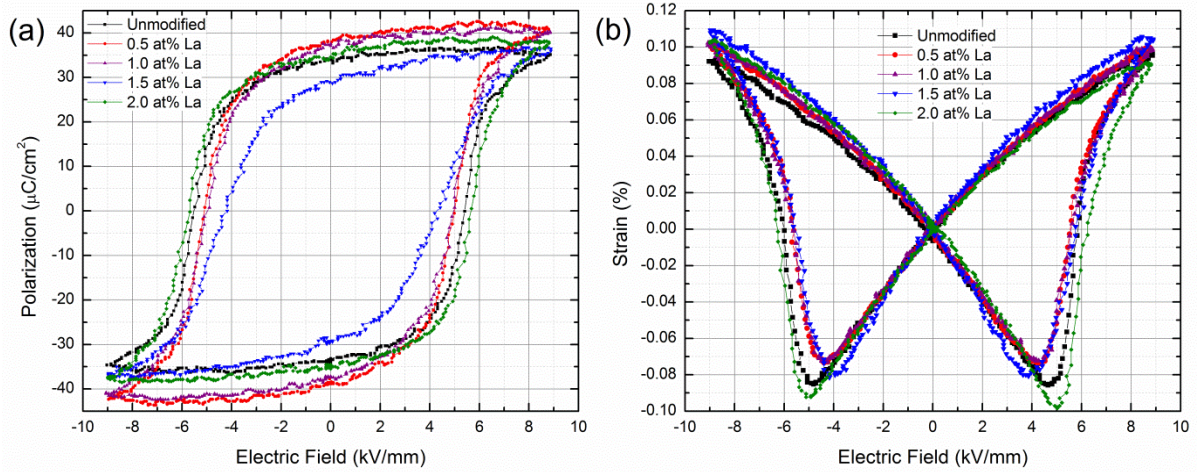


Figure 7-1. Piezoelectric properties of unmodified and La-modified NBT. A) Polarization and B) strain measurements as a function of applied electric field at a frequency of 1 Hz on unmodified and La-modified NBT.

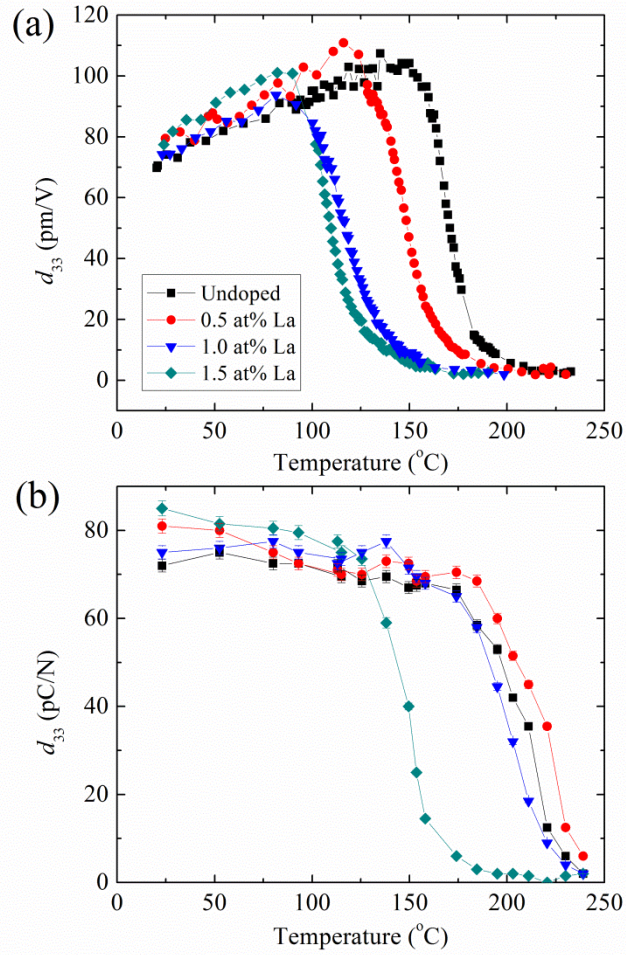


Figure 7-2. The thermal depolarization properties of NBT, measured A) *in situ*, and B) *ex situ*.

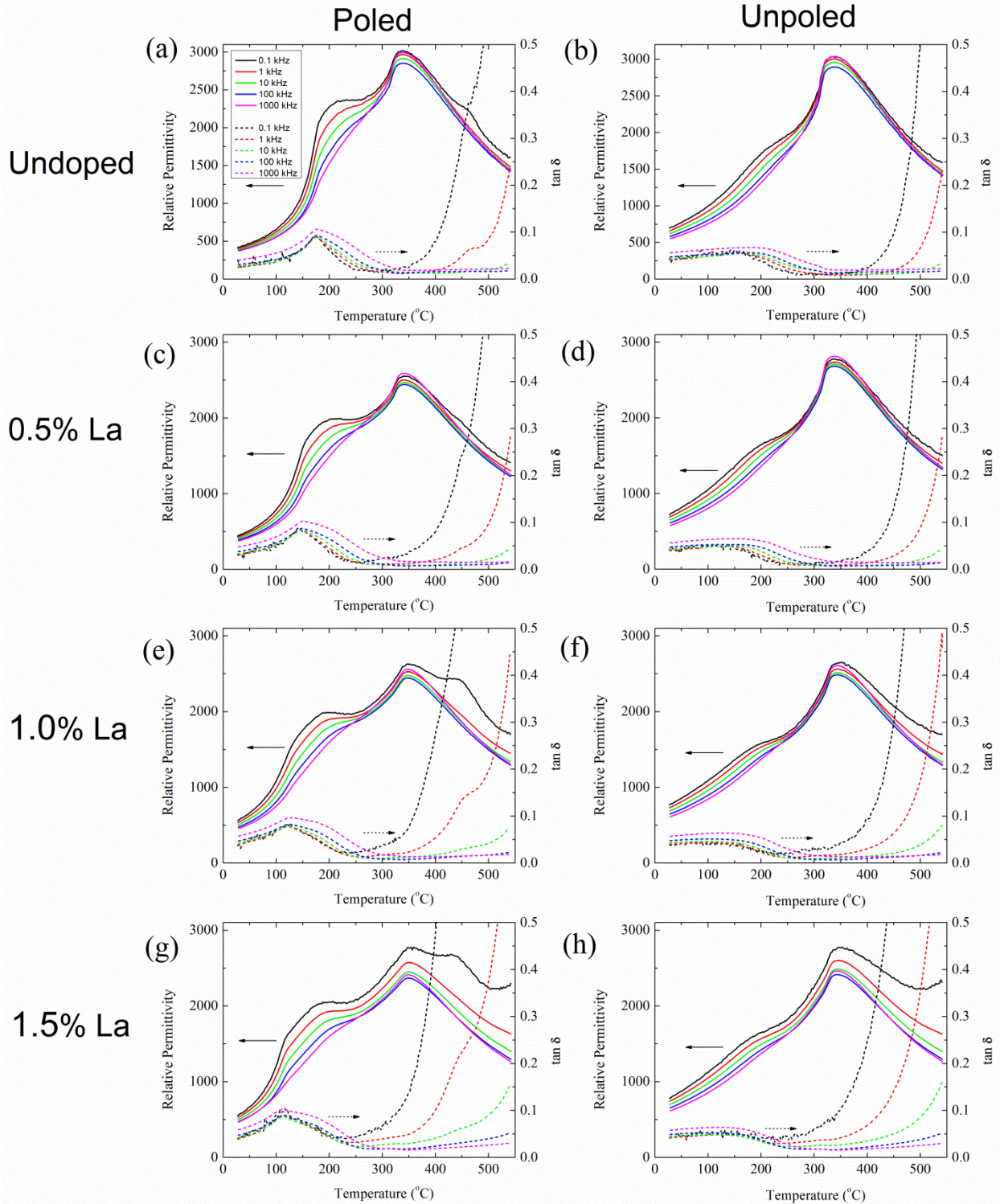


Figure 7-3. Permittivity at selected frequencies was measured with temperature for NBT samples modified with La in compositions ranging from 0-1.5 at%. The measurements were performed on poled samples then repeated on depoled sample.

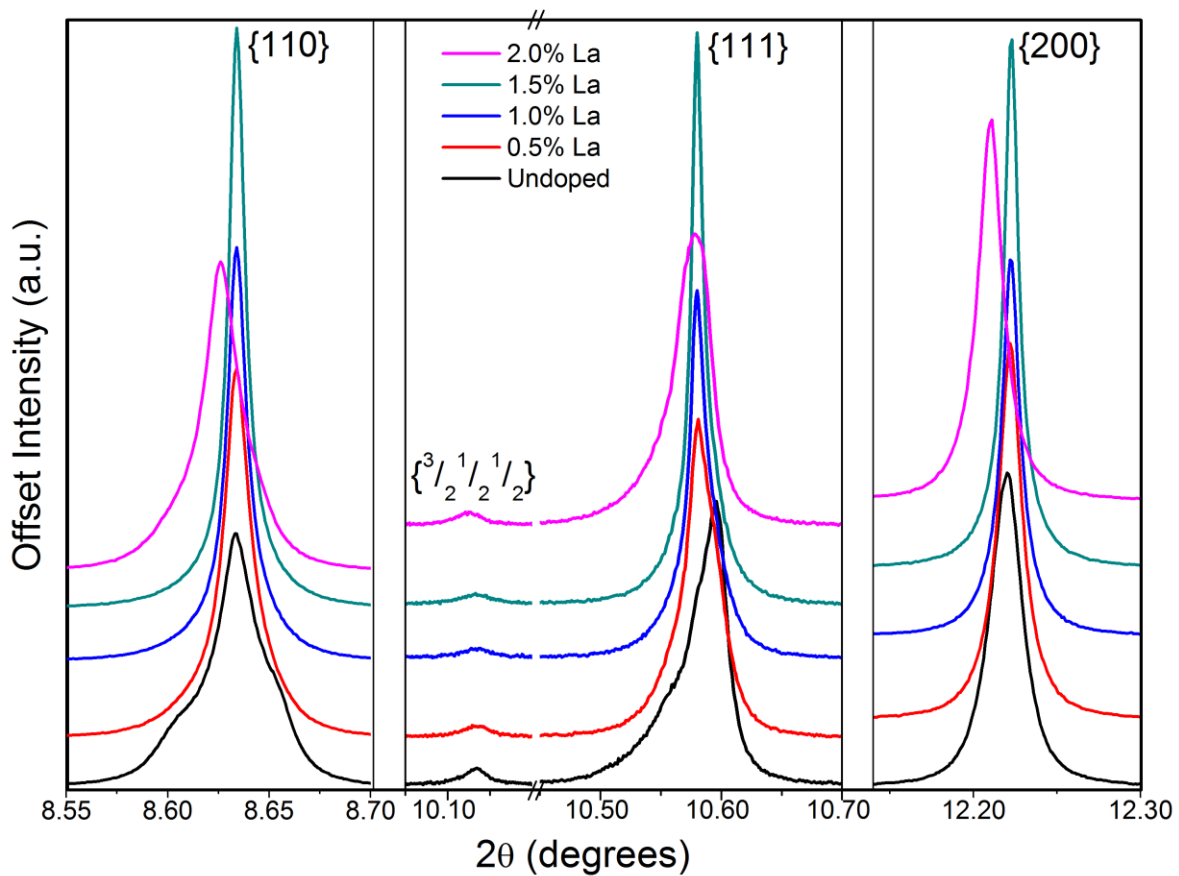


Figure 7-4. Excerpts of high resolution XRD patterns of NBT with varying La modification. For simplicity, peaks are labeled relative to the pseudo-cubic planes.

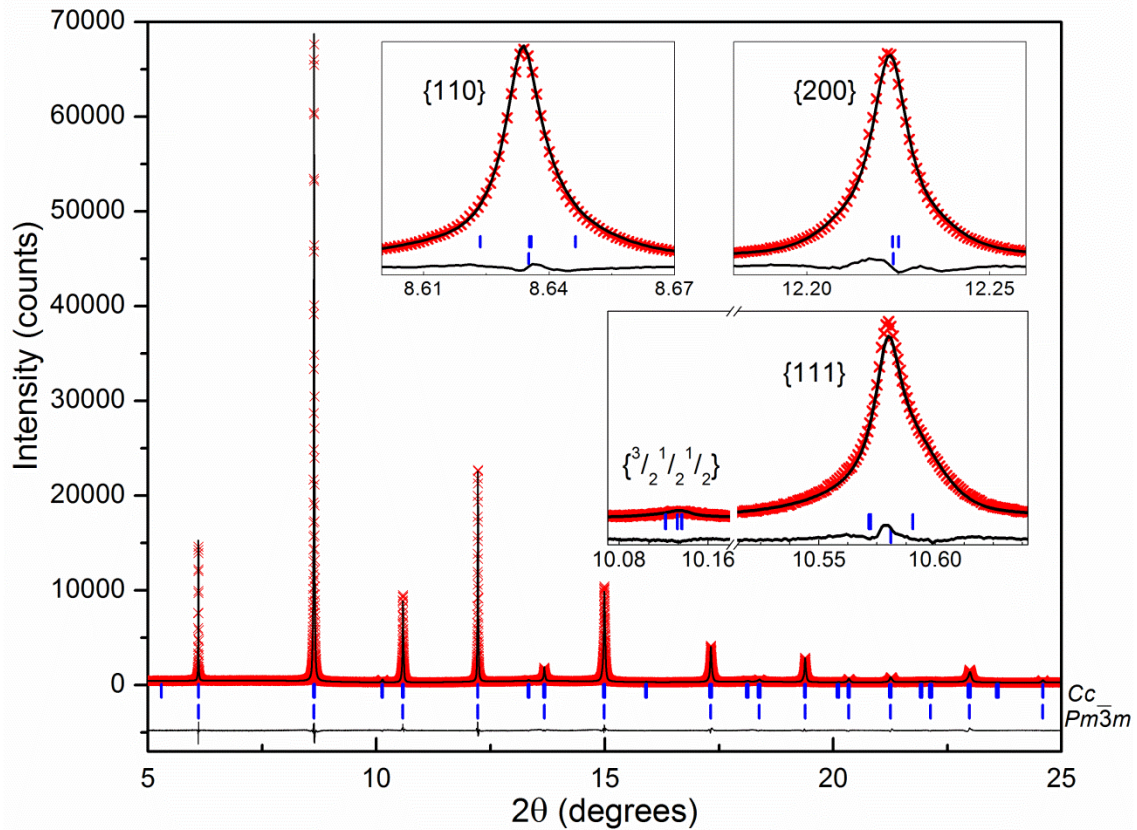


Figure 7-5. Rietveld refinement of a high resolution XRD pattern of 1% La-modified NBT showing the observed pattern (x) and the calculated fit (—). The line beneath is the difference between the observed and calculated intensities.

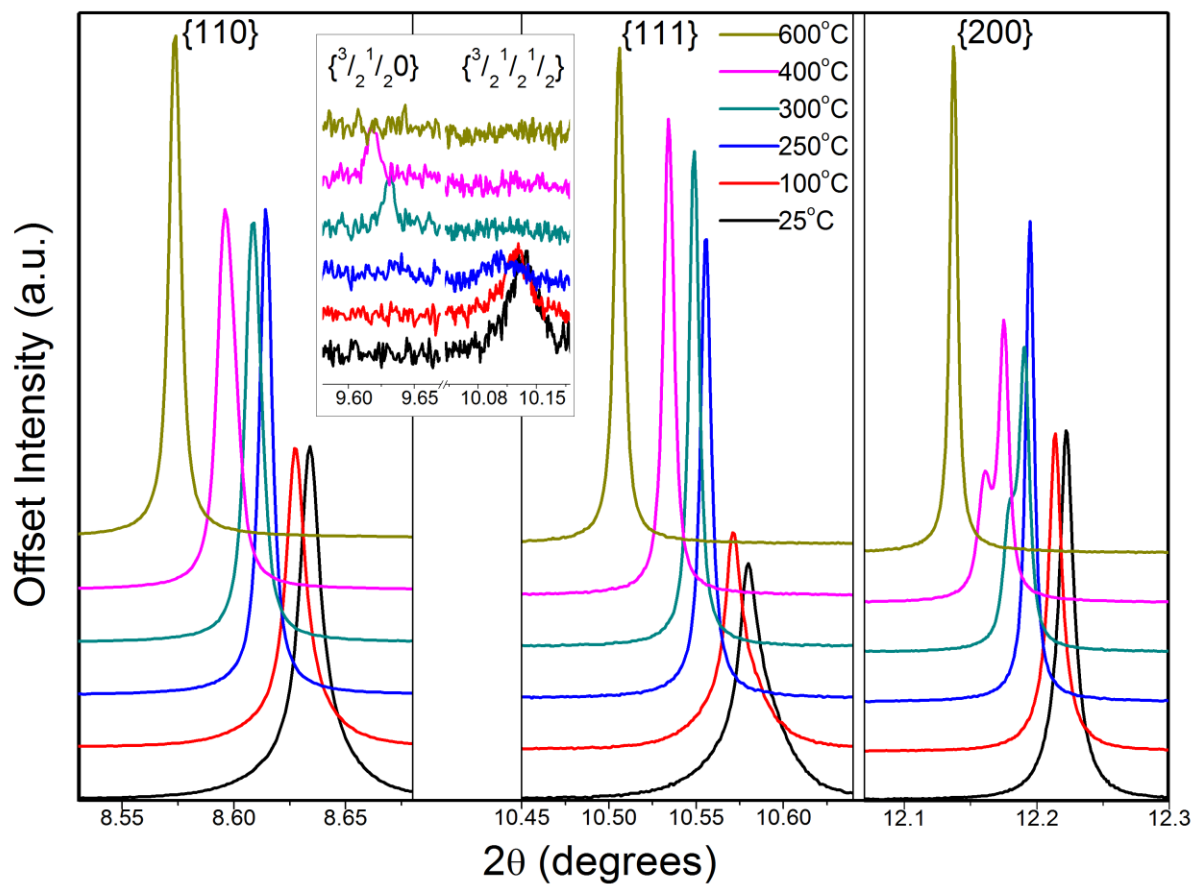


Figure 7-6. Excerpts of high resolution XRD patterns of 1% La-modified NBT at selected temperatures.

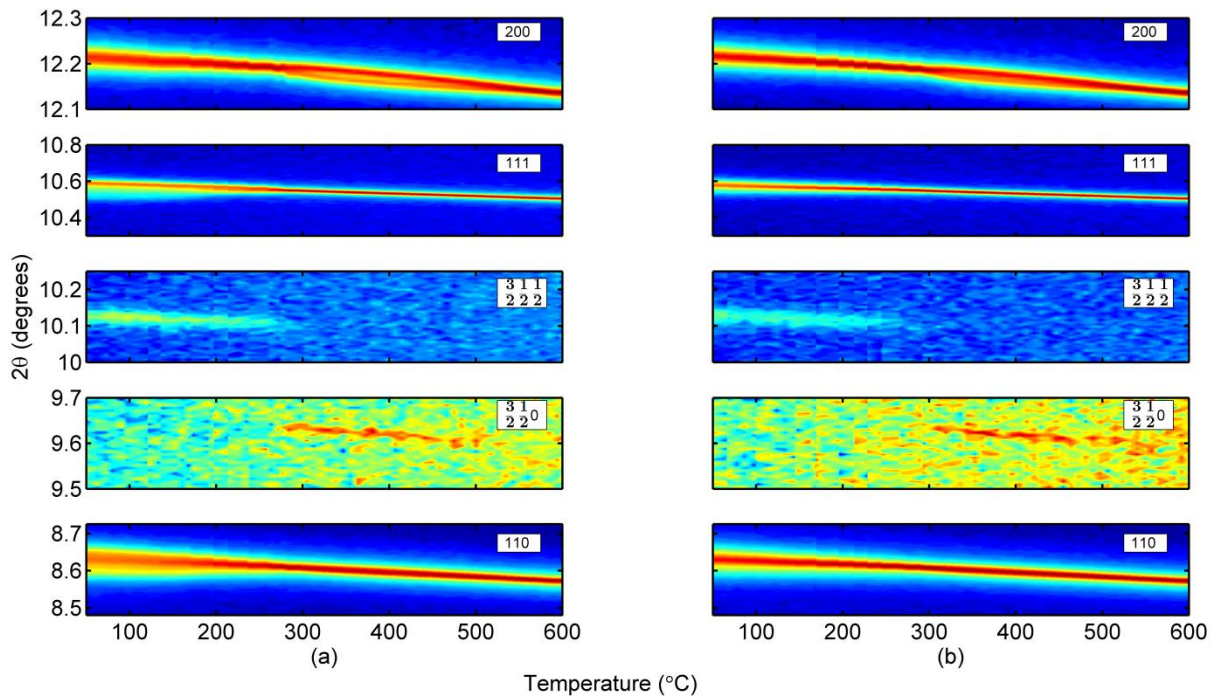


Figure 7-7. Selected areas of XRD patterns of A) unmodified and B) 1% La modified NBT plotted as a function of temperature.

CHAPTER 8 STRUCTURE AND PROPERTIES OF FE-MODIFIED NBT AT AMBIENT AND ELEVATED TEMPERATURES

Motivation

As shown in Chapter 7, the T_d of NBT may be modified through the addition of dopants or through the use of solid solution alloying with other perovskite structures. For example, Watanabe *et al.* presented the impact of several lanthanide dopants substituted on the perovskite A-site of NBT and found that the T_d of NBT decreased with increased dopant content.³³ Davies *et al.* showed an increase in the T_d with substitution of Fe or Mn on the perovskite B-site.³⁶ These modifiers also increased the piezoelectric coefficient at higher temperatures prior to piezoelectric depolarization.³⁶ In solid solutions of NBT with barium titanate BaTiO₃ (BT), Hiruma *et al.* showed a decrease in T_d with addition of BT up to 6%, which is in the area of the proposed morphotropic phase boundary between NBT and BT, and an increase with further addition of BT.¹¹⁴

In the NBT-BT system it was shown by Raman spectroscopy that the T_d is characterized by a loss of long-range ferroelectric order (which is maintained on the short range), rather than being a structural phase transition.¹¹⁵ The first-order Raman signal, originating from the center of the Brillouin zone, probes coherent scattering on the nanometer length scale and is thus sensitive to short-range order in a crystal lattice.¹¹⁶⁻¹¹⁹ Raman spectroscopy has been used to study phase transitions and the nanoscale structural characteristics of NBT and its solid solutions.^{115, 120-124} Due to challenges of intrinsic broadening and overlapping of phonon modes in the assignment of mode symmetries, structural analysis relies on analyzing soft-mode or hard-mode

Reprinted with permission from E. Aksel, J. S. Forrester, B. Kowalski, M. Deluca, D. Damjanovic, and J. L. Jones, *Physical Review B* **85**, 024121 (2012), copyright by the American Physical Society (2012).

behavior as a function of composition, pressure or temperature.^{115, 121-124} Other studies in NBT-BT¹²⁵ and NBT-SrTiO₃¹²⁴ generally supported the theory that transitions involving ferroelectric behavior are related to subtle local structural distortions and phase coexistence.

In this chapter, the long and short range structures in NBT and Fe-modified NBT are examined by Raman spectroscopy and X-ray diffraction (XRD) with the aim of understanding the effect of Fe modification on T_d and other piezoelectric properties. The content of this chapter is reprinted with permission from E. Aksel, J. Forrester, B. Kowalski, M. Deluca, D. Damjanovic, and J. L. Jones, "Structure and properties of Fe-modified Na_{0.5}Bi_{0.5}TiO₃ at ambient and elevated temperature," *Physical Review B*, Vol. 85, No. 024121, copyright (2012) by the American Physical Society.¹²⁶ In PZT, Fe substitution is referred to as acceptor doping due to the aliovalent substitution of Fe³⁺ ions for the Zr⁴⁺ and Ti⁴⁺ B-site ions.³² Extensive studies have shown that chemical modification of Ti-based perovskite ferroelectrics with Fe generally leads to so-called material "hardening" characterized by a decrease in the permittivity and piezoelectric coupling factor accompanied by an increase in the mechanical and electrical quality factor.^{32, 34} Effects of Fe modification on NBT include a slight decrease in the T_c , resistivity, and planar coupling factor as well as an increase in the coercive field,³⁵ consistent with Fe modified PZT. Davies *et al.* also examined Fe doping in NBT and found that the addition of Fe leads to an increase in T_d and a decrease in the room temperature piezoelectric coefficient.³⁶ Even when Fe₂O₃ is used as a sintering aid (0.15 at% Fe decreased the sintering temperature to 850°C),¹²⁷ there is a possibility that Fe can incorporate into the lattice and thus affect properties.

Experimental

Samples were prepared using solid state synthesis techniques as described in Chapter 3 with Fe_2O_3 to obtain concentrations of 0, 0.5, 1.0, 1.5, and 2.0 at% Fe. The addition of Fe_2O_3 to the samples was compensated by an appropriate reduction in TiO_2 . For synchrotron XRD, pellets were crushed into fine powder using a mortar and pestle, and annealed at 400°C for 3 h in a closed alumina crucible to reduce intra-granular residual stresses. The experimental details for the piezoelectric depolarization, permittivity, and high resolution XRD given in this chapter are described in Chapter 7. A single peak fitting procedure was also used to examine the evolution of several selected diffraction peaks as a function of temperature. A polynomial function was used to model the background of the entire diffraction pattern. An asymmetric Pearson VII-type profile shape function¹²⁸ was also used to fit individual Bragg peaks by employing a least squares algorithm in the program MATLAB (The Mathworks Inc., ver. 7.3.0.267).

Raman spectra were obtained with a LabRAM microprobe system (ISA/Jobin-Yvon/Horiba, Villeneuve d'Ascq, France) using a 532.02 nm Nd:YAG solid state laser as the excitation source. Surfaces of unpoled sintered pellets were prepared by polishing with 1 μm diamond paste. The laser light was focused on the sample surface by means of a long working distance and 100x (N.A.=0.8) objective lens (LMPlan FI, Olympus, Japan), allowing the laser beam spot width to be ~ 1 μm on the investigated position. Effective power at the sample surface was set to 3 mW. Spectra were recorded in a true backscattering geometry with the aid of a Peltier-cooled charged coupled device camera allowing a spectral resolution of 1.5 ± 0.1 $\text{cm}^{-1} \cdot \text{pixel}^{-1}$ for the investigated range. Temperature-dependent (*in situ*) Raman experiments were performed in the range 25-255°C (step: 10°C) by means of a Linkam MDS600 heating-cooling stage (Linkam,

Tadworth, UK). Temperature accuracy of the stage was monitored by means of CO₂ and H₂O inclusions in transparent minerals. Due to sample expansion with increasing temperature, spectra were recorded on different areas of the sample, which required re-focusing at each temperature interval. The measured spectra were then deconvoluted and analyzed using commercial software (PeakFit, Systat Software Inc., San Jose, CA). Multiple Gaussian-Lorentzian peak functions were used to model the recorded spectra.

Results

Temperature Dependence of Properties

Measurements of the longitudinal piezoelectric coefficient, d_{33} , as a function of temperature both *in situ* (converse) and *ex situ* (direct), were reported previously by Davies *et al.*³⁶ and these are reproduced in Figure 8-1. Both types of measurements show that the addition of a low Fe concentration (i.e., 0.5 at%) leads to an increase in the T_d without a reduction in the room temperature d_{33} . At 1 at% Fe, the T_d remains as high as in the 0.5 at% Fe sample, but a decrease in the room temperature d_{33} is observed. Further increase in Fe content leads to a reduction in both the room temperature d_{33} and the T_d . A summary of the measured depolarization temperatures (determined in Ref. ³⁶) is provided in Table 8-1.

Permittivity and loss tangent were also measured as a function of temperature for poled and unpoled samples of the same compositions. Figure 8-2 shows the permittivity and loss tangent measured at five different frequencies for unmodified and 0.5 at% Fe modified NBT. A large increase in apparent permittivity and loss with temperature is observed in the 0.5 at% Fe sample for low frequencies (Figure 8-2C and D) which is most likely due to conductivity. Permittivity and loss of samples with a higher Fe content are not shown due to the strong effect of conductivity. A peak in the loss tangent vs.

temperature plot and an inflection point in the permittivity vs. temperature plot are observed around the T_d for the poled samples. Frequency dispersion is observed in all measured compositions and poling states, consistent with relaxor-type behavior.^{77, 129} The peak in the loss tangent vs. temperature plot is at 176°C for unmodified NBT and at 202°C for 0.5 at% Fe modified NBT (Table 8-1). It is interesting to note that while a distinct peak arises in the loss tangent vs. temperature plot at the T_d for both poled samples (Figure 8-2A and C), it is more subtle for unpoled samples (Figure 8-2B and D). A slight change in the rate of this transition is also apparent after a small addition of Fe. A sharper increase in permittivity at the T_d is observed in the 0.5 at% Fe (Figure 8-2C) sample than in the unmodified one (Figure 8-2A). This behavior is mirrored in the *in situ* depolarization measurements (Figure 8-1A), in which the depolarization of the 0.5 and 1.0 at% Fe samples occurs in a narrower temperature range than the unmodified sample. Additional results of property measurements conducted on Fe-modified NBT can be found in Appendix D.

Crystallographic Structure of Unmodified and Fe-Modified NBT by XRD

Figure 8-3 shows the evolution of selected Bragg peaks with Fe modification, as observed in synchrotron XRD patterns. The indexed reflections are labeled relative to the pseudo-cubic unit cell. To extract structural information, the diffraction patterns were analyzed using Rietveld refinement. All room temperature data were modeled using the Cc space group, similar to the previous work presented in Chapter 3. A sample refinement of the 1 at% Fe sample data is presented in Figure 8-4. The Cc model used in this refinement has fully accounted for the reflections in the XRD pattern and therefore it can be inferred that there are no second phases present, to the resolution of the XRD data. An examination of the individual diffraction peaks (in particular the 110

reflection) supports the previous finding in Chapter 3 that the rhombohedral $R3c$ structure cannot fully account for splitting in the peaks.

Changes in the unit cell as well as the criteria of fit are given in Table 8-2. A comprehensive summary of the refinement results for the various Fe modified samples is available in Appendix C, Table C-1. With increasing Fe concentration, the a and c lattice parameters and monoclinic angle (β) increase while the b lattice parameter generally remains constant, indicating that no phase transitions occur. The increase in the lattice parameters and monoclinic angle indicates that the structure distorts further from the prototypical cubic structure with increasing Fe content. Although the oxygen positions were refined in this analysis, they are inconsistent for an octahedral tilting calculation, due to the insensitivity of X-rays to oxygen. It is possible, however, to infer from the increasing ferroelastic distortion with the addition of Fe that the octahedral tilting increases with Fe substitution. Extra peaks in the XRD pattern of the 2% Fe-modified sample, such as the one at $10.5^\circ 2\theta$ (Figure 8-3), are indicative of a second phase. Indexing the extra peaks revealed that the secondary phase took the perovskite structure, and one possibility is BiFeO_3 (BFO). Adding the starting model¹³⁰ of BFO as a second phase provided a good model to the XRD pattern, as seen in the criteria of fit values in Table 8-2.

To determine the preferred perovskite lattice site for Fe substitution, refinements were attempted where Fe shared the A-site with Na/Bi, although this model led to an unstable refinement. As expected, substitution of Fe on the B-site resulted in a stable refinement, consistent with the substitution scheme in PZT. An attempt was also made to quantify the occupancies of Fe and Ti on the B-site. For this determination, the initial

values for the occupancies were the expected values based on the nominal stoichiometry (e.g. for the 1% Fe sample the occupancy of Ti was set to 0.99 and Fe to 0.01). A refinement of the occupancies provided little change to the starting values. Manual adjustment of the starting values also did not affect the quality of fit. Thus, it was inferred that this method is not sufficiently sensitive to discern the exact Fe occupancy on the B-site, most likely because Fe and Ti have similar X-ray atomic scattering factors.

Structural analysis was also carried out on the XRD patterns of a 1 at% Fe sample as a function of temperature. A compilation of the patterns is presented in Figure 8-5. Each pattern was modeled via the Rietveld method, with a selection of the refined structural information given in Table 8-3. The full refinement results are presented in Appendix C, Table C-2. These results indicate that the evolution of the structure follows a transition from monoclinic *Cc* to tetragonal *P4bm* and finally to cubic *Pm $\bar{3}$ m*, with the tetragonal and cubic phases consistent with previous work from Jones and Thomas.²⁴ At 250°C it was found that the *Cc* space group could no longer adequately model the pattern. Several phase combinations were trialed, such as *Cc+R3c*, *Cc+P4bm*, *Cc+Pm $\bar{3}$ m*, and *R3c+Pm $\bar{3}$ m*. The phase combination of *Cc+Pm $\bar{3}$ m* provided the closest model to several aspects of the pattern, including the asymmetry and decreased intensity of the $\{3/2\ 1/2\ 1/2\}$ reflection, and the peak splitting present in the $\{110\}$ and $\{111\}$ peaks. The addition of the *Pm $\bar{3}$ m* space group was used to describe local disorder in the average structure which can create small variations in the diffraction patterns that cannot be entirely modeled using a single phase *Cc* structure.

While the information presented in Figure 8-5 and Table 8-3 is provided at discrete temperatures, an additional measurement was undertaken where XRD data of unmodified and 1 at% Fe modified NBT was measured continuously as a function of temperature up to 600°C. Figure 8-6 shows the evolution of several of the perovskite reflections of NBT (Figure 8-6A) and 1% Fe-modified NBT (Figure 8-6B) from room temperature to 600°C. Structural transitions in the material are apparent through the observed changes in the peak splitting. For example, the {200} peak splitting into two peaks above approximately 285°C for unmodified NBT correlates with a phase transition to tetragonal $P4bm$. To examine the presence of structural transitions around the depolarization temperature, the splitting in the {110} peak was evaluated using a single peak fitting procedure with three asymmetric Pearson-VII peak profiles. Based on this fit, a phase transition temperature is estimated when two of the component peaks are indistinguishable within the error of each other. This is observed at 195°C for unmodified NBT and 220°C for 1% Fe-modified NBT. The average error associated with these temperatures, based on a 5°C/min heating rate, is +/- 9°C. These results are qualitatively consistent with the changes observed in Figure 8-6.

Raman Spectroscopy of Unmodified and Fe-Modified NBT

A representative Raman spectrum of unmodified NBT and its deconvolution is displayed in Figure 8-7A. The spectrum is consistent with previous reports,^{115, 121-124} where it was assigned as characteristic of the pseudo-rhombohedral $R3c$ phase, for which a total of 13 Raman-active modes ($\Gamma_{\text{Raman}, R3c} = 4A_1 + 9E$) are expected.¹²³ Three main regions can be discerned. The first one at $\sim 270 \text{ cm}^{-1}$ is dominated by an A_1 mode assigned to Ti-O vibrations. The mid-frequency region at around $450\text{-}700 \text{ cm}^{-1}$ hosts modes associated with the vibration of the TiO_6 octahedra, most likely as a

superposition of transverse optical (TO) and longitudinal optical (LO) bands of A_1 character. The high-frequency region above 700 cm^{-1} has been linked to $A_1(\text{LO})$ and $E(\text{LO})$ overlapping bands.¹²⁴

The Raman spectra of unmodified and modified NBT at room temperature are displayed in Figure 8-7B. Figure 8-7C shows the Raman spectra of unmodified NBT as a function of increasing temperature. The temperature-dependent spectra for the other compositions exhibit similar behavior as observed in the unmodified NBT. The intensities of all represented spectra were corrected for the Bose-Einstein temperature factor. No consistent variation in the peak positions was measured with increasing Fe substitution at room temperature, which is compatible with the small difference in atomic mass on the B-site upon Fe substitution. This is in accordance with observations from XRD and with the fact that Raman spectra are generally only slightly affected by such small concentrations of modifiers. No contribution from the secondary phase of BFO is observed in the measured spectrum of the 2 at% Fe composition most likely because of the proximity of the Raman-active modes of BFO to those of the NBT primary phase.¹³¹

With increasing temperature, thermally-induced broadening occurs, which in the case of NBT could also support the theory that higher structural disorder exists in the Ti-O bond of the TiO_6 octahedra with increasing temperature; such behaviour may be associated with the nucleation of nanodomains within the ferroelectric matrix. This has been suggested in previous work.^{77, 115, 117} In particular, the loss of long-range ferroelectricity at T_d was proposed as related to the nucleation of antiparallel nanodomains with tetragonal $P4bm$ structure.^{77, 115} The onset of a secondary phase within the primary one will surely influence the strength of the Ti-O bond, and should

thus be visible by examining the softening of the A_1 mode at $\sim 270 \text{ cm}^{-1}$ upon increasing temperature. The temperature dependence of this mode for all compositions is represented in Figure 8-8. The displayed results are the average of three experimental runs, on the basis of which the standard deviation is represented as an error bar. The experimental error is contributed by minor differences in characteristics (e.g., local density fluctuations and microscopic residual stress) between each probed position in the sample. An overall softening of the phonon line center is detected over the investigated temperature range, and most compositions present an anomaly in the neighborhood of the expected T_d value obtained from the piezoelectric depolarization measurements (*cf.* Table 8-1). Peak softening with temperature is observed due to anharmonic terms in the vibrational potential energy.¹³² This can be generally described by the following equation, taking into account terms of up to four phonons:

$$\omega(T) = \omega_0 + A \left[1 + \frac{2}{e^x - 1} \right] + B \left[1 + \frac{3}{e^y - 1} + \frac{3}{(e^y - 1)^2} \right] \quad (8-1)$$

where $x = \hbar\omega_0/2kT$, $y = \hbar\omega_0/3kT$, with k the Boltzmann's constant and \hbar the reduced Planck's constant; A , B and ω_0 are fitting parameters, and T is temperature, which is the independent variable. In the absence of a phase transition with increasing temperature, the phonon softening can be defined by a single theoretical curve given by Equation (8-1). In the case of anomalies in the phonon softening behavior, normally a collection of curves with different fitting parameters can fit the experimental data. The point where two such adjacent curves join can be regarded as the phase transition temperature.¹³³⁻
¹³⁵ The data in Figure 8-8 are modeled with two curves of Equation (8-1) for each composition (solid red curves). The intersection of these two curves can be considered

an anomaly in the A_1 phonon. For pure NBT and NBT modified with 0.5 at% and 1 at% Fe content (Figure 8-8A, B and C) an anomaly point corresponding to the expected T_d (cf. Table 8-1) was determined, whereas the high experimental error prevented the detection of any anomaly in the two Fe-rich compositions (Figure 8-8D and E).

Discussion

Analysis of the high resolution diffraction data indicates that the room temperature structure of NBT and Fe-modified NBT is monoclinic in the Cc space group, in agreement with previous reports.^{28, 59} Although the Raman spectra measured in this work are consistent with the previous assignment of an $R3c$ structure, this result does not exclude the presence of a monoclinic Cc phase on average. Raman spectroscopy is sensitive to the short-range crystalline order, which below T_d is dominated by the B-site polarization along the rhombohedral [111] axis. In addition, resolving the higher number of Raman modes associated with a monoclinic Cc cell might prove challenging unless resonance conditions are induced.¹³⁶

The piezoelectric depolarization measurements of unmodified and 1% Fe modified NBT and the high temperature XRD measurements show a transition in the same temperature range for both methods, indicating that the depolarization of NBT may be related to structural changes. The presence of a structural change is further supported by refinement of an XRD pattern of 1% Fe modified NBT at 250°C, at which temperature a mixture of Cc and $Pm\bar{3}m$ phases exists. The $Pm\bar{3}m$ phase may describe the contribution to the diffraction pattern resulting from the observation of a long-range modulated phase of $Pnma$ platelets proposed by Dorcet *et al.*²⁶ Similar changes with temperature have been observed in unmodified NBT.¹⁰⁴ In this prior work

(presented in Chapter 6), the thermal depolarization was correlated with an increase in the volume fraction of material which does not correlate with the long-range Cc space group.¹⁰⁴ A small inclusion of this secondary phase (2 wt%) in unmodified NBT was also observed at room temperature.¹⁰⁴ It may represent the previously reported nano-scale platelets of space group $P4bm$ within the room temperature structure.^{25, 27} When measured using longer-range probes such as X-ray diffraction, these fractions of the material may result in broadening of the diffraction peaks, as observed in the present work (*cf.* Figure 8-3).

An inclusion of the $Pm\bar{3}m$ phase at room temperature was also trialed for the Fe-modified compositions, and a decrease in the $Pm\bar{3}m$ phase fraction was observed with increasing Fe content. Due to the very small contribution of the room temperature $Pm\bar{3}m$ phase, a quantitative phase fraction analysis is not presented. However, possible changes in the phase fraction of this local structure may still be postulated from the diffraction data measured at room temperature as a function of Fe content. For example, the results in Figure 8-3 highlight an increase in definition of the 110 and 111 peak splitting with increased Fe content. Since the constituent peak positions do not shift significantly in the observed X-ray pattern, it is possible that the enhanced definition results from narrowing sample contribution to peak broadening with increased Fe substitution. This change in peak shape may be associated with a decreased contribution from a secondary phase such as $Pm\bar{3}m$, and is consistent with the decrease in the refined $Pm\bar{3}m$ phase fraction for compositions with increasing Fe substitution. From this result, it is suggested that with increasing Fe substitution, the amount of this type of local disorder decreases and the structure becomes closer to the

long-range *Cc* structure. This change also correlates with the increased distortion of the unit cell and possible increased octahedral tilting, as observed in the increasing *a* and *c* lattice parameters as well as the monoclinic β angle (*cf.* Table 8-2).

Although previous TEM studies propose the formation of an orthorhombic *Pnma* phase around the T_d ,²⁶ the Raman results in this work do not support the presence of such a phase in this range. Since the A_1 and E bands in the 450-700 cm^{-1} range lose their LO and TO character (loss of infrared activity) upon transition to the orthorhombic structure¹²², it is likely that peak coalescence should be observed. In the current results, the changes in this wavenumber range (apparent peak coalescence, *cf.* Figure 8-7C) cannot be associated with a transition to such a phase. Firstly, the group-theoretical calculation for the *Pnma* phase yields $\Gamma_{\text{Raman},Pnma}=7A_g+7B_{1g}+5B_{2g}+5B_{3g}$,¹³⁷ i.e., 24 Raman-active modes, of which some should appear for wavenumbers $<400 \text{ cm}^{-1}$.¹²² In the present observation, no extra modes appeared in this range. Secondly, such peak coalescence can be mimicked by other effects such as the thermal broadening of adjacent modes.

The Raman results support (in most compositions) the presence above T_d of a phase with symmetry higher than orthorhombic *Pnma*, such as tetragonal *P4bm*. The anomaly in the response of the A_1 phonon at $\sim 270 \text{ cm}^{-1}$ with rising temperature can be related to changes in the Ti-O bond upon nucleation of a different phase. The presence in the lattice of nanodomains of tetragonal phase would in fact produce the local re-orientation of A-site cations along the [001] pseudo-cubic direction. This is expected to influence the strength of the Ti-O bond, thus causing in the neighborhood of T_d the anomaly in the phonon at $\sim 270 \text{ cm}^{-1}$. The nature of the higher experimental error, which

prevented the detection of an anomaly point at T_d for the compositions with Fe > 1.5 at%, is not fully understood. It could be however supposed that higher Fe content (and possibly, the presence of a second phase) would increase chemical residual stress in the neighborhood of substitutional sites, thus producing local shift of the phonon line center. Since for each temperature a different point of the specimen surface is observed, this could explain the observed error. The changes in the A_1 phonon are detected at lower temperatures than measured by *ex situ* depolarization. This is probably due to the sensitivity of Raman spectra to changes in the short range order. These experiments cannot discriminate an antiferroelectric character of the nanodomain phase, since only wavenumbers $> \sim 150 \text{ cm}^{-1}$ can be examined with the current setting. Access to A-site modes would provide information on possible antiparallel cation-ion displacements in the $P4bm$ phase, leading to antiferroelectric properties. Further temperature-dependent Raman experiments in this wavenumber range using different excitation wavelengths (i.e., to induce resonance) may be insightful.

Depolarization measurements indicate that the addition of 0.5 and 1 at% Fe to NBT increases the piezoelectric depolarization temperature, while further increase in Fe content leads to a decrease in T_d . The initial increase in T_d with small modification by Fe is confirmed by both Raman and XRD and may be due to defect dipoles which form with the addition of Fe to NBT.¹³⁸ The presence of such defect dipoles can stabilize ferroelectric order in the material and therefore increase the T_d .¹³⁹ The subsequent decrease in T_d due to greater Fe substitution may be associated with limited ferroelectric poling due to the high conductivity of these samples. The transitions observed in Raman and XRD measurements near the piezoelectric depolarization

temperature indicate that a structural change occurs at this temperature. A similar increase then subsequent decrease in T_d was also reported for doping with Ba^{2+} by Hiruma³¹ and Cordero¹⁴⁰. This change in T_d with Ba^{2+} doping implies that similar structural changes may be taking place in Ba-modified NBT as in Fe-modified NBT.

It was observed in Figure 8-1 that with the addition of 0.5 at% Fe the room temperature d_{33} remains the same as in unmodified NBT. However, further Fe addition to the system leads to a decrease in the room temperature d_{33} value. This result is quite different from what was found in PZT. Rema *et al.* reported that with the addition of 0.5 at% Fe to a PZT based material, the d_{33} dropped significantly from approximately 370 to 250 pC/N at room temperature.¹⁴¹ The decrease in both the room temperature d_{33} and the T_d which is observed at higher levels of Fe substitution may be associated with limited substitution of Fe in this material. Although the diffraction patterns of these materials only indicates the presence of a second phase in the 2 at% Fe composition, previous work using electron paramagnetic resonance showed that a second phase forms in concentrations as low as 1.5 at% Fe.¹³⁸ This second phase could lead to increased conductivity in the compositions with higher Fe, limiting the ferroelectric poling process. It is also likely that the increase in lattice parameters between unmodified and 1.5 at% Fe has resulted in significant lattice strain. A further increase in Fe-modification beyond 1.5 at% has led to the formation of a second phase in order to decrease the lattice strain. This is an important observation for future application of these materials, as the solubility limit in PZT is higher than what was found in this study for NBT.

Summary

The crystal structure of unmodified and Fe-modified NBT was examined as a function of increasing Fe content, and with increasing temperature. The piezoelectric properties were also examined as a function of temperature in order to understand the impact of Fe on piezoelectric depolarization. The addition of Fe to NBT did not change the phase of the material, however low concentrations (i.e., 0.5 and 1.0 at%) led to an increase in the T_d followed by a slight decrease with higher Fe content. This temperature dependence in the electrical properties as a function of Fe composition was mirrored in the structural studies using XRD and Raman spectroscopy. An analysis of the XRD data as a function of temperature indicated that there is a portion of the diffraction pattern at elevated temperatures which cannot be fully described using the Cc model. This portion is attributed to a growth in the volume fraction of nano-scale regions, modeled in this work as a $Pm\bar{3}m$ phase. An anomaly in the A_1 phonon assigned to Ti-O vibrations was found to correlate well with T_d in most compositions, thus implying that a structural transition exists on the short range at a temperature near the piezoelectric depolarization temperature, and that the temperature of this transition shifts with Fe addition. The analysis of the XRD patterns and the Raman spectra as a function of temperature supports the view that the process of thermal depolarization in NBT-based materials occurs due to the formation of nano-scale regions which disrupt the long-range ferroelectric order rather than a long-range phase transition.

Table 8-1. Depolarization temperatures, T_d (°C), measured by Raman spectroscopy, *in situ* converse d_{33} , *ex situ* direct d_{33} and synchrotron XRD in all investigated compositions. Uncertainty in T_d determination by Raman is $\pm 10^\circ\text{C}$.

Composition	Raman spectroscopy	Converse d_{33} (<i>in situ</i>)	Direct d_{33} (<i>ex situ</i>)	Permittivity	Synchrotron XRD
Unmodified	161	161	210	176	195
0.5% Fe	201	191	233	202	-
1.0% Fe	181	190	219	-	220
1.5% Fe	-	175	199	-	-
2.0% Fe	-	177	201	-	-

Table 8-2. Refined lattice parameters and Bragg fitting values for the samples with increasing Fe-modification.

at% Fe in NBT Cc setting	a (Å)	b (Å)	c (Å)	β (°)	Cell Volume (Å ³)	Fitting Values
0	9.5255(2)	5.48262(4)	5.50751(5)	125.3467(5)	234.609(5)	R_p 5.30% R_{wp} 7.36% χ^2 4.03
0.5	9.5284(2)	5.48260(3)	5.51027(3)	125.3598(6)	234.760(5)	R_p 5.58% R_{wp} 7.88% χ^2 4.54
1.0	9.5310(2)	5.48260(4)	5.51112(5)	125.3632(5)	234.845(5)	R_p 5.54% R_{wp} 7.62% χ^2 3.23
1.5	9.5322(2)	5.48263(4)	5.51263(5)	125.3775(5)	234.902(5)	R_p 5.75% R_{wp} 8.04% χ^2 3.01
2.0*	9.5322(2)	5.48454(5)	5.51327(6)	125.3785(9)	235.007(7)	R_p 5.02% R_{wp} 7.07% χ^2 3.50

*This refinement includes the addition of BFO as a second phase.

Table 8-3. Refined lattice parameters and Bragg fitting values for 1 at% Fe-modified NBT with increasing temperature.

Temp. (°C)	Space Group	a (Å)	b (Å)	c (Å)	β (°)	Fitting Values
30	<i>Cc</i>	9.5310(2)	5.48260(4)	5.51112(5)	125.3632(5)	R_p 5.54% R_{wp} 7.62% χ^2 3.23
100	<i>Cc</i>	9.5300(1)	5.48838(2)	5.51071(3)	125.3310(3)	R_p 4.98% R_{wp} 6.67% χ^2 2.466
250	<i>Cc</i> (15%) <i>Pm</i> $\bar{3}$ <i>m</i> (85%)	9.54071(9) 3.894524(4)	5.50099(3)	5.51627(5)	125.2817(8)	R_p 4.66% R_{wp} 6.09% χ^2 2.078
300	<i>P4bm</i>	5.508967(4)	5.508967(4)	3.901071(4)		R_p 4.87% R_{wp} 6.63% χ^2 2.474
400	<i>P4bm</i>	5.515873(3)	5.515873(3)	3.907307(4)		R_p 4.64% R_{wp} 6.33% χ^2 2.245
600	<i>Pm</i> $\bar{3}$ <i>m</i>	3.912961(5)	3.912961(5)	3.912961(5)		R_p 5.04% R_{wp} 7.28% χ^2 2.931

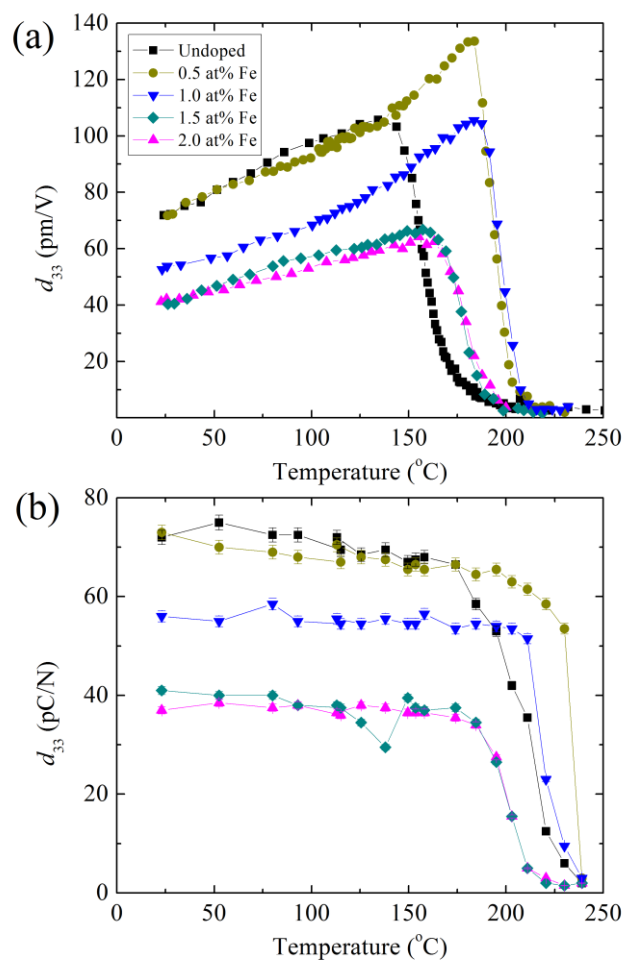


Figure 8-1. Longitudinal piezoelectric coefficient d_{33} measured as a function of temperature for various compositions of Fe-modified NBT. A) The converse d_{33} was measured *in situ* and B) the direct d_{33} was measured *ex situ*.

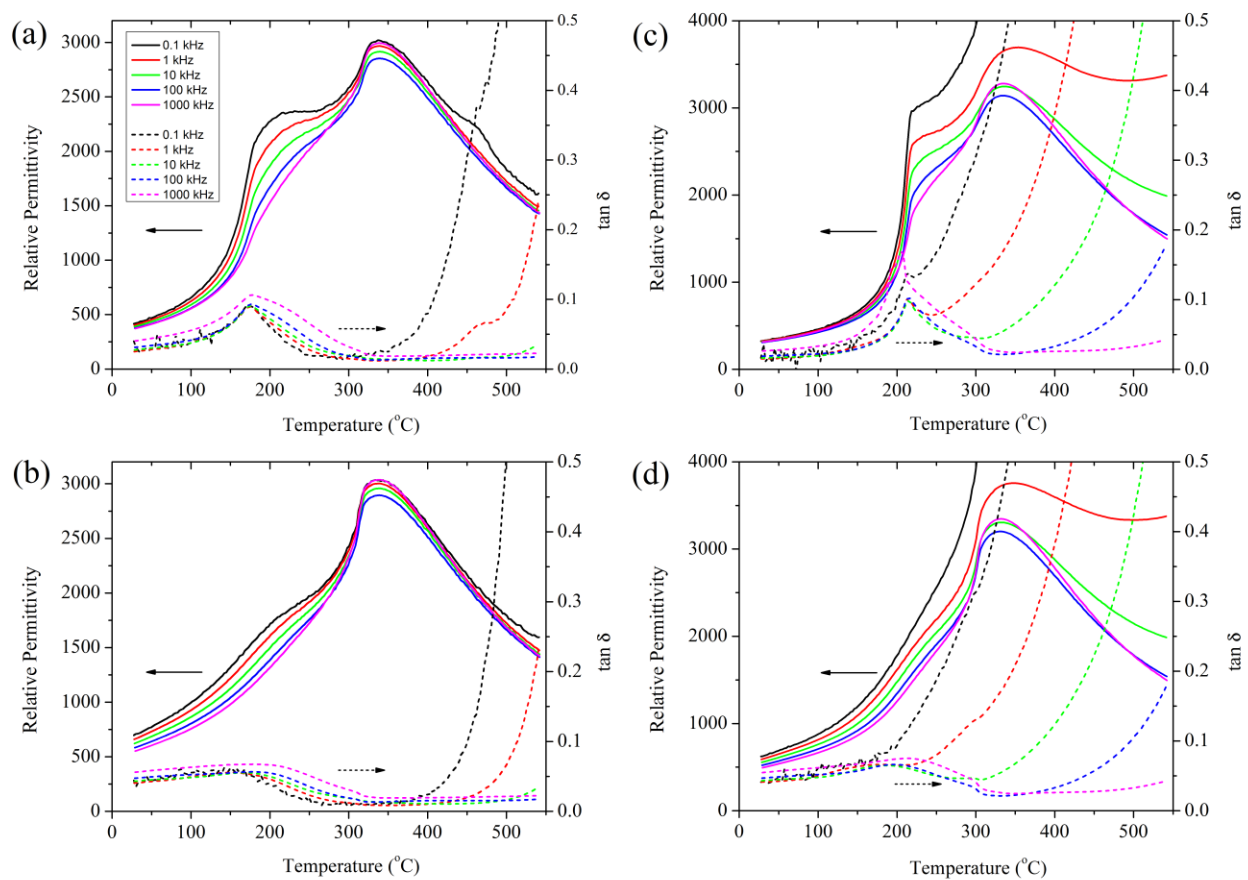


Figure 8-2. Permittivity and loss measured as a function of temperature at 0.1, 1, 10, 100, and 1000 kHz for A) unmodified NBT poled, B) unmodified NBT unpoled, C) 0.5 at% Fe modified poled, and D) 0.5 at% Fe modified unpoled.

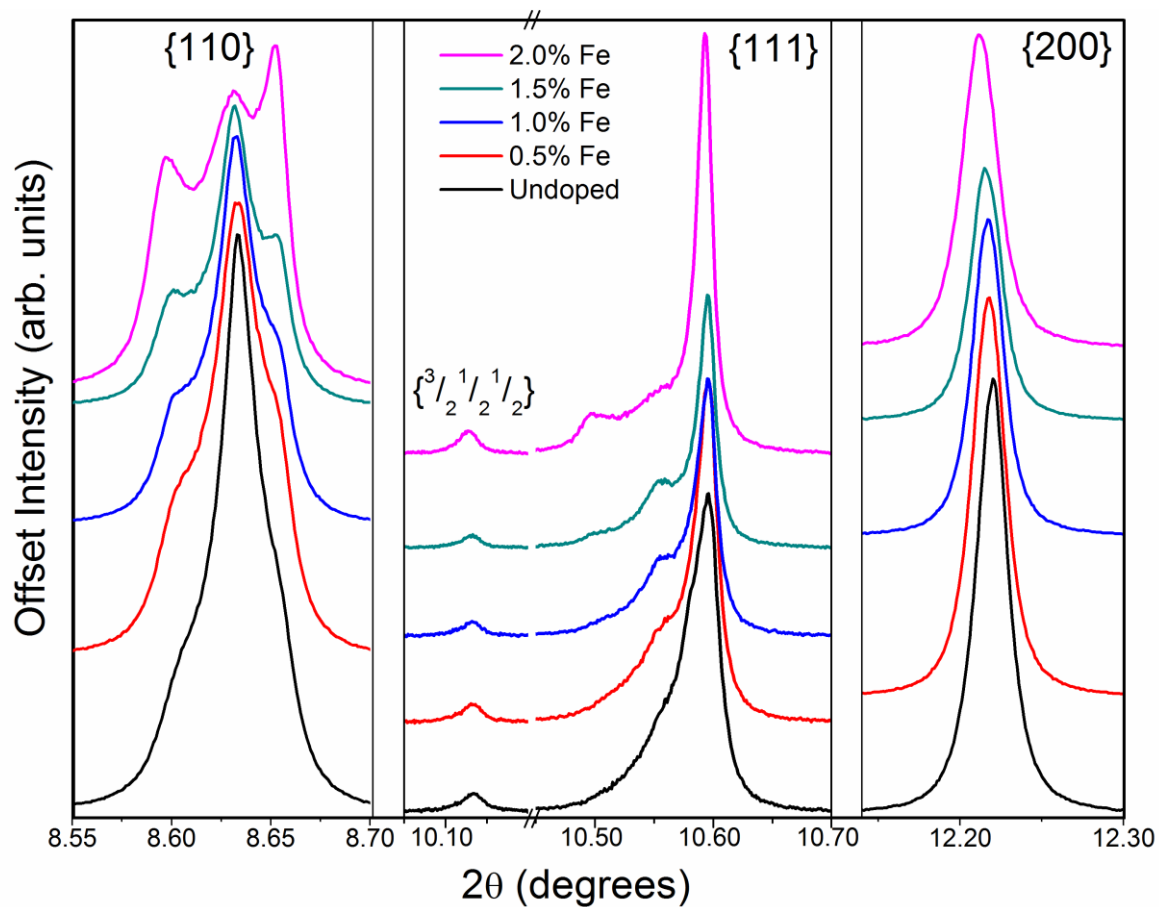


Figure 8-3. Excerpts of high resolution XRD patterns of NBT with varying Fe concentrations. For simplicity, peaks are labeled relative to the pseudo-cubic planes.

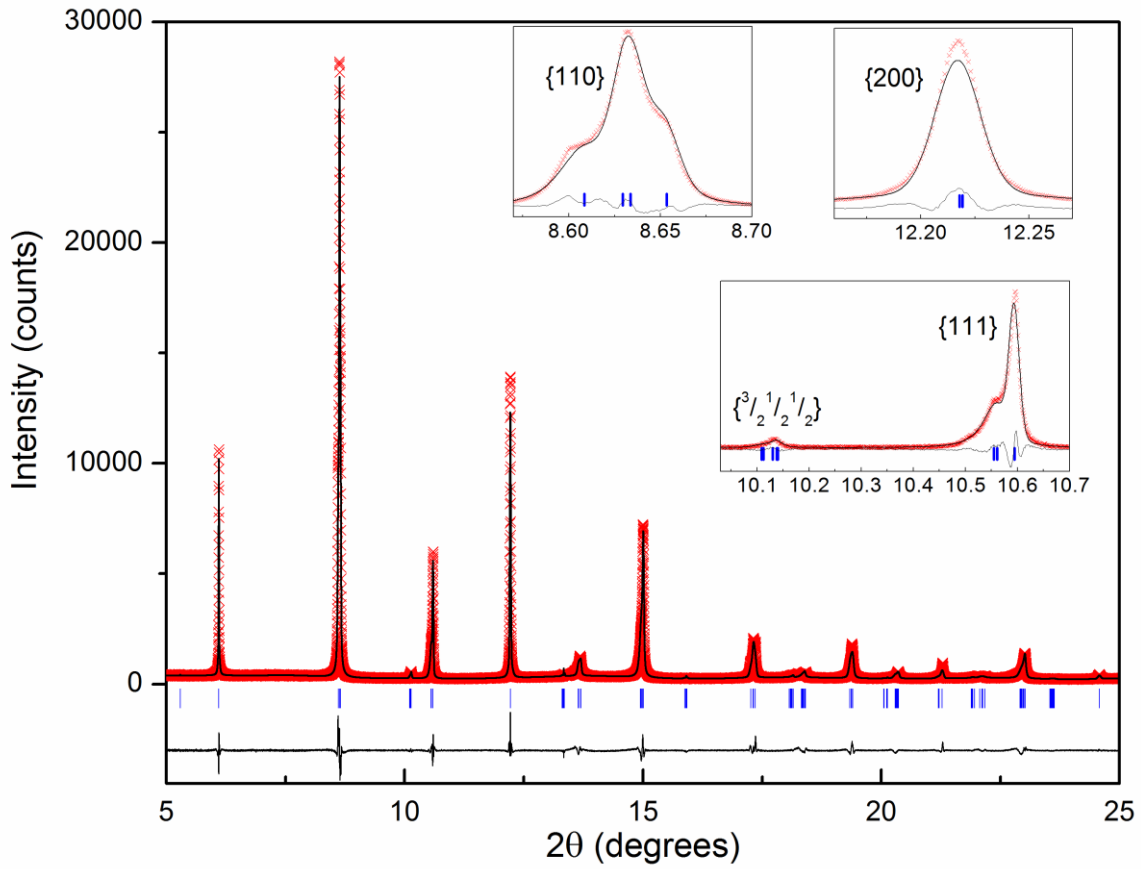


Figure 8-4. Rietveld refinement of a high resolution XRD pattern of 1% Fe-modified NBT showing the observed pattern (x) and the calculated fit (—). The line beneath is the difference between the observed and calculated intensities.

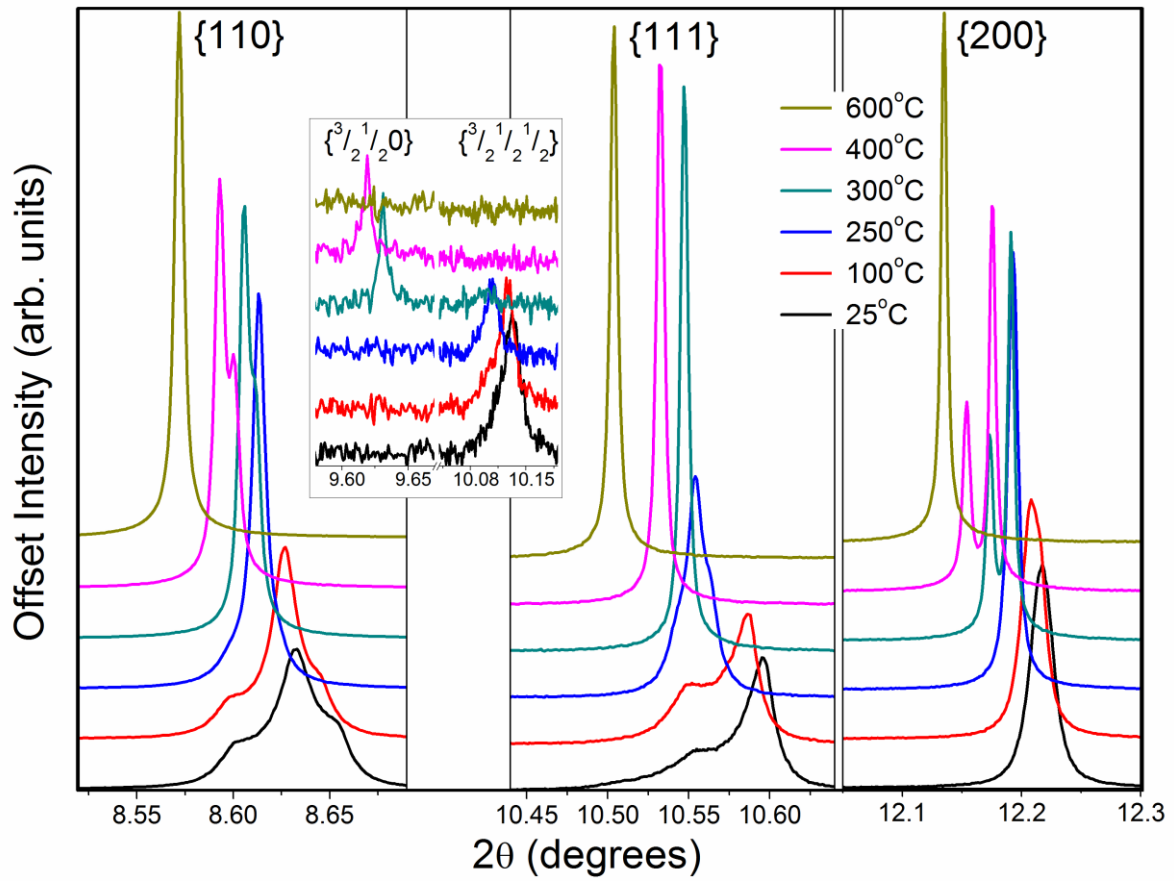


Figure 8-5. Excerpts of high resolution XRD patterns of 1% Fe-modified NBT at selected temperatures.

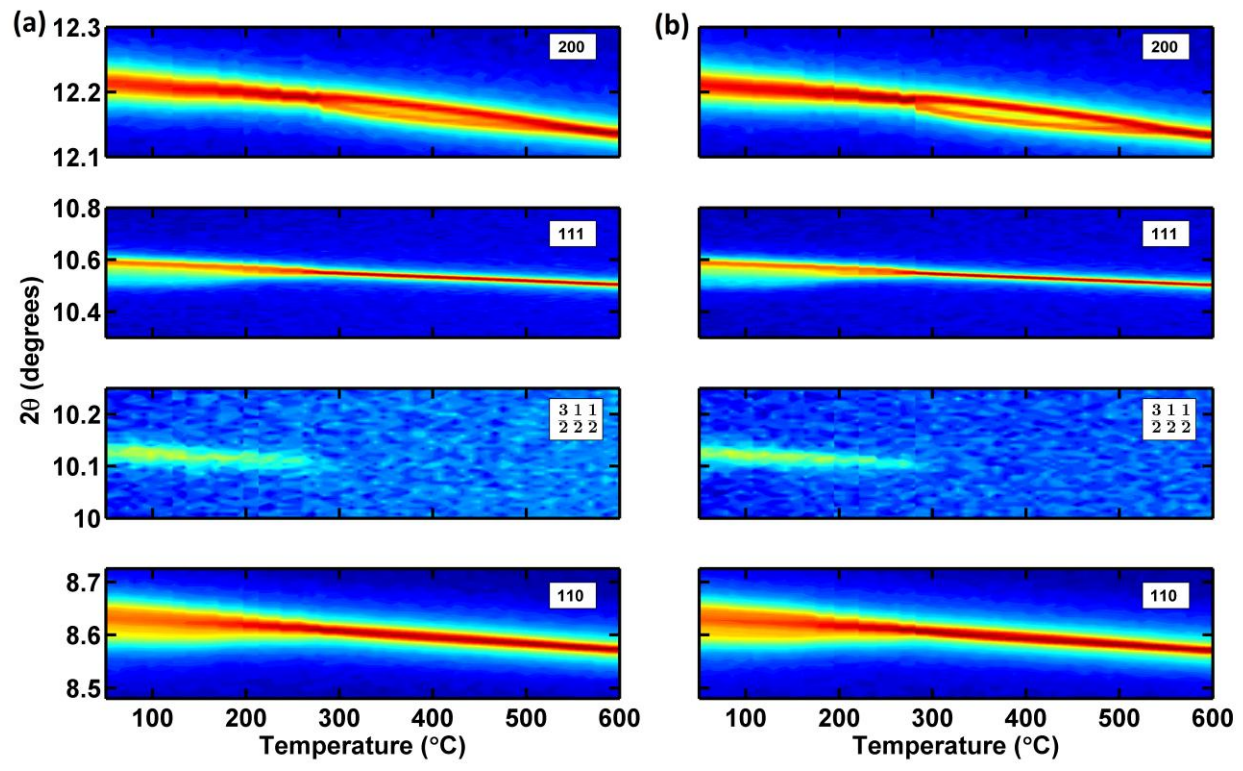


Figure 8-6. Selected areas of XRD patterns of A) unmodified and B) 1% Fe modified NBT as a function of temperature.

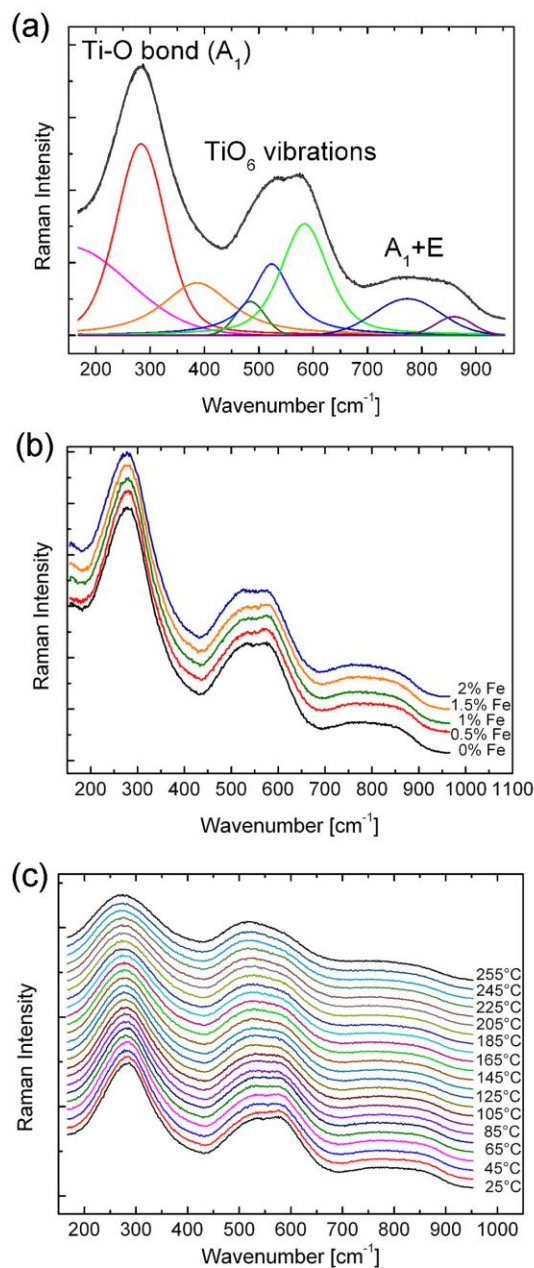


Figure 8-7. Raman spectra of unmodified and Fe-modified NBT samples. A) Raman spectrum of unmodified NBT at room temperature. Spectral deconvolution was performed according to eight Gaussian-Lorentzian modes based on literature.^{121, 122} The assignment of spectral modes to specific vibrations in the crystal lattice is superimposed on the graph. B) Raman spectra of unmodified and modified NBT at room temperature. The spectral signature is not greatly affected by Fe-modification. C) Raman spectra of unmodified NBT as a function of temperature. The displayed temperatures refer to the setting of the heating stage at 20°C steps. The apparent peak coalescence in the mid-frequency region can be ascribed to intrinsic thermal broadening.

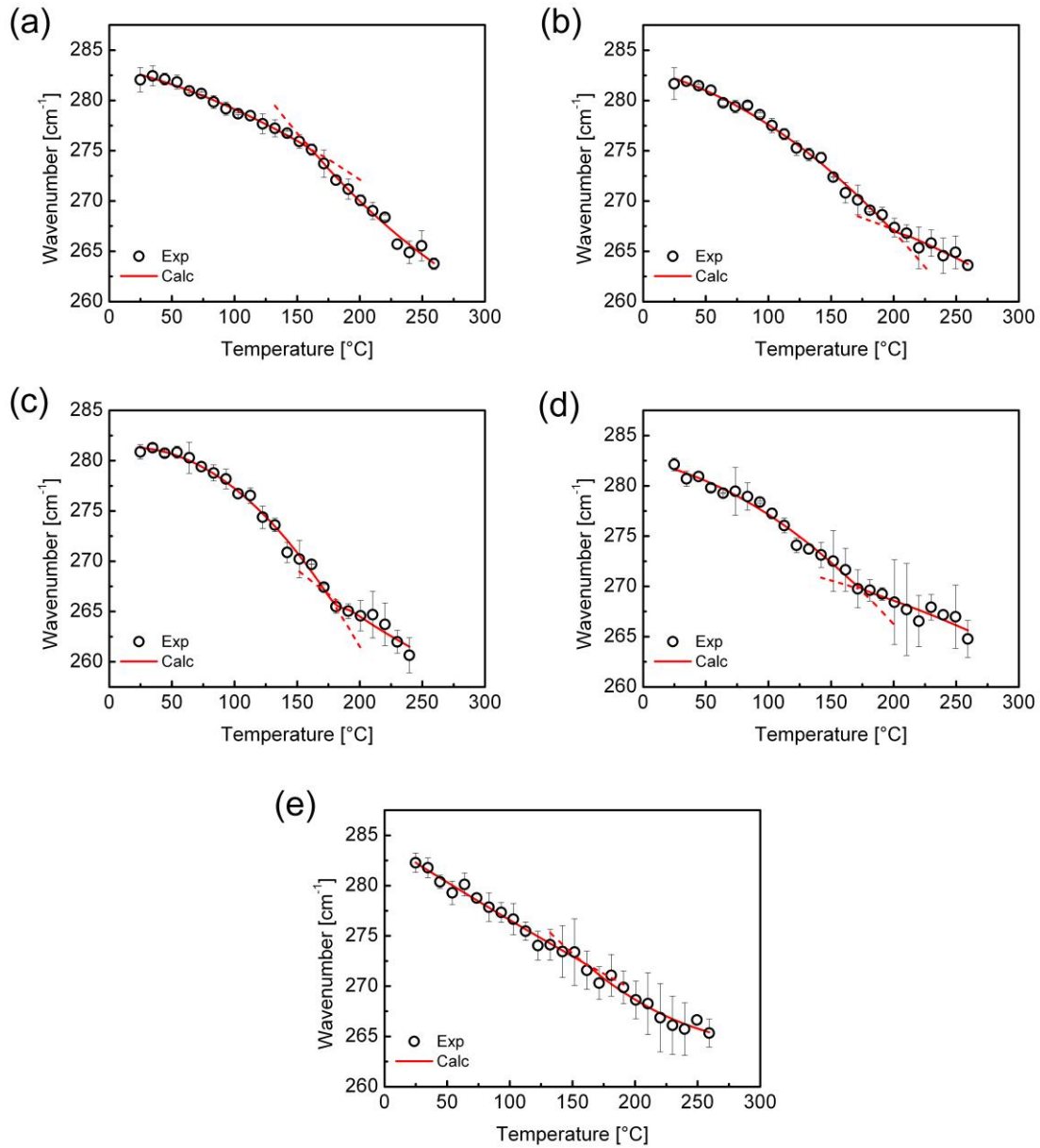


Figure 8-8. Variation of A_1 phonon line center ($\sim 270 \text{ cm}^{-1}$) as a function of temperature for all compositions: A) unmodified NBT, B) NBT with 0.5 at% Fe, C) NBT with 1 at% Fe, D) NBT with 1.5 at% Fe, and E) NBT with 2 at% Fe. Intersection (anomaly) points between two fitting datasets (red line) are highlighted by continued dashed lines, and are observed only in compositions up to 1 at% Fe. The detected anomaly points can be associated with changes in the short-range structure occurring at T_d . For higher Fe content the higher experimental error prevents from detecting any anomaly point, and thus fitting in D and E is presented considering the T_d values obtained from the depolarization study as a first approximation.

CHAPTER 9 CONCLUSIONS AND FUTURE WORK

Conclusions

The crystallographic structure and piezoelectric properties of unmodified and modified sodium bismuth titanate ($\text{Na}_{0.5}\text{Bi}_{0.5}\text{TiO}_3$, NBT) ferroelectric ceramics were examined in this research. NBT-based materials were studied at room temperature and at elevated temperatures, as well as with the addition of chemical modifiers. Based on measurements from a state-of-the-art high resolution synchrotron X-ray diffractometer, a different crystallographic structure and phase transition sequence with temperature are presented for NBT.

Chapter 2 of this work examined the solid-state processing of NBT. It was determined that NBT forms through a particle conversion mechanism of the Bi_2O_3 particle. With the use of advanced diffraction techniques in Chapter 3, it was determined that the room temperature average structure of NBT in its sintered state is best modeled using the monoclinic *Cc* space group rather than the previously accepted rhombohedral *R3c* space group. Chapter 4 expanded on the crystallographic information from the structural refinement by utilizing a combination of the high resolution XRD data with neutron diffraction data. Such an approach was sensitive to both the lattice parameters of the structure (with a degree of accuracy from the high resolution XRD data), and the atomic positions and displacement parameters of the low atomic number elements (which are most dependably measured from the neutron diffraction data).

In Chapter 5, an examination of the local structure of NBT through the Pair Distribution Function (PDF) analysis revealed a departure of the local structure from the average structure. Reverse Monte Carlo simulations of these measurements showed

that Na and Bi are surrounded by different environments. The Na atoms share the A-site equally with the Bi atoms, and it was determined that the O atoms form an isotropic distribution of bond lengths with Na. In contrast, the O atoms which surround the Bi site showed a bimodal split in bond distances. Calculations of the bond valence sums from small box PDF simulations indicated that the motion of the O positions locally may be driven by the low BVS of Bi^{3+} in the average structure.

In order to understand the origin of the piezoelectric depolarization behavior of NBT, crystal structural refinements were carried out at elevated temperatures in Chapter 6. Based on these measurements, it was proposed that thermal depoling in NBT occurs due to the loss of long-range ferroelectric order by a decrease in the volume fraction of the major *Cc* phase and may be associated with the percolation of disordered material. In these analyses it was shown that local regions of disordered material can be adequately modeled using the high temperature parent phase, $Pm\bar{3}m$.

The changes in the structure and properties of NBT were then compared to La- and Fe-modified NBT compositions in Chapters 7 and 8. It was shown in Chapter 7 that the substitution of La up to 1.5 at% decreased the depolarization temperature of NBT and consisted of a higher fraction of the disordered phase modeled by the $Pm\bar{3}m$ space group. On the contrary, with Fe modification up to 1.5 at% in Chapter 8, the depolarization temperature increased while the fraction of the $Pm\bar{3}m$ phase decreased. The correlation between the changes in depolarization temperature and the $Pm\bar{3}m$ phase fraction supports the hypothesis that it is this portion of the material, which is presumed to be present in nano-regions, that strongly influences the depolarization of NBT. The addition of a small amount of modifiers such as La or Fe to PZT often leads to

significant changes in properties. It was determined in this research that while Fe and La behave as acceptor and donor dopants (respectively) in NBT, their effects on the properties of the material are far less significant than their effect on the widely used piezoelectric ceramic PZT.

The nonlinearity of the piezoelectric response with applied field for unmodified and Fe- and La- modified NBT was also examined. Only slight nonlinearity was observed in all NBT-based compositions, implying that the extrinsic domain wall contributions to piezoelectric effect is small in NBT. It is possible that domain wall contributions are minor in this material due to the various pinning sites present in NBT. According to a study from Eitel and Randall on rhombohedral PZT, anti-phase boundaries in tilted ferroelectrics act as pinning sites to domain wall motion and can suppress the extrinsic piezoelectric response.¹⁴² The nano-regions observed in previous studies of NBT,^{25, 27} and modeled in this work using the $Pm\bar{3}m$ phase, along with anti-phase boundaries that may be present due to the tilting of the oxygen octahedra can act as pinning sites to domain wall motion. In studies of PZT compositions at the MPB, the addition of La as a donor dopant led to an increase in the extrinsic contributions to the piezoelectric effect.¹⁴³ Such a change is not observed with La modification in NBT, possibly due to the increase in the $Pm\bar{3}m$ phase fraction with increasing La. These nano-regions may introduce more pinning sites and inhibit domain wall motion.

There has been much debate in the literature over the structural changes in NBT at the depolarization temperature. Recent studies using transmission electron microscopy report the presence of nano domains which have been identified as adopting either tetragonal or orthorhombic symmetry.²⁵⁻²⁷ Although the structural

analysis in the present work cannot distinguish between these structures, it supports the finding that nano-sized regions of a structure which does not match the long range Cc structure are present in the material. The depolarization behavior of NBT has been demonstrated to be associated with the phase fraction of these short range regions.

This research has presented a fundamental study of the crystal structure and related properties of NBT ceramics. This work is of importance in the development of advanced ferroelectric ceramics with piezoelectric properties usable in industry.

Future Work

One key limitation to the use of NBT in industrial applications is the low depolarization temperature. This work illustrated the impact that two different dopants have on this property. However, there is a wide range of other dopants that can be explored to modify the properties. Since doping of NBT with 0.5 at% Fe led to a large increase in T_d without a reduction in d_{33} , it would be especially interesting to combine this small amount of acceptor doping with donor doping to potentially increase the piezoelectric coefficient without a significant decrease in T_d . A previous study which examined co-doping with La and Fe reported an increase in d_{33} (to 155 pC/N) without a large reduction in T_d (to $\sim 190^\circ\text{C}$).¹⁴⁴

In more detailed studies of La-doping in NBT, our results suggested that La^{3+} substitutes preferentially for Bi^{3+} rather than equally substituting on the A-site.¹⁴⁵ Therefore, La doping in NBT may be isovalent rather than donor doping. To better understand the effects of donor doping in NBT, it is interesting to also examine B-site donor dopants. Some preliminary studies were already done in our lab where Ta^{5+} , Nb^{5+} , Sb^{5+} , and W^{6+} were used as donor dopants on the B-site. In those studies, no significant changes in the room temperature piezoelectric and ferroelectric properties of

NBT were observed. The addition of these dopants did however decrease the T_d , as with La doping. It would be interesting to re-examine the effects of these dopants with the addition of small Fe doping.

It is also beneficial to apply the results of the dopant investigation in this research with the current development of NBT-based solid solutions. In the case of the NBT-BT system, an improvement is observed in piezoelectric constant measured at the morphotropic phase boundary, but with an associated reduction in T_d . Since the addition of a small Fe concentration to NBT correlated with an increase in T_d without a decrease in the room temperature d_{33} , it may be a beneficial to explore its use as a modifier in the NBT-BT system as well.

Another unique concern with NBT processing is the effects of potential Bi or Na volatilization during calcination or sintering. In order to understand the effects of these possible changes in stoichiometry, samples of varying Na to Bi ratios can be compared. This study was attempted with four Na to Bi ratios of 49/51, 49.5/50.5, 50.5/49.5, and 51/49. In a preliminary study, the properties of these compositions were compared to stoichiometric NBT samples. It was found that a change in the Na/Bi ratio in either direction led to a decrease in the piezoelectric constant. Also, samples with higher Na/Bi ratio had a sharp decrease in their density which was coupled with high conductivity of those samples. A study of the structure of these compositions using high resolution X-ray diffraction is currently underway.

Since NBT is an end member of many solid solutions which are currently under investigation,³ it is important to reexamine the structure of these materials based on the findings of this work. For example, the phase diagram of the solid solution of NBT-BT

has received much attention recently. The reclassification of NBT as a monoclinic Cc system as well as the addition of the $Pm\bar{3}m$ phase can aid in the refinement of the NBT-BT structures across a compositional range.

This study was restricted to an intense investigation of the crystal structure and selected piezoelectric properties of unmodified NBT, and NBT modified using La and Fe. The future work that this dissertation may inspire is only limited by the range of modifiers and related properties that can be envisioned and examined in order to produce advanced piezoelectric ceramics.

APPENDIX A TECHNIQUES AND MATERIALS

This appendix provides a more detailed description of the materials used in this work, as well as the structural refinement and pair distribution function techniques.

Materials

The particle size of the reactants, calcined powders and sintered ceramics was examined using a scanning electron microscope (SEM). Comparison of the three reactant powders, Bi_2O_3 , Na_2CO_3 , and TiO_2 , in Figure A-1 shows a large variation in the particle sizes of the reactants prior to ball milling. The Na_2CO_3 powders have the largest particle sizes, with particles around 1 mm in size. The size of the Bi_2O_3 powders is significantly smaller, ranging at approximately 2-5 μm , while the TiO_2 particles appear smaller than 1 μm . After ball milling, the mixed reactants were calcined to form NBT. NBT was also formed with different amount of La and Fe doping. Figure A-2 compares the particle sizes of calcined powders of undoped (Figure A-2A), 1 at% La modified (Figure A-2B), and 1 at% Fe modified (Figure A-2C) NBT. It is apparent that in all compositions the particle sizes are smaller than 1 μm and no significant changes are observed as a function of composition. The grain sizes in the calcined powders are then compared to the grain sizes of the sintered ceramics. Figure A-3 shows an SEM image of a cracked surface of a pellet from each of the same three compositions. After sintering, there is a slight decrease in the grain size with La modification (Figure A-3B), and an increase in the grain size with Fe modification (Figure A-3C).

Structural Refinement

Structural refinement of X-ray and neutron diffraction data was done using the Rietveld method. The Rietveld method models the measured diffraction pattern with a

line calculated using a least-squares approach.¹⁴⁶ In this method parameters for the structure and other sample and instrument effects are refined to model the diffraction pattern. Therefore, a reasonably close starting model is necessary for the calculation. The residual minimized during the least-squares refinement, S_y , is calculated by

$$S_y = \sum_i w_i (y_i - y_{ci})^2 \quad (\text{A-1})$$

where y_i is the observed intensity at the i th step, y_{ci} is the calculated intensity at the i th step, and w_i is $1/y_i$.¹⁴⁶ The quality of the fitting can then be described using different criteria of fit parameters, such as R_p (R-pattern) and R_{wp} (R-weighted pattern).¹⁴⁶

$$R_p = \frac{\sum |y_i(\text{obs}) - y_i(\text{calc})|}{\sum y_i(\text{obs})} \quad (\text{A-2})$$

$$R_{wp} = \left(\frac{\sum w_i (y_i(\text{obs}) - y_i(\text{calc}))^2}{\sum w_i (y_i(\text{obs}))^2} \right)^{1/2} \quad (\text{A-3})$$

Where $y_i(\text{obs})$ is the observed intensity and $y_i(\text{calc})$ is the calculated intensity.

Pair Distribution Function Analysis

Although the Rietveld method is a useful approach for obtaining structural information from Bragg peaks, diffuse scattering in the diffraction pattern is often removed with an arbitrary background subtraction.⁸⁸ One method to examine both Bragg and diffuse scattering together is through total scattering techniques. The total scattering data is analyzed through its Fourier transform, which is known as pair distribution function (PDF) analysis. In order to obtain a PDF, the total scattering function, $S(Q)$, must for be measured for the material. An example of the $S(Q)$ function measured for NBT (expressed as the reduced structure function, $F(Q)=Q[S(Q)-1]$) is

shown in Figure A-4. This function can then be related to a PDF using a Fourier transform with the following relation,

$$G(r) = 4\pi\rho_0(g(r)-1) = \frac{2}{\pi} \int_0^\infty Q[S(Q)-1]\sin(Qr)dQ \quad (\text{A-4})$$

where $g(r)$ is the atomic pair distribution function, ρ_0 is the number density of atoms in the system, and $G(r)$ is the reduced pair distribution function.⁸⁸ The neutron $G(r)$ for NBT is shown in Figure A-5. The PDF provides the probability of finding two atoms separated by the distance, r , making it similar to a map of the distances between atoms in the material.⁸⁸

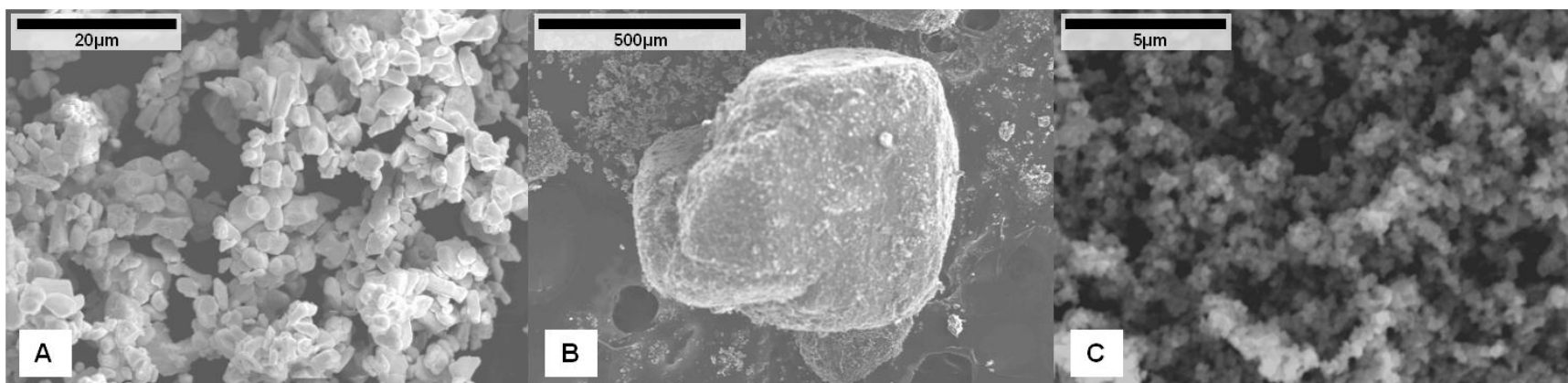


Figure A-1. SEM images of NBT reactant powders. A) Bi_2O_3 , B) Na_2CO_3 , and C) TiO_2 .

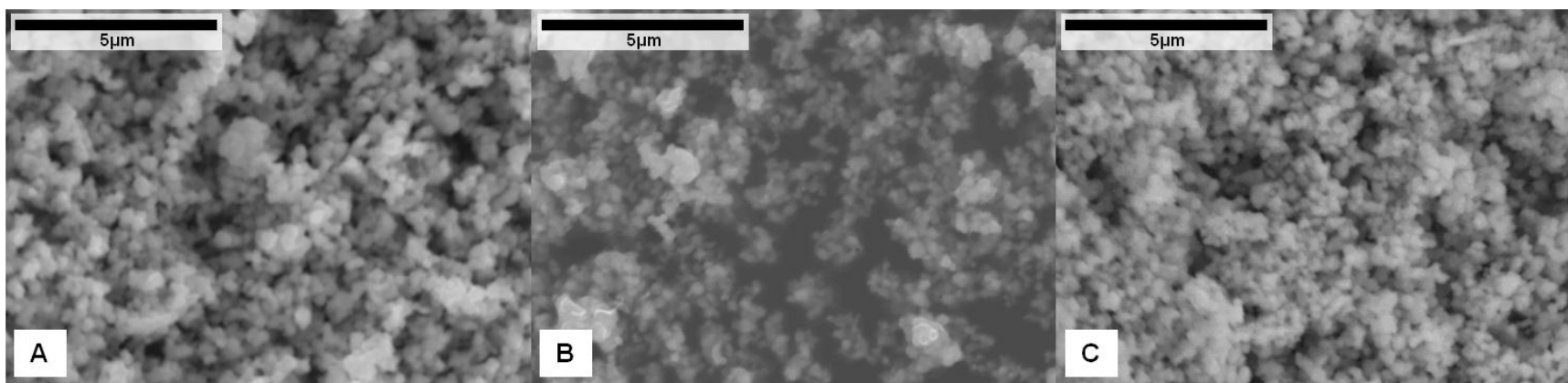


Figure A-2. SEM images of calcined NBT powders. A) Unmodified NBT, B) 1 at% La modified NBT, and C) 1 at% Fe modified NBT.

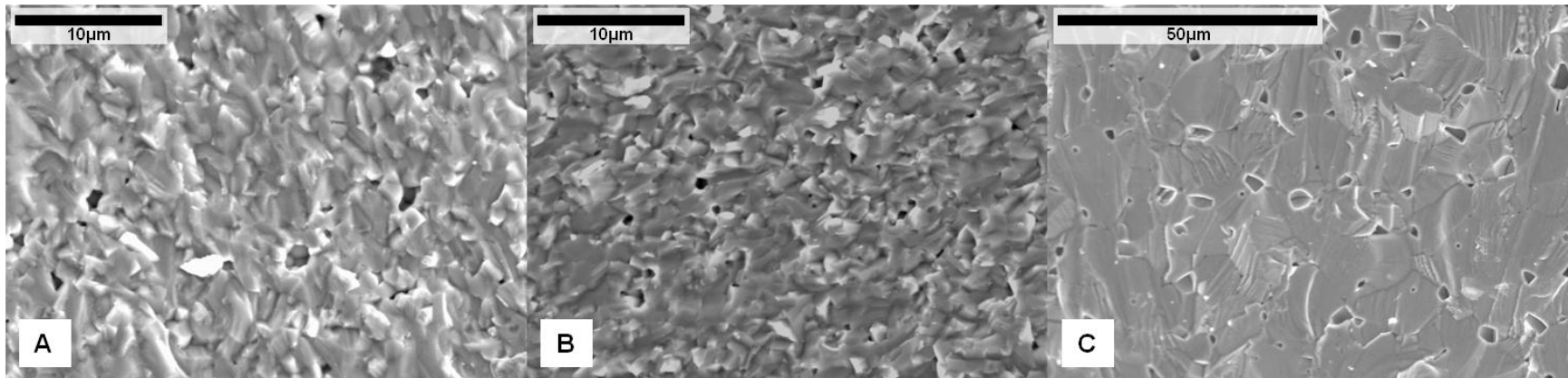


Figure A-3. SEM images of a cracked surface of sintered NBT pellets. A) Unmodified NBT, B) 1 at% La modified NBT, and C) 1 at% Fe modified NBT.

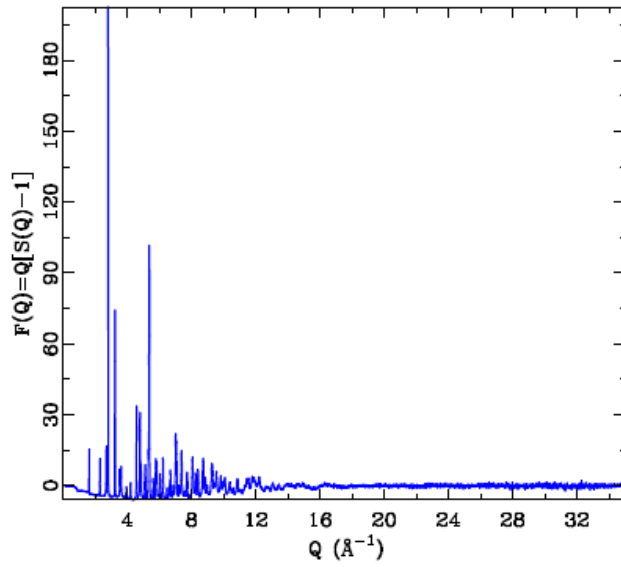


Figure A-4. Total scattering function, plotted as $Q(S(Q)-1)$, for undoped sintered NBT powder.

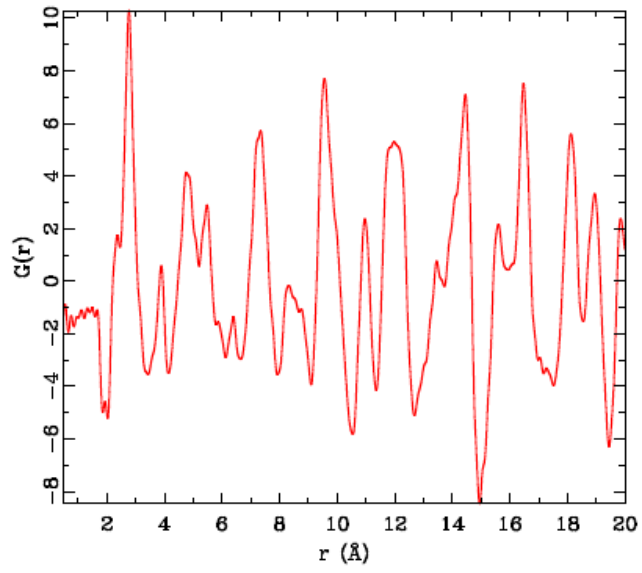


Figure A-5. Neutron $G(r)$ of undoped sintered NBT powder.

APPENDIX B
SUPPLEMENTAL INFORMATION TO CHAPTER 3

Table B-1. Refined lattice parameters and profile fits of calcined and sintered NBT.

Refined structure	Unit cell <i>a</i> (Å)	Unit cell <i>b</i> (Å)	Unit cell <i>c</i> (Å)	Angle (degrees)	Cell volume (Å ³)	Profile fits
Calcined NBT in <i>R3c</i>	5.49095(5)	5.49095(5)	13.4751(2)		351.849(7)	R_p 5.56% R_{wp} 7.20% χ^2 3.55
Calcined NBT in <i>Cc</i>	9.5449(2)	5.48624(7)	5.50096(9)	$\beta=125.3642(6)$	234.934(8)	R_p 5.16% R_{wp} 6.87% χ^2 3.23
Sintered NBT in <i>R3c</i>	5.48703(5)	5.48703(5)	13.4904(2)		351.745(7)	R_p 8.44% R_{wp} 11.72% χ^2 10.23
Sintered NBT in mixture of 2 <i>R3c</i>						R_p 5.97% R_{wp} 8.10%
Phase 1:	5.48558(4)	5.48558(4)	13.5089(2)		352.043(6)	χ^2 4.89
Phase 2:	5.49523(5)	5.49523(5)	13.4675(2)		352.200(7)	
Sintered NBT in <i>Cc</i>	9.5261(2)	5.48308(4)	5.50794(5)	$\beta=125.3442(5)$	234.669(6)	R_p 5.87% R_{wp} 8.09% χ^2 4.21

Table B-2. Refined atomic positions in calcined and sintered NBT.

	Na/Bi (A-site)	Ti (B-site)	O1	O2	O3
Calcined NBT in <i>R3c</i>	0 0 0.2765(1)	0 0 0.01469(2)	0.1344(5) 0.3498(5) 0.0864(4)		
Calcined NBT in <i>Cc</i>	0 0.25 0	0.273(5) 0.250(2) 0.751(1)	0.006(2) 0.212(2) 0.476(5)	0.188(1) 0.486(2) -0.073(3)	0.258(2) -0.021(2) -0.035(4)
Sintered NBT in <i>R3c</i>	0 0 0.2793(2)	0 0 0.0157(2)	0.1157(9) 0.336(1) 0.0932(3)		
Sintered NBT in mixture of 2 <i>R3c</i> (Phase 1)	0 0 0.2771(1)	0 0 0.0160(7)	0.129666 0.349726 0.085639		
Sintered NBT in mixture of 2 <i>R3c</i> (Phase 2)	0 0 0.2557	0 0 0.01603	0.144698 0.408620 0.096223		
Sintered NBT in <i>Cc</i>	0 0.25 0	0.2703(4) 0.2474(9) 0.7427(8)	0.008(3) 0.194(1) 0.493(5)	0.177(1) 0.481(2) -0.137(2)	0.241(1) -0.003(2) -0.044(2)

Table B-3. Refined occupancies in calcined and sintered NBT.

Refined occupancies	Na	Bi	Ti
Calcined NBT in <i>R3c</i>	0.497(9)	0.501(2)	1.041(3)
Calcined NBT in <i>Cc</i>	0.506(9)	0.502(1)	1.036(2)
Sintered NBT in <i>R3c</i>	0.49(1)	0.488(2)	1.014(3)
Sintered NBT in mixture of 2 <i>R3c</i>			
Phase 1:	0.490(4)	0.496(0)	1.005(2)
Phase 2:	0.497(9)	0.453(1)	1.043(5)
Sintered NBT in <i>Cc</i>	0.494(6)	0.498(1)	1.004(2)

APPENDIX C
SUPPLEMENTAL INFORMATION TO CHAPTER 7

Table C-1. Refined atomic positions and isotropic displacement parameters (\AA^2) for samples with increasing La content at room temperatures.

at% La in NBT	Space Group		Na/Bi/La (A-site)	Ti (B-site)	O1	O2	O3	
0	Cc	x	0	0.2652(5)	0.006(2)	0.1857(5)	0.237(1)	
		y	0.25	0.2564(5)	0.1873(6)	0.486(1)	0.002(1)	
		z	0	0.7414(7)	0.484(3)	-0.086(2)	-0.068(2)	
		U_{iso}	0.04203(9)	0.0073(3)	0.015(2)	0.002(1)	0.011(2)	
	$Pm\bar{3}m$	x	0	0.5	0.5	0.5		
		y	0	0.5	0.5	0.5		
		z	0	0.5	0	0		
U_{iso}		0.075(1)	0.029(3)	0.078(5)				
0.5	Cc	x	0	0.2657(5)	0.002(2)	0.1810(6)	0.240(1)	
		y	0.25	0.250(2)	0.1858(7)	0.490(2)	-0.004(2)	
		z	0	0.747(1)	0.482(5)	-0.082(3)	-0.064(2)	
		U_{iso}	0.03850(9)	0.0020(3)	0.001(2)	0.001(2)	0.000(2)	
	$Pm\bar{3}m$	x	0	0.5	0.5	0.5		
		y	0	0.5	0.5	0.5		
		z	0	0.5	0	0		
U_{iso}		0.0688(4)	0.0213(7)	0.019(1)				
1.0	Cc	x	0	0.2679(5)	-0.012(2)	0.1750(7)	0.240(1)	
		y	0.25	0.249(2)	0.1845(8)	0.489(2)	-0.001(2)	
		z	0	0.752(1)	0.455(4)	-0.090(4)	-0.058(3)	
		U_{iso}	0.0416(1)	0.0012(3)	0.000(2)	0.001(2)	0.000(2)	
	$Pm\bar{3}m$	x	0	0.5	0.5	0.5		
		y	0	0.5	0.5	0.5		
		z	0	0.5	0	0		
U_{iso}		7.28(3)	2.65(5)	3.35(8)				
1.5	Cc	x	0	0.2667(6)	-0.003(2)	0.1734(8)	0.240(2)	
		y	0.25	0.249(2)	0.1832(9)	0.476(2)	-0.007(2)	
		z	0	0.751(1)	0.477(6)	-0.093(3)	-0.049(4)	
		U_{iso}	0.0415(1)	0.0014(3)	0.002(2)	0.002(2)	0.003(3)	
	$Pm\bar{3}m$	x	0	0.5	0.5	0.5		
		y	0	0.5	0.5	0.5		
		z	0	0.5	0	0		
U_{iso}		0.0714(2)	0.0252(4)	0.0318(7)				
2.0*	Cc	x	0	0.2677(5)	0.001(2)	0.1765(7)	0.241(1)	
		y	0.25	0.2458(6)	0.1906(7)	0.477(2)	-0.003(2)	
		z	0	0.743(1)	0.484(5)	-0.092(3)	-0.057(3)	
		U_{iso}	0.03729(9)	0.0006(3)	0.002(2)	0.005(2)	0.002(2)	
	$Pm\bar{3}m$	x	0	0.5	0.5	0.5		
		y	0	0.5	0.5	0.5		
		z	0	0.5	0	0		
U_{iso}		0.0785(6)	0.025(1)	0.035(2)				

*A small fraction (~0.5%) of rutile (TiO_2) is present at this composition.

Table C-2. Refined atomic positions and isotropic displacement parameters (\AA^2) for the 1 at% La doped NBT sample at selected temperatures.

Temp. (°C)	Space Group		Na/Bi/La (A-site)	Ti (B-site)	O1	O2	O3	
25	Cc	x	0	0.2679(5)	-0.012(2)	0.1750(7)	0.240(1)	
		y	0.25	0.249(2)	0.1845(8)	0.489(2)	-0.001(2)	
		z	0	0.752(1)	0.455(4)	-0.090(4)	-0.058(3)	
	$Pm\bar{3}m$	U_{iso}	0.0416(1)	0.0012(3)	0.000(2)	0.001(2)	0.000(2)	
		x	0	0.5	0.5			
		y	0	0.5	0.5			
		z	0	0.5	0			
		U_{iso}	0.0728(3)	0.0265(5)	0.0335(8)			
100	Cc	x	0	0.2665(5)	0.007(2)	0.1787(7)	0.237(1)	
		y	0.25	0.2469(9)	0.1897(9)	0.478(2)	-0.002(2)	
		z	0	0.751(1)	0.488(6)	-0.087(3)	-0.061(2)	
	$Pm\bar{3}m$	U_{iso}	0.0409(1)	0.0010(3)	0.002(2)	0.000(2)	0.005(3)	
		x	0	0.5	0.5			
		y	0	0.5	0.5			
		z	0	0.5	0			
		U_{iso}	0.0754(3)	0.023(4)	0.020 (7)			
250	Cc	x	0	0.257(1)	-0.002(1)	0.183(2)	0.224(2)	
		y	0.25	0.264(5)	0.187(2)	0.523(4)	-0.021(4)	
		z	0	0.746(2)	0.467(8)	-0.093(4)	-0.058(6)	
	$Pm\bar{3}m$	U_{iso}	0.0451(2)	0.003(4)	0.009(3)	0.000(3)	0.011(4)	
		x	0	0.5	0.5			
		y	0	0.5	0.5			
		z	0	0.5	0			
		U_{iso}	0.0754(1)	0.0227(2)	0.0325(4)			
300	$P4bm$	x	0	0	0	0.2709(3)		
		y	0	0	0	0.2291(3)		
		z	0.498(6)	0.000 (1)	0.498(6)	0.039(1)		
400	$P4bm$	U_{iso}	0.03843(8)	0.0178(1)	0.066(1)	0.0104(5)		
		x	0	0	0	0.2723(3)		
		y	0	0	0	0.2277(3)		
600	$Pm\bar{3}m$	z	0.509(8)	0.005(1)	0.519(4)	0.038(2)		
		U_{iso}	0.07279(9)	0.0196(1)	0.057(1)	0.0155(5)		
		x	0	0.5	0.5			
		y	0	0.5	0.5			
		z	0	0.5	0			
U_{iso}	0.0794(1)	0.0231(2)	0.0342(3)					

APPENDIX D
SUPPLEMENTAL INFORMATION TO CHAPTER 8

Table D-1 Refined atomic positions and isotropic displacement parameters (\AA^2) for the selected Fe modified NBT samples at room temperature.

at% Fe in NBT Cc setting		Na/Bi (A-site)	Ti/Fe (B-site)	O1	O2	O3
0	x	0	0.2622(5)	-0.002(2)	0.1868(5)	0.2392(9)
	y	0.25	0.250(1)	0.1862(6)	0.489(1)	0.002(1)
	z	0	0.7434(8)	0.472(3)	-0.099(2)	-0.065(2)
	U_{iso}	0.04257(9)	0.0129(2)	0.0069(1)	0.001(2)	0.013(2)
0.5	x	0	0.2735(4)	0.027(1)	0.1717(6)	0.231(1)
	y	0.25	0.2459(6)	0.1975(6)	0.470(1)	0.011(1)
	z	0	0.7433(7)	0.506(3)	-0.053(1)	0.038(2)
	U_{iso}	0.0420(1)	0.0002(2)	0.001(1)	0.003(2)	0.006(2)
1.0	x	0	0.2667(4)	0.030(1)	0.175(1)	0.227(1)
	y	0.25	0.2505(6)	0.1885(8)	0.480(1)	-0.010(2)
	z	0	0.7391(8)	0.516(3)	-0.062(2)	0.016(2)
	U_{iso}	0.04392(9)	0.0039(2)	0.001(1)	0.002(2)	0.002(1)
1.5	x	0	0.2692(4)	0.026(1)	0.1816(7)	0.225(1)
	y	0.25	0.2480(6)	0.1883(7)	0.479(2)	0.000(1)
	z	0	0.7409 (8)	0.489(2)	-0.049(2)	0.033(2)
	U_{iso}	0.0417(1)	0.0050(2)	0.004(2)	0.003(2)	0.000(2)
2.0	x	0	0.2748(3)	0.033(1)	0.197(1)	0.226(1)
	y	0.25	0.2528(9)	0.1651(9)	0.501(2)	-0.022(3)
	z	0	0.7436(7)	0.495(2)	0.017(2)	-0.031(3)
	U_{iso}	0.0456(1)	0.0017(3)	0.004(2)	0.000(2)	0.043(3)

Table D-2 Refined atomic positions and isotropic displacement parameters (\AA^2) for the 1 at% Fe sample at selected temperatures.

Temp. (°C)	Space group		Na/Bi (A-site)	Ti/Fe (B-site)	O1	O2	O3
30	<i>Cc</i>	x	0	0.2667(4)	0.030(1)	0.175(1)	0.227(1)
		y	0.25	0.2505(6)	0.1885(8)	0.480(1)	-0.010(2)
		z	0	0.7391(8)	0.516(3)	-0.062(2)	0.016(2)
		U_{iso}	0.04392(9)	0.0039(2)	0.001(1)	0.002(2)	0.002(1)
100	<i>Cc</i>	x	0	0.2608(5)	0.020(1)	0.1908(5)	0.2396(9)
		y	0.25	0.251(1)	0.1903(6)	0.495(2)	0.005(1)
		z	0	0.7432(8)	0.504(3)	-0.066(2)	-0.049(2)
		U_{iso}	0.05160(9)	0.0118(2)	0.022(2)	0.008(1)	0.011(1)
250	<i>Cc</i>	x	0	0.258(1)	0.008(3)	0.189(1)	0.214(2)
		y	0.25	0.251(2)	0.176(1)	0.536(2)	-0.018(4)
		z	0	0.766(1)	0.521(5)	-0.039(2)	-0.066(3)
		U_{iso}	0.04392(9)	0.0086(3)	0.006(3)	0.015(3)	0.013(3)
	<i>Pm</i> $\bar{3}$ <i>m</i>	x	0	0.5	0.5		
		y	0	0.5	0.5		
		z	0	0.5	0		
		U_{iso}	0.0859(2)	0.0300(3)	0.0542(5)		
300	<i>P4bm</i>	x	0	0	0	0.2714(3)	
		y	0.5	0	0	0.2286(3)	
		z	0.5106(5)	0.0180(8)	0.514(4)	0.0580(8)	
		U_{iso}	0.0718(1)	0.0195(2)	0.072(1)	0.0339(5)	
400	<i>P4bm</i>	x	0	0	0	0.2704(3)	
		y	0.5	0	0	0.2296(3)	
		z	0.5154(6)	0.017(1)	0.487(3)	0.054(1)	
		U_{iso}	0.0754(1)	0.0219(2)	0.077(2)	0.0288(6)	
600	<i>Pm</i> $\bar{3}$ <i>m</i>	x	0	0.5	0.5		
		y	0	0.5	0.5		
		z	0	0.5	0		
		U_{iso}	0.0841(2)	0.0183(2)	0.0494(4)		

APPENDIX E ADDITIONAL PROPERTY MEASUREMENTS

This appendix presents the results of several electrical property measurements that were not included in other chapters. The measurements were conducted on unmodified NBT as well as the La- and Fe- modified compositions studied in Chapters 7 and 8, respectively. The results described in this appendix include permittivity and loss measured as a function of frequency, weak field converse d_{33} measurements, and *in situ* synchrotron diffraction measurements of samples under applied electric fields.

Permittivity and loss as well as weak field d_{33} measurements were recorded on poled ceramics. The poling procedure is given in Chapter 7. Permittivity and loss were measured for each composition from 10 kHz to 0.01 Hz. Relative permittivity and $\tan \delta$ were then calculated and are shown in Figures E-1 and E-2, respectively. In PZT based materials, donor doping often leads to an increase in the relative permittivity and dielectric loss while acceptor doping generally leads to a decrease in the relative permittivity and loss.² The same behavior is observed in NBT. With increasing La modification the relative permittivity and $\tan \delta$ of NBT increase. On the other hand, with increasing Fe modification the relative permittivity and $\tan \delta$ of NBT decrease. The sharp observed increase in the relative permittivity and $\tan \delta$ of Fe modified samples at low frequencies is due to the increased conductivity of these compositions. Also, as observed in PZT, La substitution leads to a slightly larger decrease in relative permittivity with frequency and Fe substitution leads to a slightly smaller decrease in relative permittivity with frequency.

To examine nonlinearity in d_{33} as a function of applied field in NBT-based materials, weak field measurements were also performed on poled samples. The

displacement within the samples was measured using a linear variable differential transducer (LVDT) in combination with a lock-in amplifier. A bipolar electric field of a sinusoidal waveform with a frequency of 1 Hz was applied to each sample. The amplitude of the applied sinusoidal wave ranged from 100 to 1500 V with 100 V increments. Figure E-3 shows the measured displacement as a function of applied voltage for unmodified NBT at three maximum voltages.

The slope of each plot in Figure E-3 was calculated to determine the converse d_{33} at each applied electric field. The calculated converse d_{33} values as a function of applied field for the measured compositions are shown in Figure E-4. A slight nonlinearity in the piezoelectric response is observed with applied field. To compare the different compositions, each series was normalized using the d_{33} value measured at the lowest applied field. The normalized d_{33} results are given in Figure E-5. For comparison, a commercial PZT sample was measured under the same conditions. It is clear from this figure that while a slight nonlinearity is observed in NBT-based compositions, it is significantly lower than what is observed for PZT.

Another aspect of NBT that was examined was the structural change in the material as a function of applied electric field. For these measurements unpoled ceramic samples of unmodified, 1 at% La modified, and 1 at% Fe modified were used. High energy diffraction measurements were conducted on beamline ID15A at the European Synchrotron Radiation Facility (ESRF). X-ray diffraction images were collected in the forward scattering direction using the Pixium 4700 large area detector. Samples were immersed in silicone oil while an electric field was applied perpendicular to the X-ray beam. Selected reflections of the diffraction patterns measured parallel to the electric

field are shown in Figures E-6 – E-7. In the unmodified NBT sample (Figure E-6), the splitting of the 111 peak increases and 110 peak shifts to a lower two theta as the applied electric field reaches 8 kV/mm. In the 1 at% Fe sample (Figure E-7) the splitting becomes even more pronounced, while in the 1 at% La sample (Figure E-8) only a slight change in the peak asymmetry is observed with applied field. This result is consistent with the decrease in peak asymmetry with La modification observed in the high resolution diffraction patterns reported in Chapter 7 and the increase in peak asymmetry with Fe medication reported in Chapter 8.

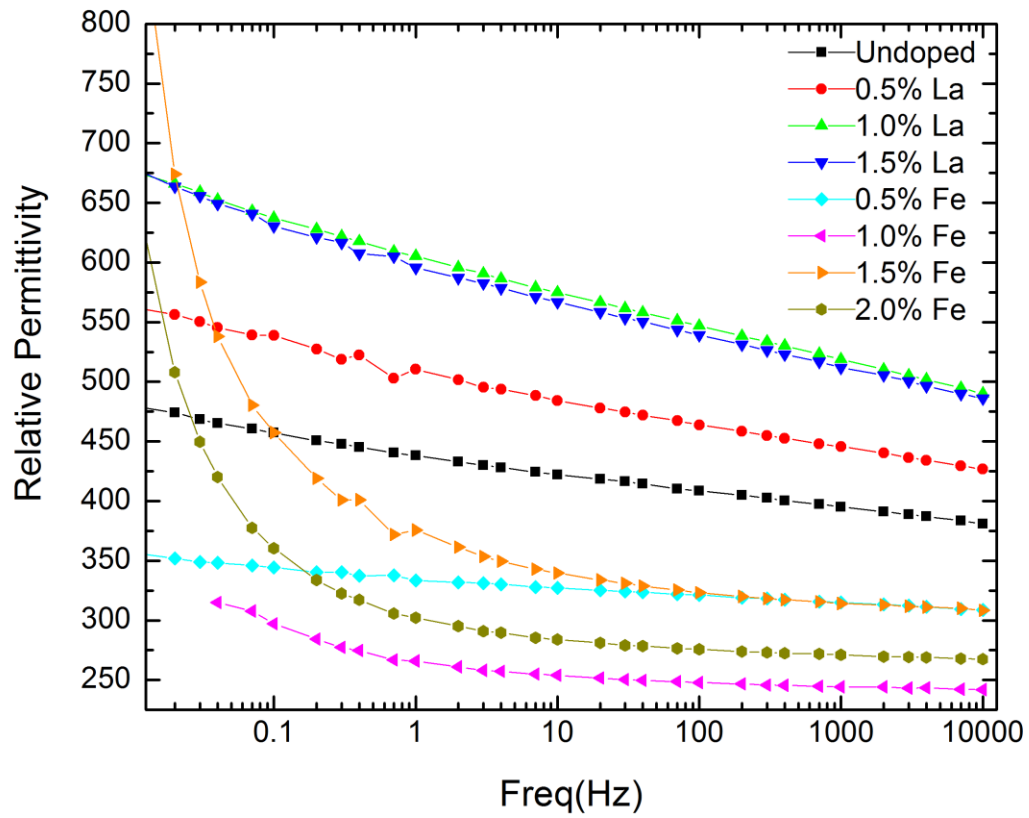


Figure E-1. Relative permittivity measured as a function of frequency for unmodified and Fe- and La- modified NBT samples. All measurements were done on poled samples.

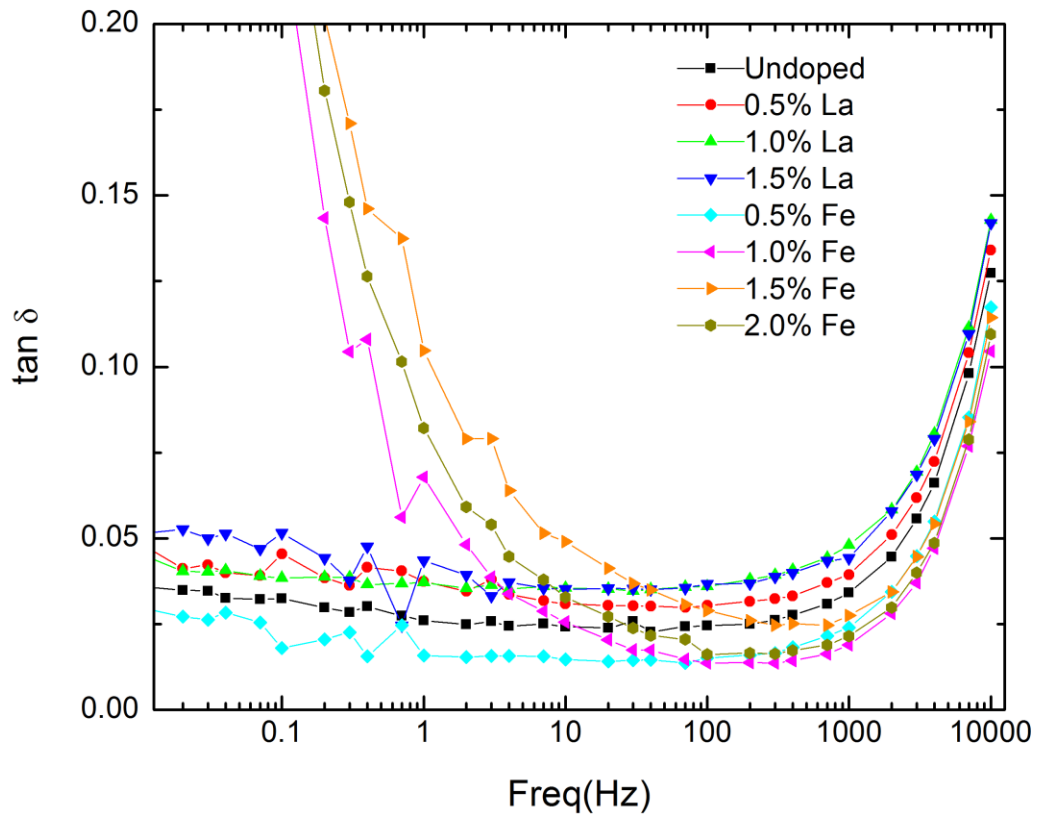


Figure E-2. $\tan \delta$ measured as a function of frequency for unmodified and Fe- and La-modified NBT samples. All measurements were done on poled samples.

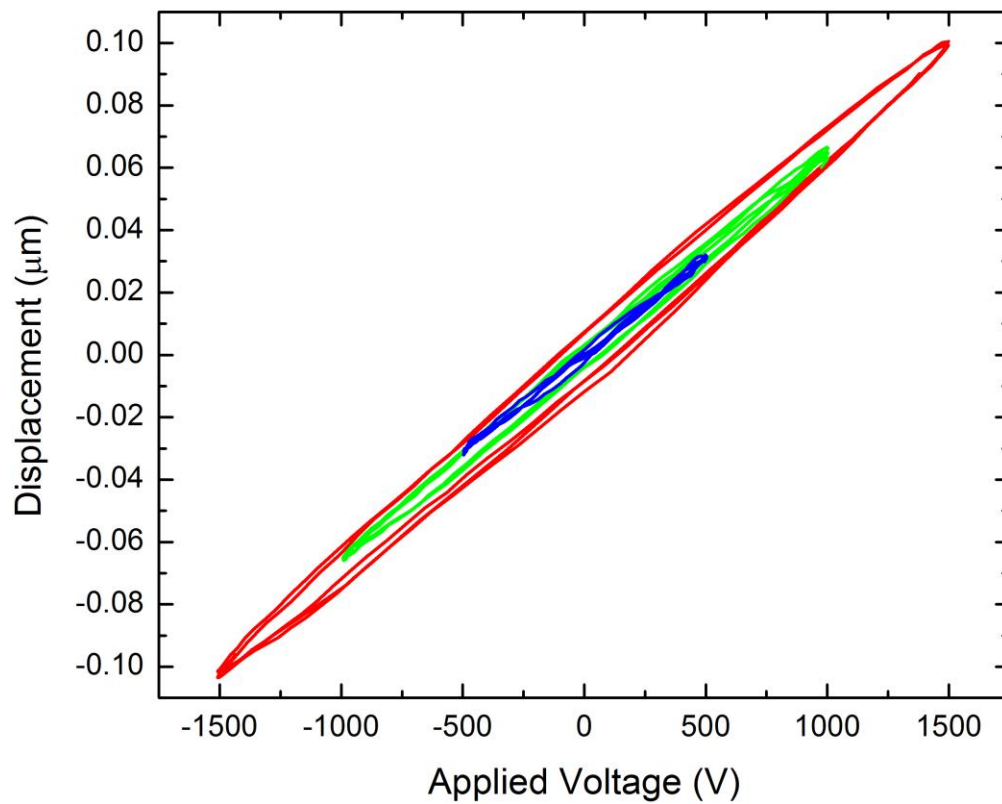


Figure E-3. Displacement measured as a function of small applied voltages for a poled unmodified NBT sample.

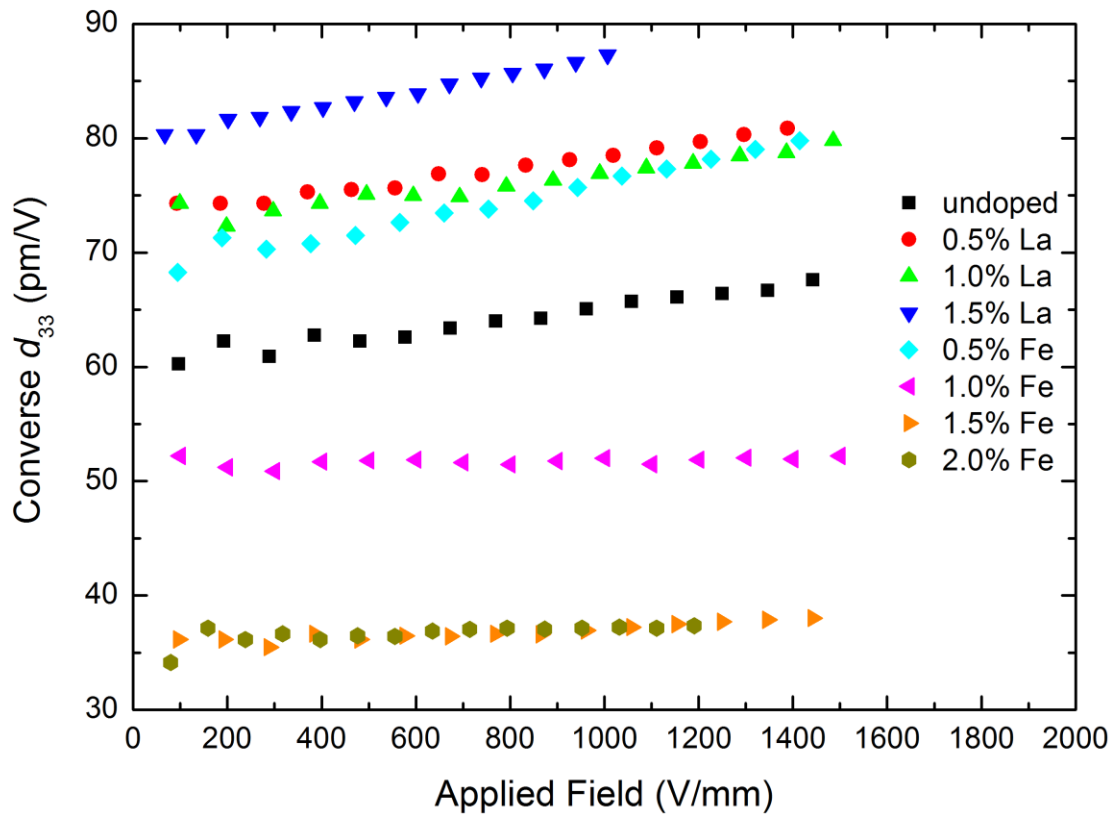


Figure E-4. Converse d_{33} calculated as a function of applied field unmodified and Fe- and La- modified NBT samples. All measurements are from poled samples.

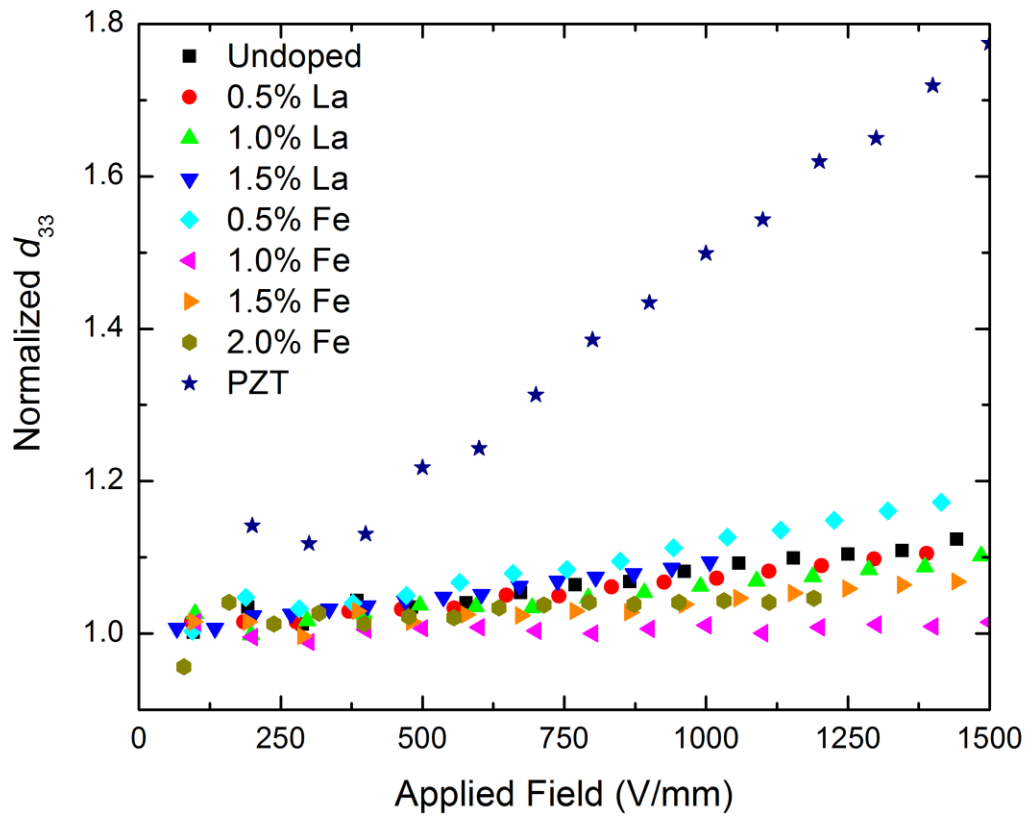


Figure E-5. Normalized converse d_{33} values as a function of applied field unmodified and Fe- and La- modified NBT samples. All measurements are from poled samples. A commercial PZT sample is shown for comparison.

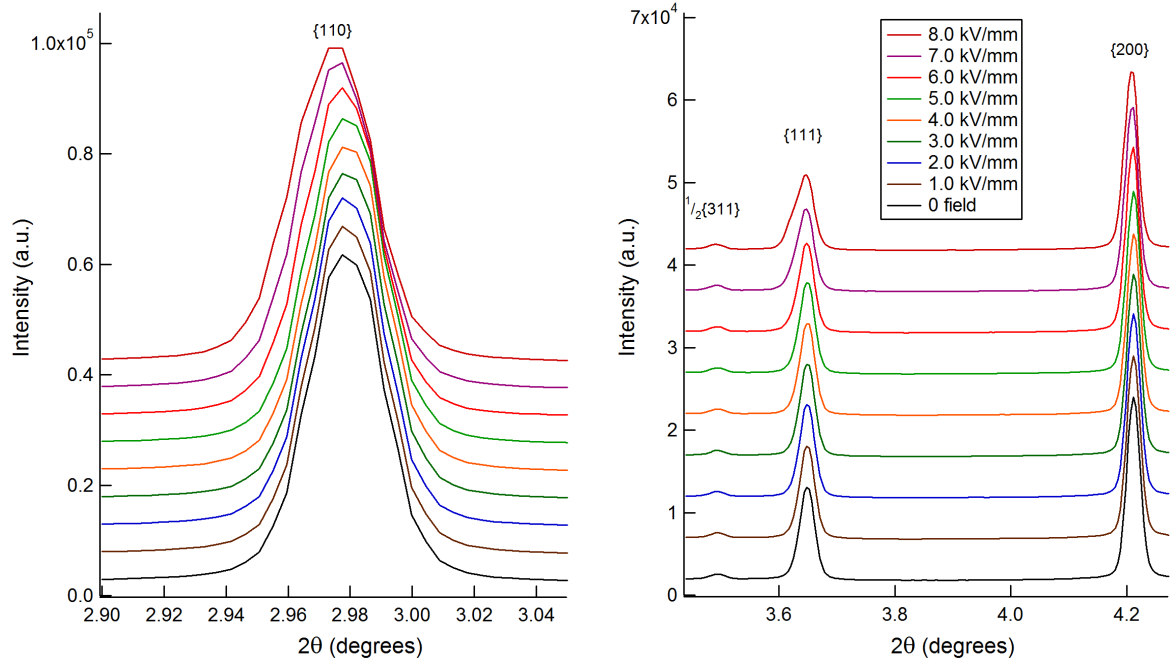


Figure E-6. Diffraction patterns of undoped NBT as a function of applied electric field. The results shown were measured parallel to the applied field.

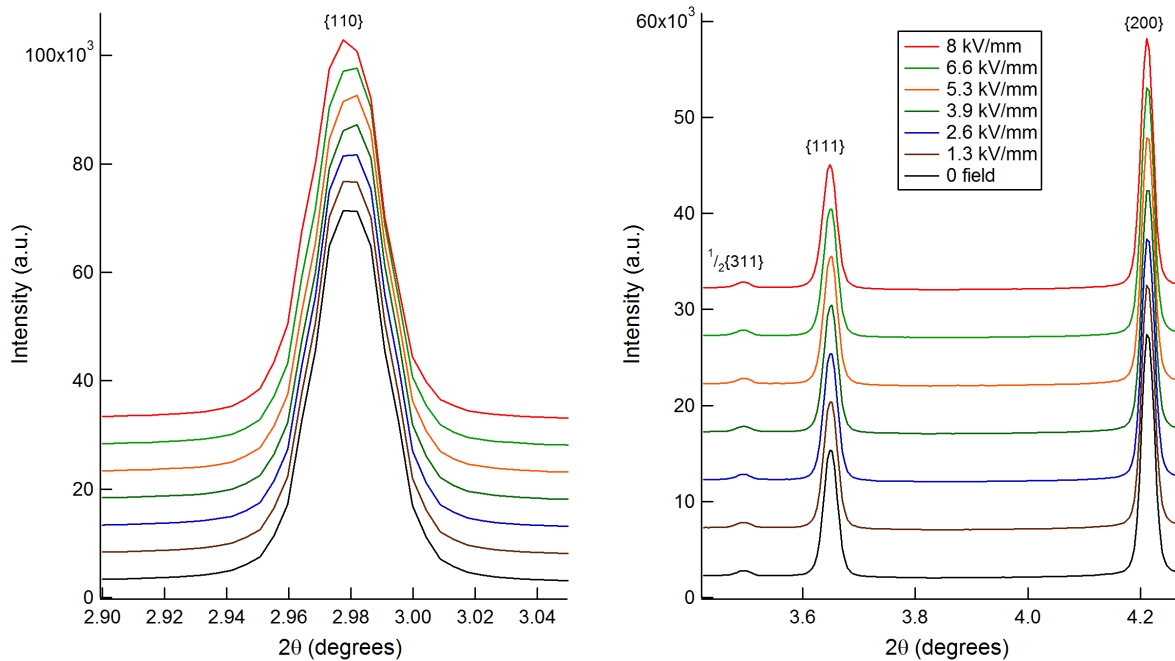


Figure E-7. Diffraction patterns of 1 at% La modified NBT as a function of applied electric field. The results shown were measured parallel to the applied field.

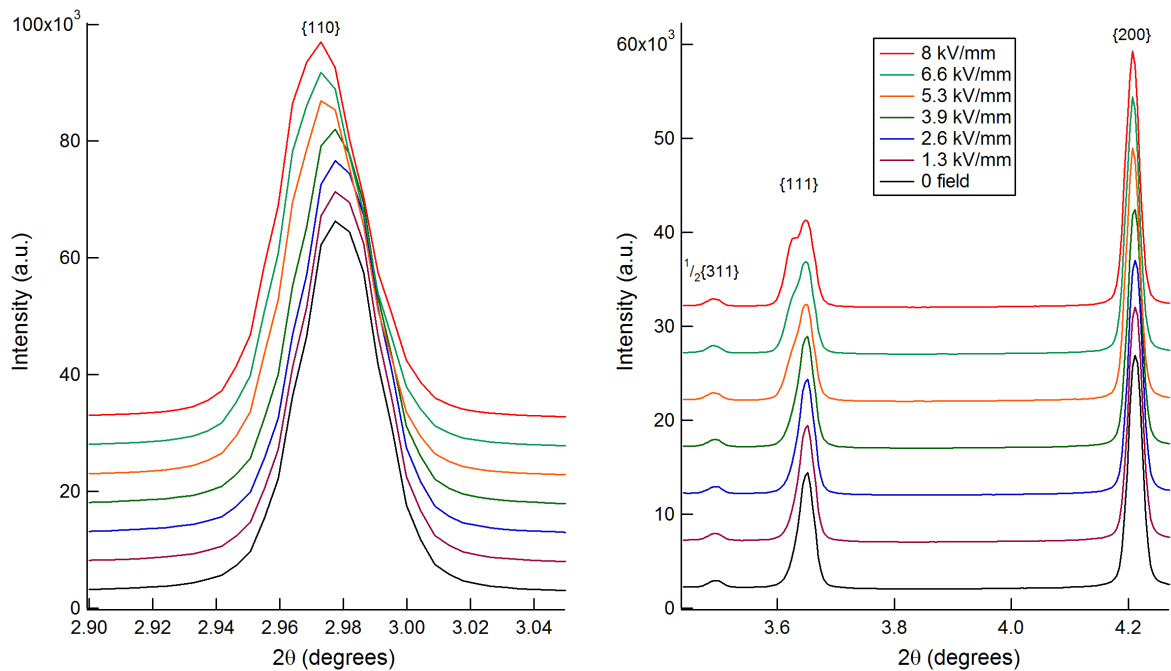


Figure E-8. Diffraction patterns of 1 at% Fe modified NBT as a function of applied electric field. The results shown were measured parallel to the applied field.

APPENDIX F
PUBLICATIONS LIST

1. E. Aksel, H. Foronda, K. Calhoun, J. L. Jones, S. Schaab, and T. Granzow, "Processing and Properties of $\text{Na}_{0.5}\text{Bi}_{0.5}\text{TiO}_3$ Piezoelectric Ceramics Modified With La, Mn, and Fe," *Functional Materials Letters*, Vol. 3, pp. 45-48 (2010).
-This paper lists some initial property and structural measurements done on NBT.
2. E. Aksel and J. L. Jones, "Advances in Lead-Free Piezoelectric Materials for Sensors and Actuators," **Invited Review Article**, *Sensors*, Vol. 10, No. 3, pp. 1935-1954 (2010).
-This invited review paper details the current literature on lead-free piezoelectric ceramics. Parts of this paper are used in Chapter 1.
3. E. Aksel, E. Erdem, P. Jakes, J. L. Jones, and R.-A. Eichel, "Defect Structure and Materials 'Hardening' in Fe_2O_3 -doped ($\text{Bi}_{0.5}\text{Na}_{0.5}\text{TiO}_3$)," *Applied Physics Letters*, Vol. 97, No. 012903 (2010). It is referenced in Chapter 7.
-This paper examines the defect complexes formed in Fe-doped NBT using electron paramagnetic resonance.
4. E. Aksel and J. L. Jones, "Phase Formation of Sodium Bismuth Titanate Perovskite during Solid State Processing," *Journal of the American Ceramic Society*, Vol. 93, No. 10, pp. 3012-3016 (2010).
-Chapter 2.
5. H. Foronda, E. Aksel, and J. L. Jones, "Phase Purity and Site Selection with Lanthanum Doping in Sodium Bismuth Titanate ($\text{Na}_{0.5}\text{Bi}_{0.5}\text{TiO}_3$) piezoelectric ceramic," *University of Florida Journal of Undergraduate Research*, Vol. 11, No. 4, pp. 1-4 (2010).
-This paper describes the project of an undergraduate student in the University Scholars Program. The student was supervised by E. Aksel.
6. E. Aksel, P. Jakes, E. Erdem, D. M. Smyth, A. Ozarowski, J. van Tol, J. L. Jones, and R.-A. Eichel, "Processing of Manganese-doped $\text{Bi}_{0.5}\text{Na}_{0.5}\text{TiO}_3$ Ferroelectrics – Reduction and Oxidation Reactions during Calcination and Sintering," *Journal of the American Ceramic Society*, Vol. 94, No. 5, pp. 1363-1367 (2011).
-This paper examines Mn-doped NBT and discusses changes in the oxidation state of Mn after different processing steps using electron paramagnetic resonance.
7. M. Davies, E. Aksel, and J. L. Jones, "Enhanced high-temperature piezoelectric coefficients and thermal stability of Fe- and Mn-substituted $\text{Na}_{0.5}\text{Bi}_{0.5}\text{TiO}_3$ ceramics," *Journal of the American Ceramic Society*, Vol. 94, No. 5, pp. 1314-1316 (2011).
-This paper examines the depolarization behavior of NBT doped with Fe and Mn.
-The paper is referenced in Chapter 8.

8. E. Aksel, J. S. Forrester, J. L. Jones, P. A. Thomas, K. Page, and M. R. Suchomel, "Monoclinic Crystal Structure of Polycrystalline $\text{Na}_{0.5}\text{Bi}_{0.5}\text{TiO}_3$," Applied Physics Letters, Vol. 98, No. 152901 (2011).
-Chapter 3.
9. E. Aksel, J. S. Forrester, B. Kowalski, P. A. Thomas, and J. L. Jones, "Phase Transition Sequence in Sodium Bismuth Titanate Observed using High-resolution X-ray Diffraction," Applied Physics Letters, Vol. 99, no. 222901 (2011).
-Chapter 6.
10. E. Aksel, J. S. Forrester, B. Kowalski, M. Deluca, D. Damjanovic, and J. L. Jones, "Structure and Properties of Fe-modified $\text{Na}_{0.5}\text{Bi}_{0.5}\text{TiO}_3$ at Ambient and Elevated Temperature," Physical Review B, Vol. 85, no. 024121 (2012).
-Chapter 8.

LIST OF REFERENCES

- 1 N. Setter, in *Piezoelectric materials in devices*, edited by N. Setter (Nava Setter, Lausanne, 2002), p. 518.
- 2 B. Jaffe, W. R. Cook, and H. Jaffe, *Piezoelectric ceramics* (Academic Press, 1971).
- 3 J. Rodel, W. Jo, K. Seifert, E. Anton, T. Granzow, and D. Damjanovic, *Journal of the American Ceramic Society* **92**, 1153 (2009).
- 4 M. D. Maeder, D. Damjanovic, and N. Setter, *Journal of Electroceramics* **13**, 385 (2004).
- 5 D. Damjanovic, N. Klein, J. Li, and V. Porokhonsky, *Functional Materials Letters* **3**, 5 (2010).
- 6 E. Aksel and J. L. Jones, *Sensors* **10**, 1935 (2010).
- 7 C.-W. Ahn, D. Maurya, C.-S. Park, S. Nahm, and S. Priya, *Journal of Applied Physics* **105**, 114108 (2009).
- 8 E. Cross, *Nature* **432**, 24 (2004).
- 9 Y. Saito, H. Takao, T. Tani, T. Nonoyama, K. Takatori, T. Homma, T. Nagaya, and M. Nakamura, *Nature* **432**, 84 (2004).
- 10 D. Xiao, D. Lin, J. Zhu, and P. Yu, *Journal of Electroceramics* **21**, 34 (2008).
- 11 A. Herabut and A. Safari, *Journal of the American Ceramic Society* **80**, 2954 (1997).
- 12 T. Takenaka, K. Maruyama, and K. Sakata, *Japanese Journal of Applied Physics* **30**, 2236 (1991).
- 13 J. E. Daniels, W. Jo, J. Rodel, and J. L. Jones, *Applied Physics Letters* **95**, 032904 (2009).
- 14 A. B. Kounga, S.-T. Zhang, W. Jo, T. Granzow, and J. Rodel, *Applied Physics Letters* **92**, 222902 (2008).
- 15 S.-T. Zhang, A. B. Kounga, E. Aulbach, T. Granzow, W. Jo, H.-J. Kleebe, and J. Rodel, *Journal of Applied Physics* **103**, 034107 (2008).
- 16 G. H. Haertling, *Journal of the American Ceramic Society* **82**, 797 (1999).
- 17 D. Viehland, *Journal of the American Ceramic Society* **89**, 775 (2006).

- 18 G. A. Smolenskii, V. A. Isupov, A. I. Agranovskaya, and N. N. Krainik, *Soviet Physics-Solid State* **2**, 2651 (1961).
- 19 K. Uchida and T. Kikuchi, *Journal of the American Ceramic Society* **61**, 5 (1978).
- 20 J. A. Zvirgzds, P. P. Kapostin, J. V. Zvirgzde, and T. V. Kruzina, *Ferroelectrics* **40**, 75 (1982).
- 21 S. B. Vakhrushev, V. A. Isupov, B. E. Kvyatkovsky, N. M. Okuneva, I. P. Pronin, G. A. Smolensky, and P. P. Syrnikov, *Ferroelectrics* **63**, 153 (1985).
- 22 J. Suchanicz and J. Kwapulinski, *Ferroelectrics* **165**, 249 (1995).
- 23 G. O. Jones and P. A. Thomas, *Acta Crystallographica B* **56**, 426 (2000).
- 24 G. O. Jones and P. A. Thomas, *Acta Crystallographica B* **58**, 168 (2002).
- 25 V. Dorcet and G. Trolliard, *Acta Materialia* **56**, 1753 (2008).
- 26 V. Dorcet, G. Trolliard, and P. Boullay, *Chemistry of Materials* **20**, 5061 (2008).
- 27 R. Beanland and P. A. Thomas, *Scripta Materialia* **65**, 440 (2011).
- 28 S. Gorfman and P. A. Thomas, *Journal of Applied Crystallography* **43**, 1409 (2010).
- 29 M. Groting, S. Hayn, and K. Albe, *Journal of Solid State Chemistry* **184**, 2041 (2011).
- 30 I. Jeong, C. Park, D. Kim, S. Kim, B. Moon, W. Kim, and C. Ahn, *Zeitschrift Fur Kristallographie* **226**, 150 (2011).
- 31 Y. Hiruma, H. Nagata, and T. Takenaka, *Journal of Applied Physics* **105**, 084112 (2009).
- 32 D. Berlincourt, *The Journal of the Acoustical Society of America* **91**, 3034 (1992).
- 33 Y. Watanabe, Y. Hiruma, H. Nagata, and T. Takenaka, *Ferroelectrics* **358**, 139 (2007).
- 34 X. L. Zhang, Z. X. Chen, L. E. Cross, and W. A. Schulze, *Journal of Materials Science* **18**, 968 (1983).
- 35 H. Nagata and T. Takenaka, in *Applications of Ferroelectrics, 2000. ISAF 2000. Proceedings of the 2000 12th IEEE International Symposium on*, 2000), p. 45.
- 36 M. Davies, E. Aksel, and J. L. Jones, *Journal of the American Ceramic Society* **94**, 1314 (2011).

- 37 K. G. Webber, E. Aulbach, T. Key, M. Marsilius, T. Granzow, and J. Rödel, *Acta Materialia* **57**, 4614 (2009).
- 38 PiezoTechnologies, <http://www.piezotechnologies.com/materialssheet.htm>.
- 39 H. Nagata and T. Takenaka, *Journal of the European Ceramic Society* **21**, 1299 (2001).
- 40 H. Shi, W. Pan, M. H. Fang, and D. Xie, *Key Engineering Materials* **280-283**, 209 (2005).
- 41 A. B. Kounga, T. Granzow, E. Aulbach, M. Hinterstein, and J. Rodel, *Journal of Applied Physics* **104**, 024116 (2008).
- 42 E. Aksel and J. L. Jones, *Journal of the American Ceramic Society* **93**, 3012 (2010).
- 43 M. M. Lencka, M. Oledzka, and R. E. Riman, *Chemistry of Materials* **12**, 1323 (2000).
- 44 C.-Y. Kim, T. Sekino, Y. Yamamoto, and K. Niihara, *Journal of Sol-Gel Science and Technology* **33**, 307 (2005).
- 45 F. Remondiere, B. Malic, M. Kosec, and J. Mercurio, *Journal of the European Ceramic Society* **27**, 4363 (2007).
- 46 D. L. West and D. A. Payne, *Journal of the American Ceramic Society* **86**, 769 (2003).
- 47 Q. Xu, S. Chen, W. Chen, D. Huang, J. Zhou, H. Sun, and Y. Li, *Journal of Materials Science* **41**, 6146 (2006).
- 48 A. P. Wilkinson, J. S. Speck, A. K. Cheetham, S. Natarajan, and J. M. Thomas, *Chemistry of Materials* **6**, 750 (1994).
- 49 F. Bondioli, A. B. Corradi, A. M. Ferrari, T. Manfredini, and G. C. Pellacani, *Materials Science Forum* **278 - 281**, 379 (1998).
- 50 M. I. Morozov, L. P. Mezentseva, and V. V. Gusarov, *Russian Journal of General Chemistry* **72**, 1038 (2002).
- 51 V. Zhukov, V. Zhukovskii, V. Zainullina, and N. Medvedeva, *Journal of Structural Chemistry* **40**, 831 (1999).
- 52 T. Suzuki, in *Proceedings of the 14th U.S.–Japan Seminar on Dielectric and Piezoelectric Materials* Welches, OR, 2009), p. 144.
- 53 S. Omar, E. D. Wachsman, and J. C. Nino, *Solid State Ionics* **177**, 3199 (2006).

- 54 A. Weibel, R. Bouchet, and P. Knauth, *Solid State Ionics* **177**, 229 (2006).
- 55 P. Cerisier and F. Roux, *Journal of Solid State Chemistry* **22**, 245 (1977).
- 56 R. Shannon, *Acta Crystallographica Section A* **32**, 751 (1976).
- 57 I. P. Pronin, P. P. Syrnikov, V. A. Isupov, V. M. Egorov, and N. V. Zaitseva, *Ferroelectrics* **25**, 395 (1980).
- 58 G. Trolliard and V. Dorcet, *Chemistry of Materials* **20**, 5074 (2008).
- 59 E. Aksel, J. S. Forrester, J. L. Jones, P. A. Thomas, K. Page, and M. R. Suhomel, *Applied Physics Letters* **98**, 152901 (2011).
- 60 J. Wang, B. H. Toby, P. L. Lee, L. Ribaud, S. M. Antao, C. Kurtz, M. Ramanathan, R. B. Von Dreele, and M. A. Beno, *Review of Scientific Instruments* **79**, 085105 (2008).
- 61 P. L. Lee, et al., *Journal of Synchrotron Radiation* **15**, 427 (2008).
- 62 A. C. Larson and R. B. Von Dreele, *General Structure Analysis System (GSAS)*, Los Alamos National Laboratory Report LAUR, 86 (2000).
- 63 B. H. Toby, *Journal of Applied Crystallography* **34**, 210 (2001).
- 64 Y. S. Sung, J. M. Kim, J. H. Cho, T. K. Song, M. H. Kim, and T. G. Park, *Applied Physics Letters* **98**, 012902 (2011).
- 65 I. Barin, *Thermochemical Data of Pure Substances* (Wiley, Weinheim, Germany, 2008).
- 66 D. Pandey, A. K. Singh, and S. Baik, *Acta Crystallographica A* **64**, 192 (2008).
- 67 H. T. Stokes, E. H. Kisi, D. M. Hatch, and C. J. Howard, *Acta Crystallographica B* **58**, 934 (2002).
- 68 A. Glazer, *Acta Crystallographica B* **28**, 3384 (1972).
- 69 H. Yokota, N. Zhang, A. E. Taylor, P. A. Thomas, and A. M. Glazer, *Physical Review B* **80**, 104109 (2009).
- 70 R. Ranjan, A. K. Singh, Ragini, and D. Pandey, *Physical Review B* **71**, 092101 (2005).
- 71 B. Noheda, D. E. Cox, G. Shirane, R. Guo, B. Jones, and L. E. Cross, *Physical Review B* **63**, 014103 (2000).
- 72 J.-M. Kiat, Y. Uesu, B. Dkhil, M. Matsuda, C. Malibert, and G. Calvarin, *Physical Review B* **65**, 064106 (2002).

- 73 G. Smolenskii, V. Isupov, A. Agranovskaya, and N. Krainik, *Soviet Physics-Solid State* **2**, 2651 (1961).
- 74 D. Damjanovic, *IEEE Transactions on Ultrasonics, Ferroelectrics and Frequency Control* **56**, 1574 (2009).
- 75 T. Leist, K. G. Webber, W. Jo, E. Aulbach, J. Rödel, A. D. Prewitt, J. L. Jones, J. Schmidlin, and C. R. Hubbard, *Acta Materialia* **58**, 5962 (2010).
- 76 A. Pramanick, D. Damjanovic, J. E. Daniels, J. C. Nino, and J. L. Jones, *Journal of the American Ceramic Society* **94**, 293 (2011).
- 77 C. Ma, X. Tan, E. Dul'kin, and M. Roth, *Journal of Applied Physics* **108**, 104105 (2010).
- 78 Y. Hiruma, Y. Watanabe, H. Nagata, and T. Takenaka, *Key Engineering Materials* **350**, 93 (2007).
- 79 W. Jo, J. E. Daniels, J. L. Jones, X. Tan, P. A. Thomas, D. Damjanovic, and J. Roedel, *Journal of Applied Physics* **109**, 014110 (2011).
- 80 F. Zhou, Y. Xu, D. Li, C. He, M. Gao, and T. Wang, *Powder Diffraction* **4** (1989).
- 81 P. A. Doyle and P. S. Turner, *Acta Crystallographica A* **24**, 390 (1968).
- 82 V. F. Sears, *Neutron News* **3**, 26 (1992).
- 83 T. Proffen, T. Egami, S. J. L. Billinge, A. K. Cheetham, D. Louca, and J. B. Parise, *Applied Physics A* **74** [Suppl.], S163 (2002).
- 84 M. N. Burnett and C. K. Johnson, *ORTEP-III: Oak Ridge Thermal Ellipsoid Plot Program for Crystal Structure Illustrations*, Oak Ridge National Laboratory Report ORNL-6895, 1996).
- 85 V. K. Pecharsky and P. Y. Zavalij, *Fundamentals of Powder Diffraction and Structural Characterization of Materials* (Springer, New York, USA, 2005).
- 86 I. Levin, et al., *Chemistry of Materials* **23**, 2166 (2011).
- 87 S. J. L. Billinge and I. Levin, *Science* **316**, 561 (2007).
- 88 T. Egami and S. J. L. Billinge, *Underneath the Bragg peaks : structural analysis of complex materials* (Pergamon, Kiddington, Oxford, UK ; Boston, 2003).
- 89 T. Proffen and K. L. Page, *Zeitschrift für Kristallographie* **219**, 130 (2004).
- 90 V. Krayzman and I. Levin, *Journal of Applied Crystallography* **41**, 386 (2008).

- 91 T. Egami, S. Teslic, W. Dmowski, D. Viehland, and S. Vakhrushev, *Ferroelectrics* **199**, 103 (1997).
- 92 T. Egami, W. Dmowski, M. Akbas, and P. K. Davies, *AIP Conference Proceedings* **436**, 1 (1998).
- 93 V. Petkov, M. Gateshki, M. Niederberger, and Y. Ren, *Chemistry of Materials* **18**, 814 (2006).
- 94 A. L. Goodwin, S. A. T. Redfern, M. T. Dove, D. A. Keen, and M. G. Tucker, *Physical Review B* **76**, 174114 (2007).
- 95 P. F. Peterson, M. Gutmann, T. Proffen, and S. J. L. Billinge, *Journal of Applied Crystallography* **33**, 1192 (2000).
- 96 A. P. Hammersley, S. O. Svensson, M. Hanfland, A. N. Fitch, and D. Hausermann, *High Pressure Research* **14**, 235 (1996).
- 97 X. Qiu, J. W. Thompson, and S. J. L. Billinge, *Journal of Applied Crystallography* **37**, 678 (2004).
- 98 C. L. Farrow, P. Juhas, J. W. Liu, D. Bryndin, E. S. Božin, J. Bloch, T. Proffen, and S. J. L. Billinge, *Journal of Physics: Condensed Matter* **19**, 335219 (2007).
- 99 B. H. Toby and T. Egami, *Acta Crystallographica A* **48**, 336 (1992).
- 100 M. G. Tucker, D. A. Keen, M. T. Dove, A. L. Goodwin, and Q. Hui, *Journal of Physics: Condensed Matter* **19**, 335218 (2007).
- 101 D. Keen, *Journal of Applied Crystallography* **34**, 172 (2001).
- 102 N. E. Brese and M. O'Keeffe, *Acta Crystallographica B* **47**, 192 (1991).
- 103 D. P. Shoemaker, R. Seshadri, A. L. Hector, A. Llobet, T. Proffen, and C. J. Fennie, *Physical Review B* **81**, 144113 (2010).
- 104 E. Aksel, J. S. Forrester, B. Kowalski, J. L. Jones, and P. A. Thomas, *Applied Physics Letters* **99**, 222901 (2011).
- 105 I. P. Pronin, P. P. Syrnikov, V. A. Isupov, and G. A. Smolenskii, *Pis'ma v ZhTF* **5**, 705 (1979).
- 106 V. A. Isupov, *Ferroelectrics* **315**, 123 (2005).
- 107 J. Rodríguez-Carvajal, M. Hennion, F. Moussa, A. H. Moudden, L. Pinsard, and A. Revcolevschi, *Physical Review B* **57**, R3189 (1998).
- 108 A. Garg and D. C. Agrawal, *Materials Science and Engineering: B* **86**, 134 (2001).

- 109 V. Kalem, İ. Çam, and M. Timuçin, *Ceramics International* **37**, 1265 (2011).
- 110 M. Hammer and M. J. Hoffmann, *Journal of Electroceramics* **2**, 75 (1998).
- 111 P. Stephens, *Journal of Applied Crystallography* **32**, 281 (1999).
- 112 R. A. Cowley, *Advances in Physics* **29**, 1 (1980).
- 113 T. Leist, K. G. Webber, W. Jo, T. Granzow, E. Aulbach, J. Suffner, and J. Rodel, *Journal of Applied Physics* **109**, 054109 (2011).
- 114 Y. Hiruma, K. Yoshii, R. Aoyagi, H. Nagata, and T. Takenaka, *Key Engineering Materials* **320**, 23 (2006).
- 115 B. Wylie-van Eerd, D. Damjanovic, N. Klein, N. Setter, and J. Trodahl, *Physical Review B* **82**, 104112 (2010).
- 116 A. Slodczyk, P. Daniel, and A. Kania, *Physical Review B* **77**, 184114 (2008).
- 117 A. Slodczyk and P. Colomban, *Materials* **3**, 5007 (2010).
- 118 A. Feteira, D. C. Sinclair, and J. Kreisel, *Journal of the American Ceramic Society* **93**, 4174 (2010).
- 119 M. Deluca, H. Fukumura, N. Tonari, C. Capianni, N. Hasuike, K. Kisoda, C. Galassi, and H. Harima, *Journal of Raman Spectroscopy* **42**, 488 (2011).
- 120 M.-S. Zhang, J. F. Scott, and J. A. Zvirgzds, *Ferroelectrics Letters Section* **6**, 147 (1986).
- 121 J. Kreisel, A. M. Glazer, G. Jones, P. A. Thomas, L. Abello, and G. Lucazeau, *Journal of Physics: Condensed Matter* **12**, 3267 (2000).
- 122 J. Kreisel, A. Glazer, P. Bouvier, and G. Lucazeau, *Physical Review B* **63**, 174106 (2001).
- 123 J. Petzelt, et al., *Journal of Physics-Condensed Matter* **16**, 2719 (2004).
- 124 D. Rout, K.-S. Moon, S.-J. L. Kang, and I. W. Kim, *Journal of Applied Physics* **108**, 084102 (2010).
- 125 L. Luo, W. Ge, J. Li, D. Viehland, C. Farley, R. Bodnar, Q. Zhang, and H. Luo, *Journal of Applied Physics* **109** (2011).
- 126 E. Aksel, J. S. Forrester, B. Kowalski, M. Deluca, D. Damjanovic, and J. L. Jones, *Physical Review B* **85**, 024121 (2012).
- 127 A. Watcharapasorn, S. Jiansirisomboon, and T. Tunkasiri, *Materials Letters* **61**, 2986 (2007).

- 128 J. E. Daniels, J. L. Jones, and T. R. Finlayson, *Journal of Physics D: Applied Physics* **39**, 5294 (2006).
- 129 J. E. Daniels, W. Jo, J. Rodel, D. Rytz, and W. Donner, *Applied Physics Letters* **98**, 252904 (2011).
- 130 A. Reyes, C. de la Vega, M. E. Fuentes, and L. Fuentes, *Journal of the European Ceramic Society* **27**, 3709 (2007).
- 131 H. Fukumura, H. Harima, K. Kisoda, M. Tamada, Y. Noguchi, and M. Miyayama, *Journal of Magnetism and Magnetic Materials* **310**, e367 (2007).
- 132 M. Balkanski, R. F. Wallis, and E. Haro, *Physical Review B* **28**, 1928 (1983).
- 133 A. P. Litvinchuk, M. N. Iliev, V. N. Popov, and M. M. Gospodinov, *Journal of Physics: Condensed Matter* **16**, 809 (2004).
- 134 H. Fukumura, S. Matsui, H. Harima, K. Kisoda, T. Takahashi, T. Yoshimura, and N. Fujimura, *Journal of Physics: Condensed Matter* **19**, 365239 (2007).
- 135 H. Fukumura, N. Hasuike, H. Harima, K. Kisoda, K. Fukae, T. Takahashi, T. Yoshimura, and N. Fujimura, *Journal of Physics: Conference Series* **92**, 012126 (2007).
- 136 J. Rouquette, J. Haines, V. Bornand, M. Pintard, P. Papet, and J. L. Sauvajol, *Physical Review B* **73**, 224118 (2006).
- 137 P. Gillet, F. Guyot, G. D. Price, B. Tournier, and A. Cleach, *Physics and Chemistry of Minerals* **20**, 159 (1993).
- 138 E. Aksel, E. Erdem, P. Jakes, J. L. Jones, and R.-A. Eichel, *Applied Physics Letters* **97** (2010).
- 139 W. Jo, E. Erdem, R.-A. Eichel, J. Glaum, T. Granzow, D. Damjanovic, and J. Rodel, *Journal of Applied Physics* **108**, 014110 (2010).
- 140 F. Cordero, F. Craciun, F. Trequattrini, E. Mercadelli, and C. Galassi, *Physical Review B* **81** (2010).
- 141 K. Rema, V. Etacheri, and V. Kumar, *Journal of Materials Science: Materials in Electronics* **21**, 1149 (2010).
- 142 R. Eitel and C. A. Randall, *Physical Review B* **75**, 094106 (2007).
- 143 A. Pramanick, D. Damjanovic, J. C. Nino, and J. L. Jones, *Journal of the American Ceramic Society* **92**, 2291 (2009).
- 144 S. Danwittayakul, N. Vaneesorn, S. Jinawath, and A. Thanaboonsombut, *Ceramics International* **34**, 765 (2008).

- 145 H. Foronda, E. Aksel, and J. L. Jones, *University of Florida Journal of Undergraduate Research* **11**, 1 (2010).
- 146 R. A. Young, *The Rietveld Method* (Oxford University Press, Oxford, 2002).

BIOGRAPHICAL SKETCH

Elena Aksel enrolled at the University of Florida in Fall of 2008 after completing her B.S. in Chemical Engineering at the University of Virginia. While studying at the University of Virginia she worked in the research group of Prof. Roseanna Ford for three years investigating bacterial chemotaxis. During her undergraduate studies she held three summer internships in the Research and Development division of Procter and Gamble. Since starting her studies at the University of Florida, she has collaborated with several international researchers, presented her research in several conferences, and published in peer-reviewed international materials science journals.